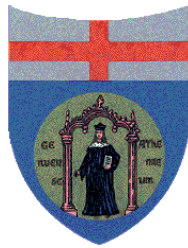


UNIVERSITÀ DEGLI STUDI DI GENOVA



Dipartimento di Ingegneria Meccanica Energetica, Gestionale e dei Trasporti

Sezione di Termo-Energetica e Condizionamento Ambientale

Dottorato in Ingegneria Meccanica Energetica e Gestionale Curriculum Fisica Tecnica

XXXII Ciclo

DYNAMIC THERMAL ANALYSIS OF NEARLY ZERO EMISSION BUILDINGS WITH GEOTHERMAL AND SOLAR PLANTS

Tutor: Prof. Ing. Antonia Priarone

Candidate: Dott. Federico Silenzi

March 2020

Ringraziamenti

Durante il percorso di studi per conseguire questo dottorato di ricerca, ho avuto il piacere di incontrare e di lavorare con molte persone che mi hanno aiutato a crescere sia professionalmente che individualmente.

Vorrei ringraziare profondamente il Prof. Marco Fossa che, con la sua esperienza, la sua passione, la sua pazienza e la sua disponibilità ha saputo indirizzarmi e aiutarmi durante questo percorso. Senza le sue idee e la sua lungimiranza questa tesi non esisterebbe.

Un grande e sincero ringraziamento va alla mia Tutor, la Prof. Antonia Priarone, che mi ha aiutato e ha condiviso con me molte gioie e parecchi dolori “accademici”, lavorando insieme a lei ho imparato molto e le sono riconoscente.

Un abbraccio va a tutti i miei colleghi, che sono stati con me durante questo percorso, condividendo momenti spensierati e momenti impegnativi, incoraggiandomi col loro esempio (in ordine “cronologico” ma non di importanza): un grazie a Ermanno, Camilla, Sara, Chiara, Augusto, Arman, Stefano e Alessia.

Vorrei ringraziare anche Massimo D’Incà (DIBRIS) ed i tecnici di laboratorio Ares e Carlo che mi hanno aiutato a realizzare e a tradurre dall’idea alla pratica molti progetti.

In fine un enorme grazie va a mia moglie Serena, per essermi sempre stata vicino, senza avermi fatto mancare mai il sostegno, la pazienza e l’amore di cui avevo bisogno durante questo percorso. Ringrazio anche la mia famiglia intera (Paola, Fulvio, Valentina, Andrea, Nadia, Alfredo, Biagio, Ielma, Vincenzo, Cesarina, Lucia e Patrizia) per l’affetto, l’esempio e le opportunità che mi hanno dato nel corso della mia vita fino ad ora.

Federico

Abstract

At the present day, the need for the reduction of energy consumption is one of the main issues, from the technical, economic and environmental point of view. Buildings are responsible for more than 40% of energy utilization in European countries in 2017 [1]. Thus, actions that increase building energy efficiency are mandatory. Some interventions on the envelope and the internal operating conditions are addressed to the reduction of the heating and cooling loads of the building (i.e. the energy needs). Others pertain directly to the plants that must be properly selected and sized considering, if possible, also the use of renewable energies.

In this framework, the present study is devoted to the analysis of energy-efficient buildings, with features aimed to reduce the loads and equipped with efficient plant solutions including innovative ground coupled water-to-water heat pumps and high efficiency air to air heat pump with energy recovery.

The first part of the study is devoted to the ground heat exchangers and in particular to the modeling of energy geopiles in which the geothermal heat exchangers are integrated into the foundations of the building. To correctly size a ground heat exchanger (HE) field, in terms of total length, the number of HE and spacing, the ground response is needed and is provided in term of g-function. A new semi-analytical method is proposed, based on the spatial superposition of a basic analytical solution, namely the single point source solution. This method allows generating ground response function (g-functions) for shapes of the heat exchanger different from classical linear one, as for the case of helix. The method has been validated by comparison with literature analytical solutions and with FEM simulations with Comsol Multiphysics.

The second part of the research is devoted to developing a comprehensive model for dynamical energy simulations of a Nearly-Zero-Emission-Building. The model, developed with three different software (Sketch-Up, Openstudio and Energy Plus), represents the Smart Energy Building (SEB) located in the Savona Campus of the University of Genoa. The SEB is a very innovative building for both the envelope (ventilated facades) and the energy systems (i.e. geothermal heat pump and high efficiency air-to-air heat pump with energy recovery). Moreover, it has a complete monitoring system with numerous sensors that provide in real-time numerous thermal and electrical data (temperature, mass flow rates, electrical power, current, etc).

All the detailed features of the building have been analyzed: the geometry, the materials, and the internal operating conditions. The climatic conditions of the site where the building is located are considered through a proper weather file. That information allows evaluating, firstly, the heating and cooling loads, which means the energy needs of the building during winter and summer.

Then, the thermal plants have been introduced into the model, namely the ground coupled water-to-water heat pump and the air handler associated to a high efficiency air-to-air heat pump with energy recovery. For both the heat pumps, the performance (COP

and EER) depends on the load and source-side fluid temperatures. This feature has been carefully implemented in the Energyplus model.

The main results from the simulations are zone temperatures and primary energy consumption from the heating and cooling plants. Finally, the PV modules located on the roof of the SEB have been included in the model. The PV field has been analyzed considering electrical power production, cell temperature and solar irradiance received.

The SEB is included in the complex and complete monitoring system of the Smart Polygeneration Microgrid of the Savona Campus. The validation process of the model with real measurements from the SEB monitoring system would represent an important and original contribution of this study. Unfortunately, a complete analysis is not possible at the moment due to the unavailability of data series about the ventilation system. However, a preliminary comparison between model and measured data has been realized for the electrical production from the PV modules of the roof of the building. In particular, the EnergyPlus model has been updated by inserting a properly modified weather file with the measured values of outdoor air temperature and solar irradiance (global horizontal value). The calculation is done for two sample months (i.e. January and June 2018). The comparison shows a quite good agreement between simulated data trends and measured values, with a discrepancy at peak values. It is not clear if this disagreement is imputable to poor simulation parameter choice or errors in measures acquisition.

Future work will be aimed towards completing the validation of the model using the huge amount of data from the monitoring system. Moreover, the model will be used to study the SEB thermal flexibility to different control strategies.

Table of Contents

| | |
|---|----|
| 1. Introduction | 12 |
| 2. Ground Coupled Heat Pumps: The Use of Geothermal Piles | 15 |
| 2.1. Geothermal Energy and Ground Heat Exchangers | 15 |
| 2.2. The Ground Heat Transfer Phenomena | 17 |
| 2.3. Ground Temperature Response Factor: Classical Analytical Solutions | 19 |
| 2.3.1. Single Point Source Solution | 19 |
| 2.3.2. Infinite Line Source | 20 |
| 2.3.3. Finite Line Source | 21 |
| 2.3.4. Infinite Cylindrical Source | 22 |
| 2.4. Analytical Solution for Geothermal Piles | 23 |
| 2.4.1. Infinite and Finite Solid Cylindrical Source models | 24 |
| 2.4.2. Infinite and Finite Ring Source models | 24 |
| 2.4.3. Infinite and Finite Spiral Source models | 25 |
| 2.5. The innovative Multiple Point Source (MPS) model | 26 |
| 2.5.1. Source Discretization Analysis | 27 |
| 2.5.2. MPS Method Validation with Literature Analytical Solutions | 30 |
| 2.5.3. MPS Method Validation with Two-Dimension FEM Model | 31 |
| 2.5.4. MPS Method Application and Results Discussion | 33 |
| 3. Dynamic Simulation Model for the Smart Energy Building of the Savona Campus | 36 |
| 3.1. The Savona Campus Smart Energy Building (SEB) | 36 |
| 3.2. Heating and Cooling Loads Evaluation | 38 |
| 3.2.1. Weather File Customization Using Elements | 38 |
| 3.2.2. The Ideal Loads Model in EnergyPlus | 38 |
| 3.2.3. Envelope and Geometrical Information | 40 |
| 3.2.3.1. Masonry Analysis | 40 |
| 3.2.3.2. Glazed Surface Analysis | 43 |
| 3.2.3.3. Shading Surface Analysis | 44 |
| 3.2.4. Volumetric Analysis and Thermal Zoning | 45 |
| 3.2.4.1. Geometrical Volume Analysis and Thermal Zones | 45 |
| 3.2.4.2. Thermal Zones Operating Conditions and Internal Gains | 46 |

| | | |
|----------|--|-----|
| 3.2.5. | Ideal Loads System Simulation Results | 53 |
| 3.2.5.1. | Ideal Loads System Simulation Results - Winter Season | 55 |
| 3.2.5.2. | Ideal Loads System Simulation Results - Summer Season | 60 |
| 3.2.6. | Smart Energy Building Plants: Description..... | 64 |
| 3.2.7. | Ground Coupled Heat Pump..... | 64 |
| 3.2.8. | Air-to-air Heat Pump..... | 67 |
| 3.2.9. | Air Distribution System..... | 68 |
| 3.2.10. | Water Distribution System | 70 |
| 3.3. | Smart Energy Building Plants: Modeling in EnergyPlus | 72 |
| 3.3.1. | Heat Pumps Reference Models | 72 |
| 3.3.1.1. | Water-to-water HP Reference Model | 73 |
| 3.3.1.2. | Air-to-air HP Reference Model | 75 |
| 3.3.2. | Heat Pumps Model Implementation | 76 |
| 3.3.2.1. | Water-to-water HP Model Implementation | 76 |
| 3.3.2.2. | Air-to-air HP Model Implementation | 81 |
| 3.3.3. | Heat Pumps Models Validations | 88 |
| 3.3.3.1. | Water-to-water HP Model Validation | 88 |
| 3.3.3.2. | Air-to-air HP Model Validation | 91 |
| 3.3.3.3. | Implementation of the Fancoil model in EnergyPlus | 94 |
| 3.3.4. | Photovoltaic Field of the Smart Energy Building | 94 |
| 3.3.5. | Photovoltaic Effect Theoretical Background..... | 95 |
| 3.3.6. | Smart Energy Building Photovoltaic Field | 97 |
| 3.3.7. | PV Module Models in EnergyPlus..... | 99 |
| 3.3.7.1. | General EnergyPlus PV Modules Model..... | 99 |
| 3.3.7.2. | Equivalent One Diode Model | 100 |
| 3.3.7.3. | Power Production Models | 103 |
| 3.4. | Model Validation | 104 |
| 3.4.1.1. | Inverter Efficiency Calculation..... | 107 |
| 3.4.1.2. | Weather File Enhancing with Measured Climatic Parameters..... | 108 |
| 3.5. | PV field Model Validation..... | 109 |
| 3.5.1.1. | Solar Irradiance Analysis..... | 110 |

| | | |
|----------|--|-----|
| 3.5.1.2. | Module Temperature Validation..... | 111 |
| 3.5.1.3. | Electrical Power Production Validation | 113 |
| 4. | Conclusions and Final Remarks | 116 |
| 4.1. | MPS Method Conclusions..... | 116 |
| 4.2. | Smart Energy Building Ideal Loads Calculation Conclusions | 117 |
| 4.3. | Smart Energy Building Heat Pumps Analysis Conclusions..... | 118 |
| 4.4. | Smart Energy Building Photovoltaic Field Analysis Conclusions..... | 119 |
| | Bibliography | 120 |

Index of Figures

| | |
|---|----|
| Figure 1: Example of APE certificate | 14 |
| Figure 2: Share of installed capacity in the three main geothermal energy application sectors .. | 15 |
| Figure 3: Ground Temperature vs Depth for different months [10] | 16 |
| Figure 4: Generic line discretization example | 27 |
| Figure 5: Comparison between MPS method results (with different $\Delta s/rb$) and reference FLS results (calculated with $rb/H = 10E-3$) | 28 |
| Figure 6: HHE approximated as a series of stacked ring coils | 29 |
| Figure 7: Effect of heat source discretization in case of stacked ring coils heat exchanger | 29 |
| Figure 8: Comparison between MPS method results and reference Analytical Solutions for stacked ring coil heat exchanger | 32 |
| Figure 9: Comparison between the Γ_L -functions between MPS results and FEM results..... | 33 |
| Figure 10: Heat exchangers configuration for the MPS application scenarios | 34 |
| Figure 11: MPS application results confrontation between stacked ring and vertical U-pipe heat exchanger..... | 35 |
| Figure 12: Savona Campus SPM-SEB connection draft | 36 |
| Figure 13: SEB building in Savona Campus | 37 |
| Figure 14: General winter energy balance for a building..... | 40 |
| Figure 15: General summer energy balance for a building | 40 |
| Figure 16: Ventilated façade stratigraphy, layer thickness is reported in [mm] | 41 |
| Figure 17: Modular glazed elements - (a) Hall Façade and Gym (b) Offices and Classrooms (c) Hall entrance and glazed doors | 44 |
| Figure 18: Structural Positioning of Windows | 44 |
| Figure 19: Complete SEB model in Sketchup | 45 |
| Figure 20: Monthly aggregated energy needs and average outdoor air temperature | 55 |
| Figure 21: Selected Thermal Zone..... | 55 |
| Figure 22: Office 3 Temperatures (Outdoor and Indoor) and Relative Humidity - January weekly trends..... | 57 |
| Figure 23: Office 3 Ventilation Heat Loss / Gains and Ideal Loads Heating and Cooling Loads - January weekly trends..... | 57 |
| Figure 24: Office 3 Ventilation and Ideal Loads Air Volumetric Flow Rates - January weekly trends | 58 |
| Figure 25: Gym Temperatures (Outdoor and Indoor) and Relative Humidity - January weekly trends..... | 58 |
| Figure 26: Gym Ventilation Heat Loss / Gains and Ideal Loads Heating and Cooling Loads - January weekly trends..... | 59 |
| Figure 27: Gym Ventilation and Ideal Loads Air Volumetric Flow Rates - January weekly trends | 59 |
| Figure 28: Office 3 Temperatures (Outdoor and Indoor) and Relative Humidity - July weekly trends..... | 61 |
| Figure 29: Office 3 Ventilation Heat Loss / Gains and Ideal Loads Heating and Cooling Loads - July weekly trends..... | 61 |
| Figure 30: Office 3 Ventilation and Ideal Loads Air Volumetric Flow Rates - July weekly trends . | 62 |
| Figure 31: Gym Temperatures (Outdoor and Indoor) and Relative Humidity - July weekly trends | 62 |

| | |
|--|-----|
| Figure 32: Gym Ventilation Heat Loss / Gains and Ideal Loads Heating and Cooling Loads - July weekly trends..... | 63 |
| Figure 33: Gym Ventilation and Ideal Loads Air Volumetric Flow Rates - July weekly trends | 63 |
| Figure 34: (a) TRT machine developed at the University of Genova, (b) Temperature profiles during the first 100 hours of the pulsated TRT experiment | 66 |
| Figure 35: Air Distribution duct lines scheme, detail of the first floor | 69 |
| Figure 36: Detail of Water Distribution Scheme | 69 |
| Figure 37: Heat pump operating conditions draft - (a) water-to-water HP - (b) air-to-air HP (without heat recovery). | 73 |
| Figure 38: (a) $Q_c/Q_{c,ref}$ and (b) P/P_{ref} comparison for cooling mode | 79 |
| Figure 39: (a) $Q_H/Q_{H,ref}$ and (b) COP comparison for heating mode | 80 |
| Figure 40: HP performances in cooling mode, comparison between manufacturer data and Equations (47) and (48) | 87 |
| Figure 41: HP performances in heating mode, comparison between manufacturer data and Equations (49) and (50) | 88 |
| Figure 42: EER in cooling mode: comparison between EnergyPlus simulations and equation fit model approach | 90 |
| Figure 43: COP in heating mode: comparison between EnergyPlus simulations and equation fit model approach | 91 |
| Figure 44: EIR in cooling mode: comparison between EnergyPlus simulations and Equation (48) with Table 25 coefficients | 93 |
| Figure 45: COP in heating mode: comparison between EnergyPlus simulations and Equation (50) with Table 25 coefficients | 93 |
| Figure 46: p-n junction and Space Charge Region [34] | 96 |
| Figure 47: One diode equivalent circuit for an ideal PV cell [35] | 96 |
| Figure 48: SketchUp model of the PV field installed on SEB rooftop | 99 |
| Figure 49: Equivalent One Diode model equivalent circuit for one PV module | 100 |
| Figure 50: EnergyPlus input window for "Equivalent OneDiode" PV model | 102 |
| Figure 51: <i>DESIGO page for the AHU monitoring</i> | 105 |
| Figure 52: Electrical Power aggregated at floor level, for the 1st floor (8 th January - 8 th February 2019) | 106 |
| Figure 53: Inlet and Outlet Temperatures [°C] for the GHE | 106 |
| Figure 54: Efficiency vs partial load curve for typical inverter | 107 |
| Figure 55: Measured Irradiance vs Simulated Irradiance (on horizontal surface) for January ... | 110 |
| Figure 56: Measured Irradiance vs Simulated Irradiance (on horizontal surface) for June | 111 |
| Figure 57: Example of Shading Effect on PV Modules for January | 112 |
| Figure 58: Measured Module Temperature vs Simulated Module Temperature for January | 112 |
| Figure 59: Measured Module Temperature vs Simulated Module Temperature for June | 113 |
| Figure 60: Electrical power comparison between measured data (modified with inverter efficiency) and electrical power calculated with module temperature and total irradiation simulated, for January..... | 114 |
| Figure 61: Electrical power comparison between measured data (modified with inverter efficiency) and electrical power calculated with the MPP method-Equation (70), for June | 114 |

**Figure 62: Module efficiency calculated applying Equation (72) to measured and simulated
Module Temperature (January)..... 115**

**Figure 63: Module efficiency calculated applying Equation (72) to measured and simulated
Module Temperature (June)..... 115**

1. Introduction

This brief introductory chapter will address the overall problem context and will give information on how the present work positions itself in that framework.

Energy saving is one of the most important keywords that lead the research in many countries of the world, covering many different fields. In the present work, the problem is analyzed from the building energy consumption point of view, considering also the importance of renewable sources of energies, like geothermal and solar energies.

Buildings are covering a crucial role when dealing with energy consumption and different ways can be followed to move towards their more efficient energy use. For instance, the use of high thermal performance materials allows reducing the heat flux through the building's external surfaces. Acting on the energy plants, it is possible to choose high-efficiency devices (such as heat pumps) coupled with renewable energies sources (geothermal or solar energy). Moreover, building management is important and in this scenario the user is the most important factor. By developing virtuous behaviors (like turning off lights when not needed or lowering the thermostat when leaving the building) it is possible to reduce energy waste. In this sense is useful to consider home automation devices. The building can be refurbished for this application, substituting traditional systems (like lighting, window blinds, thermostat and conditioning system) with dedicated devices, with a high costly operation. However, as Ringel et al. [2] show, the energy savings with the application of smart home devices can be relevant even when low cost or partial solutions are applied.

The European Commission started to consider the energy performance of building in 2010, with the emission of the Energy Performance of Building (EPBD) EU directive [3]. The directive established some guidelines aimed towards the reduction of emissions related to the residential sector (in the framework of the Horizon 2020 program). In particular, the European Commission promoted the application of new technologies to existent building and the use of alternative energy and renewable energy sources together with innovative systems (like heat pumps).

EPBD established a methodology that can be used to evaluate the energy performance of buildings, during a given period (a year). This is important because all the members of the EU, in this way, have to standardize the calculation method of energy performance of buildings, even if the application of the methodology can be differentiated at national and regional levels.

Aside from this methodology, the EPBD indicates also other tools that can be applied when dealing with energy performance of buildings. One of the most important indicators proposed by the EPBD is the Energy Performance Certificate (EPC), which clearly states the energy performance class of the building. This certificate has a 10-years duration and it is mandatory when the building is sold or rent.

In Italy, with the application of by the inter-ministerial decree of the 26 June 2015 [4], it is necessary to produce the Attestato di Prestazione Energetica (APE) which identifies the global energy performance index of the building. This certificate assigns a specified class to the considered building, starting from “G” (which is the most commonly assigned class to standard buildings with poor or no measures for energy consumption reduction) going up to “4A” which represents the most efficient class. Figure 1 shows an example of an APE certificate.

This certificate also allows to label the building as a Nearly Zero Energy Building (NZEB). A Zero Energy Building (ZEB) is a particular class of buildings defined for the first time by Torcellini et al. in 2006 [5]. When dealing with ZEB the main issue is to correctly identify a uniform criterion able to define the zero-energy threshold. For this reason, the Authors provide four different definitions that can be used:

- Net Zero Site Energy: the energy produced on-site by the building must be equal to or greater than the amount it requires. This definition is the simplest and does not account for the type of energy used, but only if the energy is produced in situ. In this case, the delivered energy to the building plants is zero for all the external energy carriers;
- Net Zero Source Energy: in this definition is necessary to account for the site-to-source conversion multipliers, that are different depending on the energy extraction, generation or distribution. The source energy is then calculated as the primary energy used to both generate and deliver the energy to the building, multiplying by the site-to-source conversion coefficients. This definition favors the use of natural gas as an energy source;
- Net Zero Energy Costs: this definition is the more economy-oriented one because it accounts for money that can be generated selling to the grid the energy produced by the building. A building can be considered a net-zero energy cost if, over a year, the income generated by selling the energy is equal or greater than the amount spent on buying energy. This definition is not completely exhaustive because the energy prices for selling or buying electricity are variable in time (a building may fulfill the definition criterion one year but not the next). Also, since the selling price is different from buying price, it can be necessary to produce more energy compared to the net-zero site or source definitions;
- Zero Energy Emissions: the building must produce an amount of emission-free energy from renewable sources equal to or greater than the amount of energy generated by other emission-producing sources. This definition is site depending. For instance, considering a building located in a country with strong energy production from renewable sources (like hydroelectric) it is necessary to consider this in its energy balance, actually lowering the avoided emission goal concerning the same building located in a country where the electricity is mainly produced by fossil fuels.

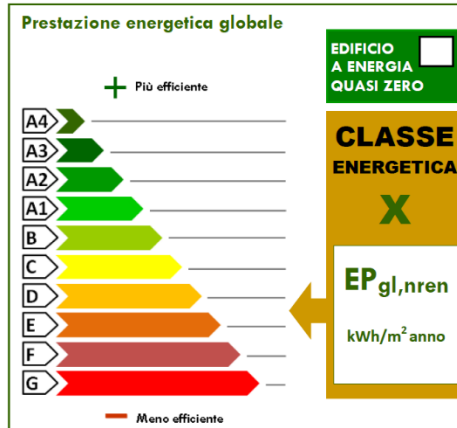


Figure 1: Example of APE certificate

A more general description can be given taking into consideration all the aspects highlighted by the four definitions listed above. A ZEB can be considered as an energy-efficient building able to generate electricity, or other energy carriers, from renewable sources to balance its energy demand. Aiming to reduce and minimize the environmental impact, different renewable energy technologies are available within the building's footprint, such as rooftop PV and solar water heating. The production can be coupled with a reduced energy need through the application of low-energy technical solutions: high insulated envelope, natural daylighting and ventilation, high-efficiency HVAC equipment, etc.

A Nearly Zero Emission Building differs from this general description only in the threshold used to define the energy target. For an NZEB this threshold is not set to zero, but it is low enough. For instance, the EPBD [3] refers to NZEB as a building that has a very high energy performance and covers a significant percentage of its energy request with energy from renewable sources even produced on-site or nearby.

Another important point that can be useful to discuss more deeply is the concept of "Net Zero", because it implies that an energy balance must be established, no matter what is the definition that is used. The energy balance is calculated considering the building and the grid. This kind of mutual relationship is influenced by many factors, including the stability and the power quality sold to the grid. It is useful, then, to think about the smart grids (as the one present at the Savona Campus, in which the Smart Energy Building is integrated) that allow for more easily controlled production, storage, and delivery of the produced energy. This, in turn, allows to better control the emissions and to reduce the operating costs [6].

2. Ground Coupled Heat Pumps: The Use of Geothermal Piles

This first part of the thesis describes some general fundamental information about geothermal energy and its exploitation in low enthalpy applications. Then, the ground temperature response functions (g-functions) are introduced with their importance in the designing process of ground heat exchangers, in particular in case of geopiles systems. Finally, a new semi-analytical model for calculating g-functions is presented and discussed widely for the selected application of geopiles systems.

2.1. Geothermal Energy and Ground Heat Exchangers

Geothermal energy is the heat produced by the Earth itself, and it is generated mainly by the radioactive decay that continuously takes place into the planet core. The heat produced is transmitted outwards, towards the surface. The temperature difference between the core and the surface is known as the geothermal gradient, and on average is equal to 25°C for every kilometer of depth. This heat can be exploited in different ways, depending on the depth (and thus, the temperature) at which it is extracted: low enthalpy systems are adopted to harvest heat from 0 to 1 Km depth, from 1 Km up to 3.5 Km it is possible to exploit hot water aquifers, while at higher depths one speaks of hot dry rock systems [7].

Given the high specificity of the geothermal source, which can be different from place to place for depth and temperature, several different technologies have been developed. In general, it is possible to divide geothermal exploitation into three main categories:

- Shallow application, which uses mainly Ground Coupled Heat Pumps (GCHP);
- Direct uses, employing district heating mostly;
- Electrical power production with dedicated power plants;

As the European Geothermal Congress 2019 reported [8], geothermal energy is mainly exploited with shallow applications, especially in countries like Sweden, Germany, France, and Finland.

In the present work, only the GCHP applications are investigated.

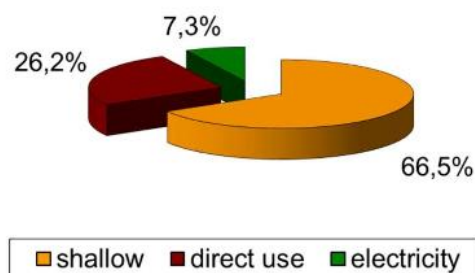


Figure 2: Share of installed capacity in the three main geothermal energy application sectors

Geothermal energy can be considered as a great opportunity for preserving environment and energy saving purposes, being free and vastly available almost everywhere on the planet. As shown in Figure 3, below approximately 10 meters from the surface, the ground can be considered at a constant temperature throughout the year, thus offering great stability as a source for heat pump systems. The average temperature of the ground is variable from place to place but, in general, the ground of a defined site is warmer during winter and cooler during summer than its external air.

To exploit ground heat, it is necessary to realize a horizontal or vertical heat exchanger field. If the heat exchanger is realized horizontally, it is necessary to remove part of the ground (with excavators) to realize a shallow but large excavation. Usually, the depth is 2-3 meters while the length can be some ten meters. This configuration is easier to realize but suffers from seasonal variability of ground temperature. Moreover, horizontal heat exchangers are very demanding for available free terrain surface, and this can be a relevant issue when considering highly populated areas, where buildings are often very close one to another. Moreover, the amount of required surface can be unfeasibly large in case of, particularly big system application.

If the borehole field is realized vertically, a series of narrow and depth holes have to be realized into the ground. The number and depth of the boreholes depend on the size of the ground heat exchanger that has to be realized. Generally, the radius of each borehole is about 0.5 meters, while the depth can be up to several hundred meters (100-300 m). This configuration, called Borehole Heat Exchanger (BHE), is much more difficult to realize and highly specialized technicians and dedicated operating machines must be employed. As a consequence, vertical heat exchangers suffer for the high cost of the borehole drill, which according to Liu et al account for more than 30% of the total system cost [9]. On the other hand, they are not suffering from seasonal temperature variability.

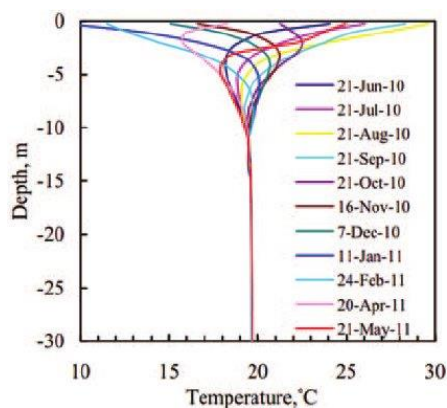


Figure 3: Ground Temperature vs Depth for different months [10]

Once the ground has been properly drilled, it is possible to insert the pipes that will constitute the network in which the operating fluid will circulate, realizing in this way a ground heat exchanger (GHE).

The plastic pipes (High-Density PolyEthylene - HDPE) are commonly arranged in a single or double U configuration and buried into the ground. The operating fluid (usually water or a mixture of water and an antifreeze liquid, like glycol or ethyl alcohol) is circulated through the heat exchanger to modify its temperature accordingly to the heat pump seasonal operation. During the heating season, the carrier fluid is usually colder than the ground, so the fluid is heated by the ground. Vice versa, during the cooling season, the operating fluid enters the heat exchanger at a temperature higher than the ground one. In this way, it is possible to extract heat from the ground during winter and to inject heat into the ground during summer.

The ground heat exchanger performance depends also on the ground thermophysical parameters. These parameters are often assumed equal to some standards values that are typical for the region in which the system is realized, but sometimes this approach can lead to poor design of the heat exchanger. For this reason, a Thermal Response Test (TRT) can be performed to experimentally determine the values for the ground thermal conductivity and BHE thermal resistance. Generally, a TRT is performed circulating a fluid (usually water) into a GHE, using a pump, while heating or cooling the fluid with constant power. The GHE inlet and outlet fluid temperature are recorded for all the test duration, which can be up to several days. Recently, Fossa et al. [11] developed a device able to carry out a TRT test with a time-variable heat pulse to the ground, to achieve information on the heat transfer also for transient regimes. In this way, it is possible to size the system without the risk of either underestimate or overestimate the total length of the ground heat exchanger.

2.2. The Ground Heat Transfer Phenomena

The heat transfer process in the ground is a complex mechanism, usually studied under certain simplified assumptions, listed as follow:

- Only heat conduction is considered in the ground;
- The ground is considered as an isotropic homogeneous medium, thus all the thermophysical properties are uniform in the domain; moreover, they are constant and not depending on temperature;
- The ground has a known initial temperature, which is equal to the undisturbed ground temperature;
- The boundary conditions at the ground surface and the far end of the ground domain are set equal to the undisturbed ground temperature.

With those assumptions, it is possible to deduce the temperature field into the ground considering Equation (1):

$$\rho c_p \frac{\partial T}{\partial \tau} = \frac{\partial}{\partial x} \left(k \frac{\partial T}{\partial x} \right) + \frac{\partial}{\partial y} \left(k \frac{\partial T}{\partial y} \right) + \frac{\partial}{\partial z} \left(k \frac{\partial T}{\partial z} \right) \quad (1)$$

The homogeneity of the ground can be used to obtain Equation (2):

$$\frac{1}{\alpha} \frac{\partial T}{\partial \tau} = \frac{\partial^2 T}{\partial x^2} + \frac{\partial^2 T}{\partial y^2} + \frac{\partial^2 T}{\partial z^2} \quad (2)$$

Where $\alpha = k/(\rho c_p)$ is the thermal diffusivity of ground.

Equation (2) can be written using also a polar coordinate system, obtaining Equation (3).

$$\rho c_p \frac{\partial T}{\partial \tau} = \frac{1}{r} \frac{\partial}{\partial r} \left(kr \frac{\partial T}{\partial r} \right) + \frac{1}{r^2} \frac{\partial}{\partial \theta} \left(k \frac{\partial T}{\partial \theta} \right) + \frac{\partial}{\partial z} \left(k \frac{\partial T}{\partial z} \right) \quad (3)$$

Again, the assumption of homogeneity of ground can be used to obtain Equation (4):

$$\frac{1}{\alpha} \frac{\partial T}{\partial \tau} = \frac{1}{r} \frac{\partial}{\partial r} \left(r \frac{\partial T}{\partial r} \right) + \frac{1}{r^2} \frac{\partial^2 T}{\partial \theta^2} + \frac{\partial^2 T}{\partial z^2} \quad (4)$$

When dealing with heat sources that show a cylindrical shape, like in the case of ground heat exchangers. it is frequently possible to introduce also the assumption of one-dimensional heat flux. With this assumption, it is possible to consider the temperature of the ground only function of the radial coordinate r and independent from the azimuthal angle θ and the axial coordinate z [12].

Under this assumption, Equation (4) can be rewritten in a simpler form, given by Equation (5):

$$\frac{1}{\alpha} \frac{\partial T}{\partial \tau} = \frac{1}{r} \frac{\partial}{\partial r} \left(r \frac{\partial T}{\partial r} \right) \quad (5)$$

Considering the more general case described by Equation (4), it can be solved by imposing a set of boundary conditions, that can be different, depending on the physics of the problem considered. For instance, it is possible to impose a constant heat flux. The methods that can be used for solving this equation can be either numerical or analytical, and each one has some limitations or intrinsic issues. Analytical solutions are mathematical expressions, but often they are difficult to apply for the complex mathematical formulation of the solution. Moreover, each solution is derived for the considered BHE geometry. This is a limit to the versatility of the solution because changing the shape of the BHE implies also to change the equation that expresses the solution. On the other hand, numerical methods are more simply implemented and offer more versatility of use, but the application is necessarily linked to the discretization of the spatial domain. For these reasons, often Equation (4) is approximated using simplified expressions.

In this thesis, a new semi-analytical method is proposed, called Multi Point Source (MPS) method, to overcome both the disadvantages of using pure analytical or pure numerical approaches, while maintaining good results in terms of precision and low computational time.

2.3. Ground Temperature Response Factor: Classical Analytical Solutions

Designing a Ground Heat Exchanger (GHE) requires the knowledge of the thermal behavior of ground during the operational time of the GCHP, which behavior is not only depending on the thermophysical properties of the ground but also on the bore field geometry (length and number of boreholes, aspect ratio of the single borehole) and the building loads. Thus, to study the ground heat transfer process it is necessary to know its temperature field both in time and space. For this purpose, it is common practice to introduce a non-dimensional temperature response factor, usually known as g-function. The g-function describes the temperature change into the ground (in time) with respect to the undisturbed value when a constant heat flux per unit length is imposed.

A general expression for the g-function is given by Equation (6)

$$\Gamma = \frac{2\pi k_{gr}(T - T_{gr,\infty})}{\dot{Q}'} \quad (6)$$

The g-functions are depending on non-dimensional parameters that account for time and borefield geometry. In particular, the dependency from time is expressed by a proper Fourier number, based on the characteristic length that is considered (it can either be a radial distance – FO_r - or the borehole length - FO_H).

Equation (7) can be used to link the two Fourier's numbers:

$$FO_r = FO_H \frac{H^2}{r_b^2} \quad (7)$$

In the following paragraphs, the most relevant analytical models are presented, starting from the single point source model up to cylindrical and helix source ones.

2.3.1. Single Point Source Solution

The Single Point Source (SPS) solution is of fundamental interest for the work explained in this thesis. Starting from this solution it is possible to obtain the temperature response function for a given geometry of the bore field, using the superposition principle. The single point source solution is the solution for the conduction equation in a mono-dimensional case, under the hypothesis of spherical spatial domain. Some further assumptions are considered to obtain the single point source solution:

- The heat injection at the point source is started at a specific time and the heat flux is constant;
- There is perfect contact between the source and the adjacent ground so that there is only pure conduction;
- There is no influence from groundwater flow and other adjacent boreholes.

Under these assumptions, it is possible to obtain Equation (8) which expresses the temperature field T as a function of the radial distance r (distance from the point source at which the temperature T is evaluated) and the time τ .

$$T(r, \tau) - T_{gr, \infty} = \frac{\dot{Q}}{2\pi kr} \operatorname{erfc} \left(\frac{1}{2\sqrt{Fo_r}} \right) \quad (8)$$

here:

- $T_{gr, \infty}$ is the undisturbed ground temperature [$^{\circ}\text{C}$];
- \dot{Q} is the heat flux [W];
- k is the ground thermal conductivity [W/m $^{\circ}\text{C}$];
- Fo_r is the Fourier's number calculated for the radial distance r ;
- erfc is the complementary error function;

2.3.2. Infinite Line Source

The first application of the superposition principle of the SPS solution is the Infinite Line Source (ILS) solution. It was firstly proposed by Lord Kelvin [13], then described in detail by Ingersoll et al [14] following the previous work of Carslaw and Jaeger [15]. The solution is valid under the same assumptions made for the SPS solution but assuming that the source is not a single point but rather an infinite line.

The heat flux is considered only in the normal direction with respect to the source length, and the ground has initial homogeneous temperature. This model is useful in case of narrow boreholes, with a small diameter compared to the length.

With the previous assumptions, it is possible to write Equation (9):

$$\Gamma_{ILS}(r, t) = 2 \cdot \int_{1/4Fo}^{\infty} \frac{e^{-\beta}}{\beta} d\beta = 2 \cdot E_1 \left(\frac{1}{4Fo_r} \right) \quad (9)$$

This formulation of the ILS solution contains the exponential integral function E_1 that can be approximated by different series expansions or tabulated values. Abramovitz and Stegun [16] proposed an approximation given by Equation (10):

$$E_1 = a_0 - \ln \left(\frac{1}{4Fo_r} \right) + \sum_{j=1}^5 a_j \left(\frac{1}{4Fo_r} \right)^j \quad (10)$$

With the coefficients a_0 and a_j assuming the following values:

| | |
|---------------------|--------------------|
| $a_0 = -0.57721566$ | $a_3 = 0.05519968$ |
| $a_1 = 0.99999193$ | $a_4 = -0.2491055$ |
| $a_2 = -0.24991055$ | $a_5 = 0.00107857$ |

Since Equation (10) approximates the integral function E_i it is necessary to give information about its accuracy:

- If $Fo_r > 0.25$: the accuracy is within 10%;
- If $Fo_r > 2$: the accuracy is within 1%;

Given the timescale usually considered when dealing with GHE (mainly years), it is clear that this approximation has good accuracy. In fact, considering a standard value of thermal diffusivity equal to 1.46 [m²/s], a borehole radius of 0.45 [m] and a depth of 10 [m], $Fo_r=2$ for a time of about 20 minutes.

2.3.3. Finite Line Source

In real heat exchanger analysis, it is convenient to discard the hypothesis of infinite length of the heat source and to consider a finite line source. It is possible to superpose in space the SPS solution, considering the ground as an infinite homogeneous medium thus obtaining the Finite Line Source in an Infinite Medium (FLSI) according to Equation (11):

$$\Gamma_{FLSI}(r, z, \tau) = \frac{1}{2} \cdot \int_0^H \left[\frac{\operatorname{erfc}\left(\frac{\sqrt{(z-h)^2 + r^2}}{2\sqrt{a\tau}}\right)}{\sqrt{(z-h)^2 + r^2}} \right] dh \quad (11)$$

Equation (11) allows calculating the temperature field at any point of coordinates (r, z) at a given time τ .

It is possible to discharge the hypothesis of considering ground as an infinite medium, obtaining the Finite Line Source solution in a Semi-Infinite Medium (FLS). To consider the ground as a semi-infinite medium it is necessary to use a series of image-sources (which are emitting a heat flux equal to the real sources, but with opposite sign) to maintain the temperature of the symmetry plane (which is representing the ground surface) constant and equal to $T_{gr, \infty}$.

Different research groups proposed a formulation of this solution, which is obtained using the superposition method in space. In particular, a Chinese research group [17] proposed a solution given by Equation (12):

$$\Gamma_{FLS}(r, z, \tau) = \frac{1}{2} \cdot \int_0^H \left[\frac{\operatorname{erfc}\left(\frac{\sqrt{(z-h)^2 + r^2}}{2\sqrt{a\tau}}\right)}{\sqrt{(z-h)^2 + r^2}} - \frac{\operatorname{erfc}\left(\frac{\sqrt{(z+h)^2 + r^2}}{2\sqrt{a\tau}}\right)}{\sqrt{(z+h)^2 + r^2}} \right] dh \quad (12)$$

Equation (12) allows calculating the temperature field at a given time τ for any point with coordinates (r, z) . More recently, Lamarche and Beauchamp [18] proposed a solution that is averaging the temperature along the z -axis, for the borehole depth H . Equation (13) provides the expression of this solution:

$$\Gamma_{FLS \text{ ave}}(r, \tau) = \left[\int_{\beta}^{\sqrt{\beta^2+1}} \frac{\operatorname{erfc}(\gamma \cdot z)}{\sqrt{z^2 - \beta^2}} dz - D_A - \int_{\sqrt{\beta^2+1}}^{\sqrt{\beta^2+4}} \frac{\operatorname{erfc}(\gamma \cdot z)}{\sqrt{z^2 - \beta^2}} dz - D_B \right] \quad (13)$$

where:

- $\gamma = \frac{1}{(2\sqrt{FOH})}$ [-] represent the dimensionless time;
- $\beta r/H$ [-] is the dimensionless radial distance.

D_A and D_B are given by Equations (14) and (15) respectively:

$$D_A = \sqrt{\beta^2 + 1} \cdot \operatorname{erfc}(\gamma \cdot \sqrt{\beta^2 + 1}) + \beta \cdot \operatorname{erfc}(\gamma \cdot \beta) - \frac{e^{-\gamma^2(\beta^2+1)} - e^{-\gamma^2\beta^2}}{\beta\sqrt{\pi}} \quad (14)$$

$$D_B = \sqrt{\beta^2 + 1} \cdot \operatorname{erfc}(\gamma \cdot \sqrt{\beta^2 + 1}) + 0.5 \left[\beta \cdot \operatorname{erfc}(\gamma \cdot \beta) + \sqrt{\beta^2 + 4} \cdot \operatorname{erfc}(\gamma \cdot \sqrt{\beta^2 + 4}) \right] - \frac{e^{-\gamma^2(\beta^2+1)} - 0.5[e^{-\gamma^2\beta^2} + e^{-\gamma^2(\beta^2+4)}]}{\beta\sqrt{\pi}} \quad (15)$$

A new expression for the FLS solution has been also proposed in 2011 by Claesson and Javed [19]. In this formulation, the distance D represents the distance of the finite linear source from the ground surface, i.e. the “buried depth” of the ground heat source. This formulation is given by Equation (16):

$$\Gamma_{FLS\ ave}(r, \tau) = \frac{1}{2} \cdot \left[\int_{\sqrt{\frac{1}{4FOH}}}^{\infty} \exp \left[-\left(\frac{r}{H}\right)^2 z^2 \right] \cdot \frac{Y\left(z, \frac{D}{H} \cdot z\right)}{z^2} dz \right] \quad (16)$$

$Y(x, y)$ can be expressed using Equation (17):

$$Y(x, y) = 2ierf(x) + 2ierf(x + 2y) - ierf(2x + 2y) - ierf(2y) \quad (17)$$

Where

$$ierf(U) = \int_0^U \operatorname{erf}(v) dv = U \cdot \operatorname{erf}(U) - \frac{1}{\sqrt{\pi}} (1 - e^{-U^2}) \quad (18)$$

2.3.4. Infinite Cylindrical Source

This solution has been proposed by Carslaw e Jaeger [15] and it is valid under assumptions very similar to the ones made for the ILS solution, but considering the heat source as a cylindrical “hollow” surface. The “hollow” definition means that the heat capacity of the material inside the cylindrical surface is neglected.

Carslaw and Jaeger solved the problem using two different kinds of boundary conditions, which in turn lead to two different solutions, namely imposed constant heat flux and constant temperature.

The Equations (19) and (20), represent the two solutions, also called, respectively, G and F solutions.

$$\Gamma_{ICS\ Q}(r, \tau) = 2\pi \cdot G \left(Fo_{r,cyl}, p = \frac{r}{r_{cyl}} \right) = \frac{2}{\pi} \int_0^{\infty} \frac{e^{-\beta^2 \cdot Fo_{r,cyl}} - 1}{J_1^2(\beta) + Y_1^2(\beta)} [J_0(p\beta)Y_1(\beta) - J_1(\beta)Y_0(p\beta)] \frac{1}{\beta^2} d\beta \quad (19)$$

$$\Gamma_{ICS\ T}(r, \tau) = \frac{2\pi}{F(Fo_{r,cyl})} = \frac{\pi^2/4}{\int_0^{\infty} \frac{e^{-\beta^2 \cdot Fo_{r,cyl}} - 1}{J_0^2(\beta) + Y_0^2(\beta)} \frac{1}{\beta} d\beta} \quad (20)$$

Both expressions contain the Bessel functions, J and Y, of the zeroth and first order. Recently, Fossa [20] proposed an approximation for the ICS solution when a constant heat flux is considered as a boundary condition, given by Equation (21):

$$\Gamma_{ICS\ Q}(r = r_{cyl}, \tau) = 2\pi \cdot \left[\sum_{j=0}^6 c_j \text{Log}^j_{10}(Fo_{r,cyl}) \right] \quad (21)$$

The coefficients c_j are defined as follows:

Table 1: Coefficients for Equation (20)

| | |
|------------------------------|-----------------------------|
| $c_0 = 1.2777 \text{ E-1}$ | $c_4 = -1.4459 \text{ E-3}$ |
| $c_1 = 1.0812 \text{ E-1}$ | $c_5 = 3.6415 \text{ E-4}$ |
| $c_2 = 3.0207 \text{ E-2}$ | $c_6 = -2.4889 \text{ E-5}$ |
| $c_3 = -2.30337 \text{ E-3}$ | |

Equation (21) is approximating the analytical solution with an error smaller than 1% [20].

2.4. Analytical Solution for Geothermal Piles

The previous paragraph presented some fundamental models that are usually used to study long and narrow heat exchangers.

When dealing with geopiles, the assumption of a long and narrow heat exchanger is no longer valid, because the aspect ratio of those structures is lower compared to typical boreholes. Geopiles usually have a diameter around one meter, while the depth can be up to several meters (15m is a typical value for building piles). Moreover, the inner mass of the cylindrical volume of the pile induces a not negligible effect on the thermal capacity of the system. This typology of short ground heat exchangers is often shaped like a helix (Helix Heat Exchangers - HHE), because this shape allows coiling the pipes around the building pile. In this way, it is possible to obtain more compact heat exchangers, maintaining the total length of the pipe unaltered, but reducing greatly the drill depth necessary for the

installation. Maintaining the total length unaltered is crucial for keeping constant the heat flux exchanged with the ground.

It appears clear why it is necessary to find new models able to properly describe the heat transfer in the ground in case of HHE. In the following paragraph, different analytical models will be briefly illustrated, with reference to both infinite and finite length sources. For all the models analyzed, the boundary condition used to obtain the solution is imposed constant heat flux per unit of borehole length. Moreover, for all the models dealing with finite length sources, the ground is assumed to be a semi-infinite medium, whose surface temperature is maintained constant and equal to $T_{gr,\infty}$.

The presented analytical models were developed recently by a Chinese research group through the application of Green's function theory.

Man et al. (2010 - 2011) and Cui et al. (2011) [21], [22], [23] proposed several models dealing with GHE different in shape and length:

- Infinite and Finite Solid Cylindrical Source models;
- Infinite and Finite Ring Source models;
- Infinite and Finite Spiral Source models.

2.4.1. Infinite and Finite Solid Cylindrical Source models

Both models have been proposed by Man et al. [22] to improve the existing "hollow" cylindrical model (i.e. the ICS solution). This model considers the thermal mass inside the cylindrical surface and its effect on the heat transfer phenomenon in the ground.

The Infinite Solid Cylindrical Source (ISCS) solution is given by Equation (22):

$$\Gamma_{ISCS}(r, \tau) = -\frac{1}{2} \cdot \int_0^\pi \frac{1}{\pi} \cdot E_i \left(-\frac{r^2 + r_{pile}^2 - 2r \cdot r_{pile} \cos \varphi}{4a\tau} \right) d\varphi \quad (22)$$

Equation (22) is depending also on the angular coordinate φ , while Equation (23) is describing the Finite Solid Cylindrical Source (FSCS) solution:

$$\Gamma_{FSCS}(r, z, \tau) = \frac{1}{4} \cdot \int_0^\tau \frac{1}{\tau} \cdot I_0 \left[\frac{r \cdot r_{pile}}{2a\tau} \right] \cdot \exp \left[-\frac{r^2 + r_{pile}^2}{4a\tau} \right] \cdot \left\{ \operatorname{erf} \left[\frac{H-z}{2\sqrt{a\tau}} \right] + 2\operatorname{erf} \left[\frac{z}{2\sqrt{a\tau}} \right] - \operatorname{erf} \left[\frac{H+z}{2\sqrt{a\tau}} \right] \right\} d\tau \quad (23)$$

The FSCS model allows knowing the temperature field at a specific depth z , considering the total pile height as H . I_0 is the modified Bessel Function of zeroth order.

2.4.2. Infinite and Finite Ring Source models

To better assess the real pipe layout of an HHE, Cui et al. [21] developed two models in which the heat source is not a cylinder but a series of stacked rings. In this way, it is possible to account for the discontinuities between the coiled pipes that are present in

real HHE configurations. The ring coils are stacked along a vertical axis (the z-axis) and they are spaced by a certain distance p which is referred to as the coil pitch.

Equation (24) gives the expression of the Infinite Ring Source (IRS) solution:

$$\Gamma_{IRS}(r, z, \tau) = \frac{p/r_{pile}}{4\sqrt{\pi}} \cdot \sum_{n=0}^{\infty} \int_0^{Fo} \frac{1}{Fo_{rpiled}^{\frac{3}{2}}} \cdot I_0 \left[\frac{r/r_{pile}}{2Fo_{rpiled}} \right] \cdot \exp \left[-\frac{(r/r_{pile})^2 + 1}{4Fo_{rpiled}} \right] \cdot \left\{ \exp \left[-\frac{\left(\frac{z - n \cdot p - 0.5 \cdot p}{r_{pile}} \right)^2}{4Fo_{rpiled}} \right] + \exp \left[-\frac{\left(\frac{z + n \cdot p + 0.5 \cdot p}{r_{pile}} \right)^2}{4Fo_{rpiled}} \right] \right\} dFo_{rpiled} \quad (24)$$

If the hypothesis of infinite source is left, and the HHE is modeled as a finite source, it is possible to consider the heat exchanger as a series of m rings, spaced by the pitch p and stacked vertically along the z-axis, up to the total pile depth H . With this discretization of the heat source, it is possible to obtain the Finite Ring Source (FRS) solution, expressed by Equation (25):

$$\Gamma_{FRS}(r, z, \tau) = \frac{p/r_{pile}}{4\sqrt{\pi}} \cdot \int_0^{Fo} \frac{1}{Fo_{rpiled}^{\frac{3}{2}}} \cdot I_0 \left[\frac{r/r_{pile}}{2Fo_{rpiled}} \right] \cdot \exp \left[-\frac{(r/r_{pile})^2 + 1}{4Fo_{rpiled}} \right] \cdot \sum_{n=0}^m \left\{ \exp \left[-\frac{\left(\frac{z - n \cdot p - 0.5 \cdot p}{r_{pile}} \right)^2}{4Fo_{rpiled}} \right] - \exp \left[-\frac{\left(\frac{z + n \cdot p + 0.5 \cdot p}{r_{pile}} \right)^2}{4Fo_{rpiled}} \right] \right\} dFo_{rpiled} \quad (25)$$

The previous expression contains the modified Bessel Function of zeroth order, I_0 .

2.4.3. Infinite and Finite Spiral Source models

To further refine the modeling of the HHE, Man et al. [23] represented the layout of the buried heat source as a helix, coiled around the central vertical z-axis with a coil pitch p .

Man et al. studied two different models, dealing both with the infinite source hypothesis and the finite one.

The Infinite Spiral Source (ISS) solution is hereby presented using Equation (26):

$$\Gamma_{ISS}(r, \varphi, z, \tau) = \frac{p/r_{pile}}{8 \cdot \pi\sqrt{\pi}} \cdot \int_0^{Fo} \frac{1}{Fo_{rpiled}^{\frac{3}{2}}} \cdot \int_{-\infty}^{\infty} \exp \left[-\frac{(r/r_{pile})^2 + 1 - 2(r/r_{pile}) \cdot \cos(\varphi - \varphi') + \left(\frac{z - p \cdot \varphi'/2\pi}{r_{pile}} \right)^2}{4 \cdot Fo_{rpiled}} \right] d\varphi' \cdot dFo_{rpiled} \quad (26)$$

When dealing with a finite length helix, it is possible to refer to the Finite Spiral Source (FSS) solution, given by Equation (27):

$$\Gamma_{FSS}(r, \varphi, z, \tau) = \frac{p/r_{pile}}{8 \cdot \pi \sqrt{\pi}} \cdot \int_0^{Fo} \frac{1}{Fo_{r_{pile}}^{\frac{3}{2}}} \cdot \exp \left[-\frac{(r/r_{pile})^2 + 1}{4Fo_{r_{pile}}} \right] \cdot \int_0^{2\pi H/b} \exp \left[\frac{2(r/r_{pile}) \cdot \cos(\varphi - \varphi')}{4Fo_{r_{pile}}} \right] \cdot \left\{ \exp \left[-\frac{\left(\frac{z - p \cdot \varphi' / 2\pi}{r_{pile}} \right)^2}{4Fo_{r_{pile}}} \right] - \exp \left[-\frac{\left(\frac{z + p \cdot \varphi' / 2\pi}{r_{pile}} \right)^2}{4Fo_{r_{pile}}} \right] \right\} d\varphi' \cdot dFo_{r_{pile}} \quad (27)$$

In the previous expression, the helix heat source is of finite length H , and it is composed of m spiral coil stacked along a common vertical axis.

2.5. The innovative Multiple Point Source (MPS) model

In this paragraph, the innovative MPS method will be described in detail, giving information on how it is derived, validated and applied to a sample application. The MPS method is a semi-analytical method based on the spatial superposition of the SPS source, whose main feature is the extreme flexibility of application to any GHE shape and the low requirements in terms of computational time, with respect to the standards analytical solutions and the commercial software based on Finite Element Models (FEM).

The Multiple Point Source is a semi-analytical method based on the superposition in space of the Single Point Source (SPS) solution, ref. Equation (8), that can be used to calculate the temperature response factor in case of irregular layout of the heat source, like a helix or more complicated arrangements.

The ground is considered as an isotropic semi-infinite medium with constant thermophysical properties. The surface temperature is set equal to the undisturbed ground one ($T_{gr,\infty}$) and it is maintained constant using the mirror source approach: a set of identical images is superposed using the ground surface as a symmetry plane. Each of the mirror sources emits a heat flux equal to the corresponding real one, but the heat flux is opposite in sign. In this way, since the ground acts as a symmetry axis, the temperature at the interface is maintained constant and equal to $T_{gr,\infty}$.

Considering the ground domain, it is possible to evaluate the temperature excess with respect to $T_{gr,\infty}$, for every j -th position, considering the effects induced not only by the real sources in the ground but also by the image ones. In this way, for every timestep τ it is possible to calculate Equation (28):

$$T_j(\tau) - T_{gr,\infty} = \sum_{i=1}^{N_{sources}} T_{i,j}(\tau) - T_{gr,\infty} \quad (28)$$

$N_{sources}$ accounts for all the sources, both real and imaginary ones.

Now it is possible to apply the SPS solution (Equation (8)), obtaining Equation (29):

$$T_j(\tau) - T_{gr,\infty} = \frac{\dot{Q}}{4\pi k_{gr}} \sum_{i=1}^{N_{sources}} \frac{1}{r_{i,j}} \operatorname{erfc}\left(\frac{1}{2\sqrt{(Fo_r)_{i,j}}}\right) \quad (29)$$

From Equation (29) it is possible to average the temperature excess with respect to all the j -th positions, obtaining Equation (30):

$$\bar{T}(\tau) - T_{gr,\infty} = \frac{1}{N_{positions}} \sum_{j=1}^{N_{positions}} T_j(\tau) - T_{gr,\infty} \quad (30)$$

2.5.1. Source Discretization Analysis

One of the most critical aspects of applying the MPS method is to correctly choose the discretization of the heat source. This is fundamental because a poor choice can either have effects on the accuracy of the results (if the discretization is too coarse) and on the computational time (if it is too fine). Discretizing the heat source means to choose the number of point sources that will be superimposed during the calculation.

From a geometrical point of view, imposing the number of sources is equal to define a specific distance between them. If the distance is too big, the number of sources is too small, and the discretization is too coarse. Vice versa, if the distance is very small, the sources are very numerous, and the calculation might become too demanding from the computational time point of view. Usually, a finer discretization produces results more accurate, but the drawback in terms of increased simulation time might outbalance the enhanced accuracy. For these reasons, it is important to establish a general criterion able to offer a good compromise between accuracy and computational time.

However, defining the maximum allowable distance between source points (SP) necessarily involves the evaluation of another geometrical parameter: the distance of each point source to the closer evaluation point (EP).

Figure 4 briefly sketches how the discretization problem can be assessed. Considering a generic line, it is possible to position the single point sources (PSs) at a generic distance Δs .

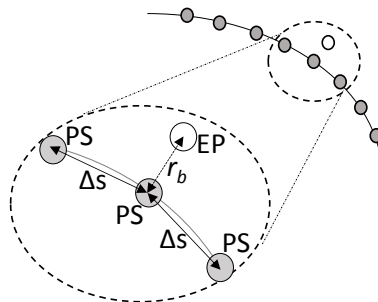


Figure 4: Generic line discretization example

It is important to notice that the evaluation point is not on the line, but it is placed at a distance r_b normal to the generic line. This allows to completely neglect the presence of the grout thermal resistance, during the model application, because the distance r_b is already considering the dislocation of the Evaluation Point with respect to the Point Source.

From Figure 4 it is also possible to individuate the ratio $\Delta s/r_b$ which can be considered the main discretization parameter. In order to individuate a general criterion for the choice of $\Delta s/r_b$, a series of preliminary calculations and considerations have been performed, with respect to some reference analytical solutions.

The first case studied was the comparison between the MPS method application and the FLS analytical solution, to firstly investigate a linear source model.

The results of this first analysis are illustrated in Figure 5: it is clearly visible that the curve obtained with $\Delta s/r_b=4$ is not in good agreement with the reference FLS result. The reference FLS results have been calculated imposing $r_b/H=10E-3$. Reducing $\Delta s/r_b$ increases sensibly the accuracy of the MPS superposition results, with the curve obtained with $\Delta s/r_b=1$ being in very good agreement with the proposed reference solution.

The second comparison was made for a stacked ring coil heat exchanger that is one of the possible approximations for an HHE. For clarity sake, Figure 6 sketches the ring coil configuration with the main parameters.

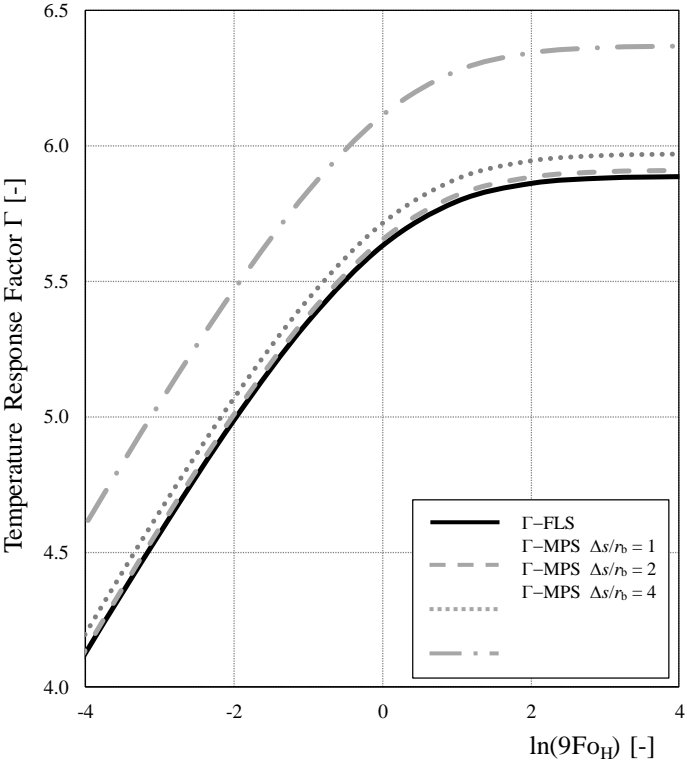


Figure 5: Comparison between MPS method results (with different $\Delta s/r_b$) and reference FLS results (calculated with $r_b/H = 10E-3$)

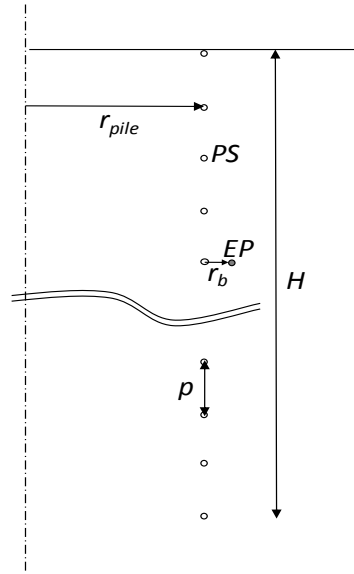


Figure 6: HHE approximated as a series of stacked ring coils

With:

- $r_{pile} = 0.45$ [m]
- $r_b = 0.02$ [m]
- $\rho = 0.5$ [m]
- $H = 15$ [m]

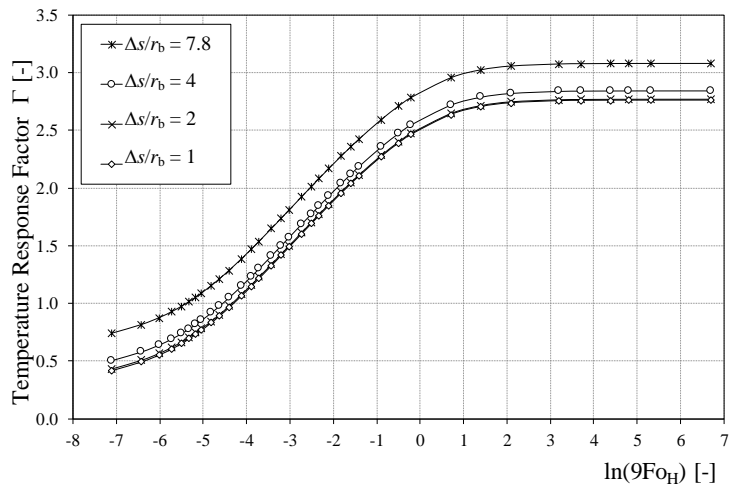


Figure 7: Effect of heat source discretization in case of stacked ring coils heat exchanger

Different calculations have been performed, with the ring coils being discretized using increasing PS to obtain a value of $\Delta s/r_b=1$, corresponding to $N_{PS}=140$.

The results of the comparisons between the Thermal Response Factors (obtained applying the MPS method) calculated with different number of PS are reported in Figure 7.

Analyzing Figure 7, it is clear that increasing the number of PS is beneficial for the accuracy of the results. To better understand the effect of the $\Delta s/r_b$ parameter, the relative error between the different results have been calculated, according to Equation (31):

$$\varepsilon\% = ave \left| \frac{\Gamma_i - \Gamma_{i+1}}{\Gamma_{i+1}} \right| \% \quad (31)$$

The results of the average relative errors evaluation are reported in Table 2:

Table 2: Ring coil heat exchanger discretization parameter average error analysis

| N_{ps} | $\Delta s = 2 \cdot \pi \cdot r_{pile} / N_{ps}$ | $\Delta s / r_b$ | $\varepsilon\%$ |
|----------|--|------------------|-----------------|
| 18 | 0.16 | 7.8 | - |
| 35 | 0.08 | 4 | 17.8% |
| 70 | 0.04 | 2 | 6.1% |
| 140 | 0.02 | 1 | 0.9% |

The results are important to establish which is the best discretization criterion, considering the specific case of stacked ring coils heat exchanger. In fact, looking at the last column of Table 2, the relative error between the results obtained comparing $\Delta s/r_b = 1$ and $\Delta s/r_b = 2$ is just 0.9%. This means that results with a discretization parameter $\Delta s/r_b = 1$ are not substantially more precise with respect to those obtained for $\Delta s/r_b = 2$. This means that the latter offers the best balance between calculation time and results accuracy.

2.5.2. MPS Method Validation with Literature Analytical Solutions

This paragraph is devoted to the validation of the MPS method results by the comparison with the temperature response factor calculated from literature analytical solutions (refer to paragraph 2.3). This part is very important to correctly assess the reliability of the method.

The HHE has been modeled as a series of rings stacked vertically, equivalent to the geometry represented in Figure 6. The results of the application of the MPS method to this geometry have been compared to the results obtained from the reference analytical solutions:

- Infinite solid cylindrical source (ISCS);
- Finite solid cylindrical source (FSCS);
- Infinite ring coil source (IRS);
- Finite ring coil source (FRS).

The geometrical parameters considered for all the calculations are listed in Table 3.

Table 3: Geometrical Parameters for HHE model

| Geometrical Parameter | Value |
|-----------------------|----------|
| H | 15 [m] |
| r_{pile} | 0.45 [m] |
| p | 0.5 [m] |
| r_b | 0.02 [m] |
| N_{EP} | 10 [-] |

The number of evaluation points (N_{EP}) for every pitch distance (p) is equal to 10. Thus, their number is greater than the number of rings present (H/p) in the whole depth H , to evaluate the temperature response factor (Γ) also in positions far from the Point Sources (PS) that compose the ring approximation. Evaluating Γ in Evaluation Points (EP) that are far from the PS will produce lower values compared to the values obtained with EPs that are closer to the PS. For this reason, the asymptotic value of the Temperature Response Factors shown in Figure 8 will be lower than those shown in Figure 7.

An important remark about the results in Figure 8 is that for low Fo values (meaning $\ln(9Fo_H) < -4$, which correspond to $Fo_{rb} < 2$) all the solutions must match with the ILS trend. This is because, at the beginning of the heat injection, the Evaluation Points are behaving as they are not influenced by neighbor sources, thus they behave like single points of an infinite line.

In Figure 8 the IRS is falling below the other solutions, and it is not clear if this is related to the Matlab solver used to integrate Equation (24) or some inefficiencies of the analytic expression itself. For high Fo , the application of the MPS method clearly shows that the results obtained are in very good agreement with the reference analytical solutions results. Applying Equation (31) allows estimating the average relative error between the MPS results and the FSCS and FRC solutions. The average relative error calculated is equal to 2.8% and 1.8%, respectively.

2.5.3. MPS Method Validation with Two-Dimension FEM Model

To further validate the MPS method, a comparison with two FEM models (using Comsol) has been carried out.

The HHE has been modeled as a stacked ring coil heat source (FRS), for both the MPS method and the Comsol Model. The geometrical parameters of the heat exchanger are listed in Table 4.

Like in the previous simulations, the temperature field is not evaluated at the ring interface, but at a distance r_b .

The boundary condition imposed for the Comsol FEM model was a constant heat rate at the ring external surface.

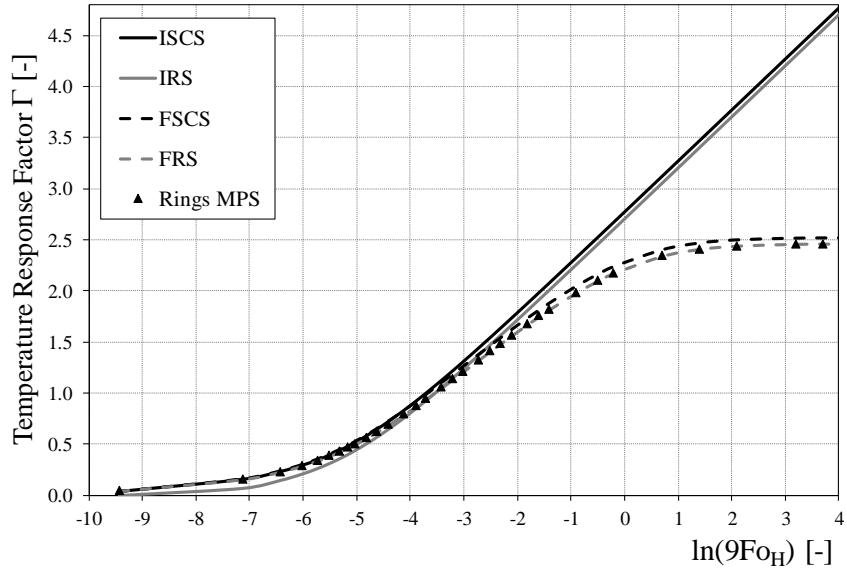


Figure 8: Comparison between MPS method results and reference Analytical Solutions for stacked ring coil heat exchanger

Table 4: FRS Geometrical Parameters used for the FEM model

| Geometrical Parameter | Value |
|-----------------------|----------|
| H | 15 [m] |
| r_{pile} | 0.45 [m] |
| ρ | 0.25 [m] |
| r_b | 0.02 [m] |

Knowing the temperature field both in space and time from Comsol simulations allows the application of the Equation (32):

$$\Gamma_L = 2\pi k_{gr} \frac{T - T_{gr,\infty}}{\dot{Q}'_L} = \Gamma \cdot \frac{H}{L} \quad (32)$$

It is important to note that, here, the heat flux \dot{Q}'_L is referred to the unit helix length, and not to the unit pile depth (\dot{Q}'). This was necessary to compare the Γ -functions in the same form. Figure 9 compares the two thermal response factors and, by observing it, it is immediate to notice that, the two curves are in very good agreement, during the initial phase as well as during the stationary long-term asymptotic trend.

Performing once again the average relative error analysis, using Equation (31), one can discover that the average difference is equal to 2.5%, which is in line with the average errors calculated In Paragraph 2.5.2.

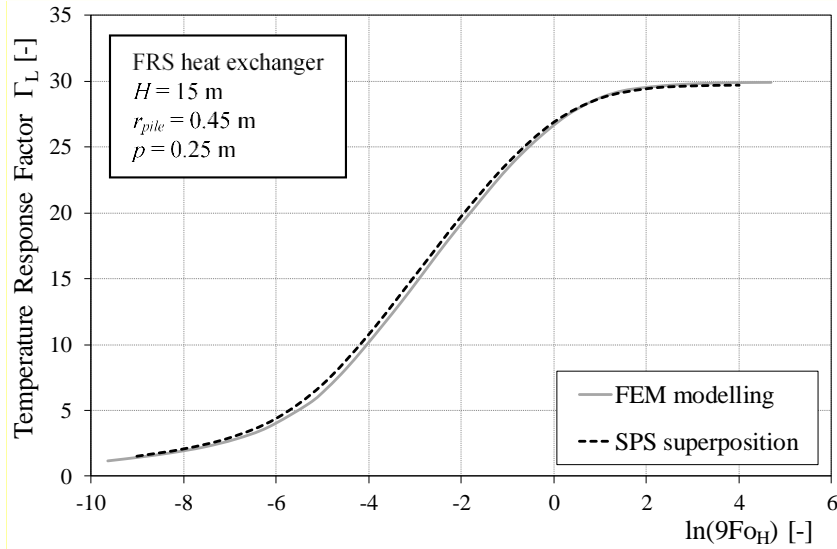


Figure 9: Comparison between the Γ_L -functions between MPS results and FEM results.

2.5.4. MPS Method Application and Results Discussion

After presenting and validating the method against both analytical solutions and FEM simulations results, it is possible to apply the MPS model to two shapes for geopile applications.

As stated before, the MPS method is incredibly flexible and, thus, can be used to obtain the ground thermal response factor for any heat exchanger shape and arrangement. This is especially useful when dealing with new approaches in the realization of geothermal heat exchangers, like the geopiles.

Geopiles are very important when considering the application of the geothermal energy exploitation to newly constructed buildings. In fact, it often is impossible to realize large scale low-enthalpy geothermal plants due to the huge amount of planar terrain required (if designing a horizontal field) or due to the high costs related to the drilling phase for vertical bore fields. Geopiles eliminates both the downside, allowing the integration of the geothermal heat exchanger directly into the building pile. This offers great flexibility for the application of the geothermal energy exploitation, as well as offering new horizons to its applicability.

The biggest downside is the lack of fast and reliable tools able to correctly model the heat transfer phenomena between the ground and the heat exchanger in case of the non-conventional layout of the heat exchanger.

For these reasons, the MPS method is of great utility when dealing with such innovative technical solutions for geothermal heat exchangers. The method has been applied to two scenarios that can be found when dealing with reals cases.

The first application is related to an HHE modeled as a series of vertically stacked rings. The second application deals with a series of vertical pipes connected horizontally with U-bends, at the top and bottom of the cylindrical volume. Figure 10 reports the sketch of the considered geometries. The geometrical parameters have been selected to have the same total heat exchangers length.

$$L = L_{rings} \cong L_{vertical\ pipes} \quad (33)$$

In Equation (33) the terms can be rewritten using Equation (34) and (35):

$$L_{rings} = 2\pi \cdot r_{pile} \cdot \frac{H}{p} \quad (34)$$

$$L_{vertical\ pipes} = N_{legs} \cdot H + 2\pi \cdot r_{pile} \quad (35)$$

The geometrical parameters for the heat exchangers shown in Figure 10 are reported in Table 5.

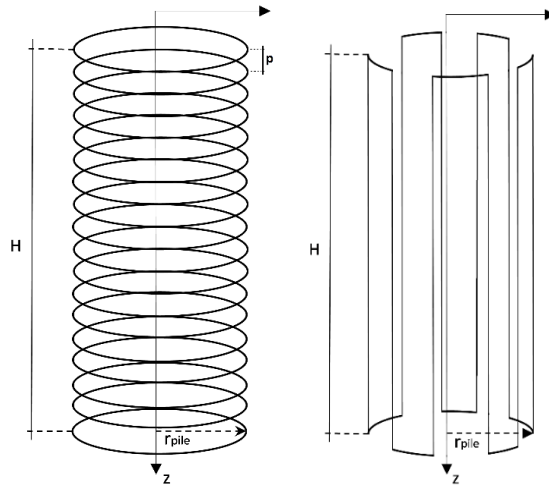


Figure 10: Heat exchangers configuration for the MPS application scenarios

Table 5: Geometrical parameters for stacked ring and vertical U-pipes configurations

| Geometrical Parameter | Value |
|-----------------------|----------|
| H | 15 [m] |
| r_{pile} | 0.45 [m] |
| p | 0.28 [m] |
| r_b | 0.02 [m] |
| N_{legs} | 10 [-] |

Using the parameters in Table 5 for calculating Equation (34) and (35), one finds that the total length for both the geometries is nearly equal to 150 m.

The application of the MPS superposition method to the proposed geometries allows finding interesting results, that are illustrated in Figure 11. Analyzing the results is easy to notice that for low Fourier's numbers ($\ln(9 Fo_H) < -1$), the two curves are in very good agreement and both match the SPS behavior. The reason for this is that at the beginning of the heat injection, the effect of each source on the ground surrounding it is limited by the thermal inertia of the ground itself. Thus, each source cannot perceive the effect on the ground temperature induced by the other sources and each one of them is considered as a single point source. This is equal to consider the response of the ground at the distance r_b from the point source almost the same as the one induced by a single point source.

At higher time scale ($\ln(9 Fo_H) > 2$) the difference between the two thermal response factors becomes not negligible. For the asymptotic part of the two curves, the percentual difference is approximately 1%.

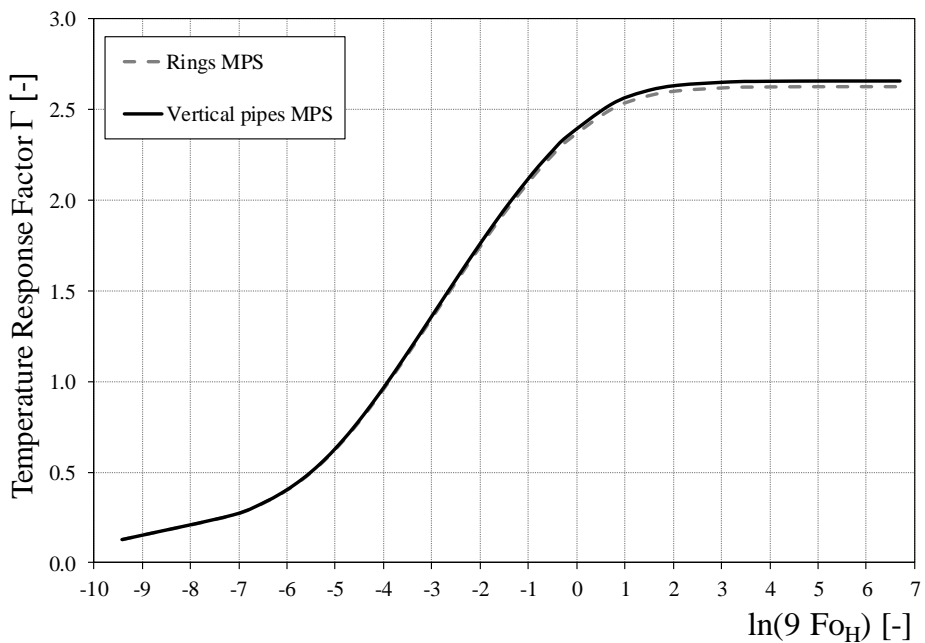


Figure 11: MPS application results confrontation between stacked ring and vertical U-pipe heat exchanger

3. Dynamic Simulation Model for the Smart Energy Building of the Savona Campus

The second part of the thesis is dedicated to extensively present the model developed with Energy Plus of the Smart Energy Building (SEB) located in the Savona Campus. The building is a Nearly Zero Emission Building (NZEB) that can boast some cutting-the-edge technological solutions for both the envelope and the energy system. For the latter, great care has been used to correctly include in the simulation the water-to-water and the air-to-air heat pumps that are present in the building. Partial validation of the model with real data has been carried out: the data were taken by the wide sensor network that monitors the SEB continuously.

3.1. The Savona Campus Smart Energy Building (SEB)

The SEB building is a nearly-Zero Emission Building located in the Savona Campus and realized by the University of Genova. It is connected to the Smart Poly-generation Microgrid (SPM) which feeds all the thermal and electrical users in the Campus. Figure 12 shows a draft of the connection between the SPM and the SEB.

Figure 12 also shows the sensor network that connects the SEB to the SPM. The sensors are used to collect a wide variety of data (i.e. thermal, electrical, indoor comfort, occupancy level) that are used to monitor and control the energy system operating conditions. Those data are collected and stored by an automatic acquisition system.

This connection between the SEB and the SPM allows to consider the building as an “Energy Prosumer”, able to produce thermal and electrical energy to satisfy its own requests, but also to exchange energy with the SPM in case of need.

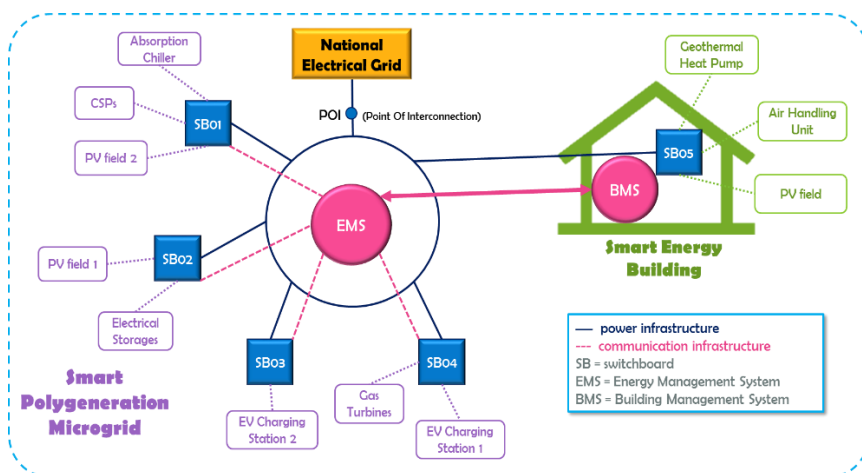


Figure 12: Savona Campus SPM-SEB connection draft



Figure 13: SEB building in Savona Campus

The building (in operation since February 2017) is characterized by the presence of:

- high-performance thermal insulation materials for the envelope,
- ventilated facades,
- a photovoltaic field (22 kWp) on the roof,
- extremely low consumption led lamps,
- a rainwater collection system,

and a thermal system composed by:

- *an air handling unit (AHU)*, installed on the roof, which performs functions such as circulating, cleaning and cooling/heating the air of the building;
- *a ground-coupled heat pump (GCHP)*, that produces cold/hot water to feed fancoils and radiators for cooling/heating purpose; the hot water is used during winter also for Domestic Hot Water (DHW) purposes;
- *an air source heat pump (ASHP)*, for DHW production purposes exclusively;
- *two solar thermal collectors*, for DHW production purposes exclusively.

3.2. Heating and Cooling Loads Evaluation

In this paragraph, it is briefly illustrated what is the concept of the heating and cooling loads for a building and the importance of estimating them when analyzing its energy performance. Moreover, it is presented a detailed description of the building masonry, glazed surfaces, shading, thermal zones (volumetric and operating conditions analysis). Then, the “Ideal Loads” model in EnergyPlus is widely described. The last part is dedicated to the presentation and discussion of the simulation results when the “Ideal Loads” hypothesis is considered.

3.2.1. Weather File Customization Using Elements

One of EnergyPlus most important input files is the weather file because it allows modeling the outdoor climatic conditions under several aspects. It contains time series for the entire year, with a time step of one hour. Usually, the time series are derived from the averaged data measured for the selected location (multi-year standard averaged series) and include precipitation, wind speed and direction, sky cloud coverage, solar irradiance (direct, diffused and global), relative and absolute air humidity, and other. The weather file also contains geographical information, like latitude, longitude, altitude and climatic area. Standard weather files can be provided as TMY (Typical Meteorological Year) files or EPW (Energy Plus Weather) files. EPW weather files are freely provided for some locations and downloadable as an additional resource for Energy Plus, directly from the software website.

3.2.2. The Ideal Loads Model in EnergyPlus

The “Ideal Load System” is a special option present in Energy Plus, which allows simulating the building without focusing on the HVAC system in detail. This system is an ideal unit that mixes air at the zone exhaust condition with the specified amount of outdoor air and then adds or removes heat and moisture at 100% efficiency to produce a supply airstream at the specified conditions. In this way, the results obtained are only depending on the building envelope thermal properties, on the internal and solar gains and do not depend on the HVAC system. The outputs of this type of model are the heating and cooling loads of the building and not the primary energy consumption of the thermal plants.

The Ideal Load System has some dedicated options that allow the user to input specific information for the system control:

- System availability for ventilation, heating, and cooling;
- Cooling and Heating Thermostat Temperature set points;
- Humidification and dehumidification set points;

- Supply maximum and minimum temperatures for cooling and heating;
- Outdoor air mass flow rates (minimum and maximum);
- Presence and functioning of heat recovery and economizer;

This simplification of the HVAC system is useful in the first stage of the building analysis since the simulations are focused on calculating the energy needs of the building. This can be very helpful in determining if there is some incongruence in the HVAC control system (i.e. inconsistent temperature set points, for cooling and heating), in the geometry (wrongly assigned thermal boundary conditions, for instance) and in the internal gains (unreasonable peak value or scheduled intervals).

Considering the nature of the “Ideal Loads” hypothesis, it is useful to introduce the building energy balance, which allows the estimation of the heating and cooling energy demand. Those quantities can be evaluated through EnergyPlus using the “Ideal Loads” option.

In general, it is possible to calculate the net energy needs of a building starting from an energy balance, which accounts for all the energy gains and losses.

The balance is different depending on the season considered. Considering the winter season, it is possible to sketch the ingoing and outgoing energy fluxes as shown in Figure 14.

The net heat energy loss can be calculated using Equation (36):

$$\dot{Q}_{net,out} = (\dot{Q}_{walls} + \dot{Q}_{windows} + \dot{Q}_{ceil} + \dot{Q}_{doors} + \dot{Q}_{inf} + \dot{Q}_{ground})_{out} - (\dot{Q}_{solar} + \dot{Q}_{people} + \dot{Q}_{plug\ loads})_{in} \quad (36)$$

The same approach can be used to evaluate the energy balance during the summer season, considering the building balance illustrated in Figure 15.

Then it is possible to write Equation (37) to calculate the net energy ingoing the building.

$$\dot{Q}_{net,in} = (\dot{Q}_{solar} + \dot{Q}_{people} + \dot{Q}_{plug\ loads} + \dot{Q}_{walls} + \dot{Q}_{windows} + \dot{Q}_{ceil} + \dot{Q}_{doors} + \dot{Q}_{inf})_{in} \quad (37)$$

Every term of Equations (36) and (37) can be calculated using EnergyPlus, to obtain more precise results that consider also the dynamic aspect of the energy exchange process. Even if the energy balances are given in a general and simple form, the precise evaluation of every term of Equations (36) and (37) is challenging when the time dependency of the problem is taken into consideration.

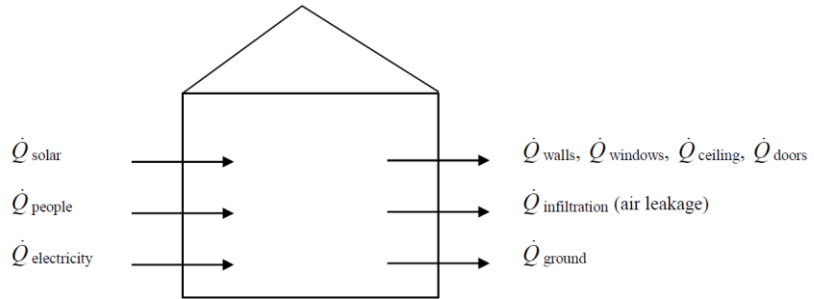


Figure 14: General winter energy balance for a building

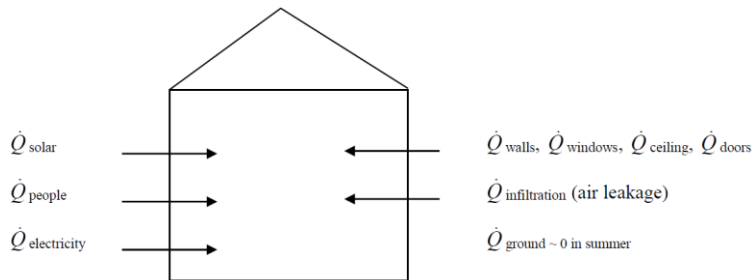


Figure 15: General summer energy balance for a building

3.2.3. Envelope and Geometrical Information

In this part, a detailed analysis of the masonry and glazed surfaced is presented. This part is very important to correctly model the envelope of the building and, subsequently, all the energy gains and losses through the external surfaces. Given the low-energy design of the building, all the materials were selected to offer very high thermal insulation performance, to minimize the energy dissipations during winter and the energy gains during summer. This is crucial to decrease the overall energy needs.

3.2.3.1. Masonry Analysis

To analyze more in detail the building, it is useful to start from the envelope and the geometry of the structure. The Savona Campus SEB is very interesting from this point of view: the material used for realizing the external façade has high thermal performance, contributing to the thermal insulation of the building. Moreover, the external walls have been covered with ventilated façades that add multiple benefits to furtherly reduce the energy requirements of the SEB. The ventilated façades are realized in a modular way, that allows avoiding the effects of the thermal bridges: every module is connected to the others by specifically designed linkages, that allows maintaining the continuity of the materials, effectively reducing the thermal bridge effects.

The external layer of all the façade is made of modular fiber-cement panels, that allow having mechanical resistance against accidental hit that could eventually damage the underlying insulant materials.

This material composition has been included in the simulation model, assigning the thermal properties listed in Table 6.

The roof, the inter-floor slab, and the ground slab have been characterized using the same approach. Table 7 and Table 8 report the stratigraphy and the thermal properties of each layer.

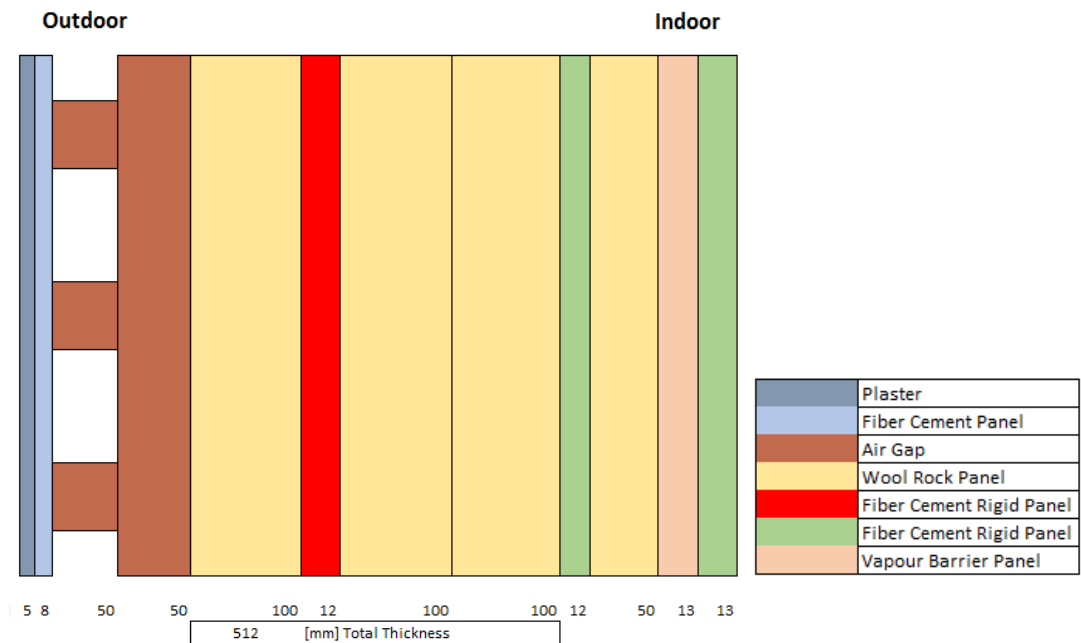


Figure 16: Ventiladed façade stratigraphy, layer thickness is reported in [mm]

Table 6: Thermal Properties for each material for external façades

| Materials | Thermal Conductivity [W/mK] | Density [kg/m ³] | Specific Heat capacity [J/kgK] |
|--------------------------|-----------------------------|------------------------------|--------------------------------|
| Plaster | 0.8 | 1600 | 1000 |
| Fibre Cement Panel | 0.39 | 1580 | 1050 |
| Mineral Wool Panel | 0.035 | 35 | 840 |
| Fibre Cement Rigid Panel | 0.35 | 1100 | 1200 |
| Fibre Cement Rigid Panel | 0.25 | 700 | 1000 |
| Vapour Barrier Panel | 0.21 | 700 | 1000 |

Table 7: Inter-floor and Roof slab thickness and thermal properties for each layer

| Materials | Thickness [mm] | Thermal Conductivity [W/mK] | Density [kg/m ³] | Specific Heat capacity [J/kgK] |
|--|-------------------|-----------------------------------|---------------------------------|---|
| Steel (roof only) | 1 | 52 | 7800 | 450 |
| Vinyl Floor Cover (inter-floor only) | 10 | 0.22 | 1200 | 1700 |
| Lean Concrete | 60 | 0.7 | 1600 | 880 |
| Bitumen Waterproofing | 1 | 0.17 | 1050 | 1000 |
| Expanded Polystyrene | 160 | 0.035 | 35 | 1250 |
| Aluminium Vapour Barrier | 1 | 200 | 2700 | 880 |
| "Prédalles" - type Prefabricated Slab | 400 | 0.952 | 1442 | 840 |
| Plaster | 15 | 0.8 | 1600 | 1000 |

Table 8: Ground slab thickness and thermal properties for each layer

| Materials | Thickness [mm] | Thermal Conductivity [W/mK] | Density [kg/m ³] | Specific Heat [J/kgK] |
|-----------------------------|-------------------|-----------------------------------|---------------------------------|-----------------------------|
| Vinyl Floor Cover | 10 | 0.22 | 1200 | 1700 |
| Lean Concrete | 60 | 0.7 | 1600 | 880 |
| Aluminium Vapour Barrier | 1 | 200 | 2700 | 880 |
| Expanded Polystyrene | 160 | 0.035 | 35 | 1250 |
| Gravel and Sand Concrete | 50 | 1.310 | 2000 | 0.88 |
| Non-ventilated Air Gap | 550 | 2.268 | 1 | 1050 |
| Lean Concrete | 60 | 0.7 | 1600 | 880 |
| Plaster | 15 | 0.8 | 1600 | 1000 |

3.2.3.2. Glazed Surface Analysis

The glazed surface analysis is based on the calculation of an overall transmittance value “ U_{cw} ” that considers not only the glass but also the frame presence and the thermal bridge effects that it induces. The calculations are based on the application of the “UNI EN ISO 12631” European standard.

The overall transmittance value is calculated using Equation (38):

$$U_{cw} = \frac{(A_g U_g + A_f U_f + A_m U_m + A_t U_t)}{A_g + A_p + A_f + A_m + A_t} + \frac{L_{fg} \psi_{fg} + L_{mg} \psi_{mg} + L_{tg} \psi_{tg} + L_{mf} \psi_{mf} + L_{tf} \psi_{tf}}{A_g + A_p + A_f + A_m + A_t} \quad (38)$$

where:

- A_g = glass area [m²]
- U_g = glass transmittance [W/m²K]
- A_f = frame area [m²]
- U_f = frame transmittance [W/m²K]
- A_m = mullion area [m²]
- U_m = mullion transmittance [W/m²K]
- A_t = traverses area [m²]
- U_t = traverses transmittance [W/m²K]
- L_{fg} = glass-frame perimeter [m]
- ψ_{fg} = glass-frame linear transmittance [W/mK]
- L_{mg} = glass-mullion perimeter [m]
- ψ_{mg} = glass-mullion linear transmittance [W/mK]
- L_{tg} = glass-traverses perimeter [m]
- ψ_{tg} = glass-traverse linear transmittance [W/mK]
- L_{mf} = frame-mullion perimeter [m]
- ψ_{mf} = frame-mullion linear transmittance [W/mK]
- L_{tf} = frame-traverses perimeter [m]
- ψ_{tf} = frame-traverses linear transmittance [W/mK]

In this way it is possible to obtain an overall transmittance value that can be directly assigned to the software object that models the windows. The U_{cw} values are calculated for different shape of window elements installed at the Smart Energy Building.

Figure 17 shows the different modular elements present in the building envelope.

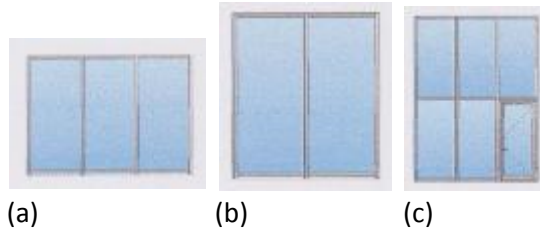


Figure 17: Modular glazed elements - (a) Hall Façade and Gym (b) Offices and Classrooms (c) Hall entrance and glazed doors

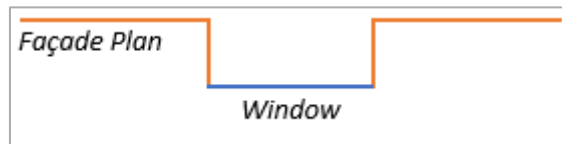


Figure 18: Structural Positioning of Windows

The calculated values of U_{cw} for the different configurations are:

- U_{cw} typology (a) = 1.30 [W/m²K]
- U_{cw} typology (b) = 1.30 [W/m²K]
- U_{cw} typology (c) = 1.40 [W/m²K]

3.2.3.3. Shading Surface Analysis

Given the dynamic aspect of the simulations, it is important to include into the model description also the shading surfaces. Shading surfaces do not actively contribute to the building energy balance, but they have a non-negligible impact in reducing solar energy gains during the day. Shading surfaces do not require a material stratigraphy characterization and they can be used to account for particular architectonic elements (i.e. balconies, marquees, railings) as well as for surrounding buildings.

In the case of SEB, shading surfaces have been used to model the external metallic outdoor blinds structure, the external emergency stairs, the railings on the rooftop and the surrounding buildings. They have been used also to consider that the windows are not aligned with the façade plane, but they are placed approximately 50 [cm] behind it and this leads to a reduction in the solar radiation received by the windows. Figure 18 visually represents the position of windows for the façade.

Modeling recessed windows could have been problematic for the high number of additional surfaces that should have been added, thus it was decided to use shading surfaces (of the same depth) around the windows to account for this peculiar façade design.

The complete model exterior design is shown in Figure 19, with shading surfaces in violet.

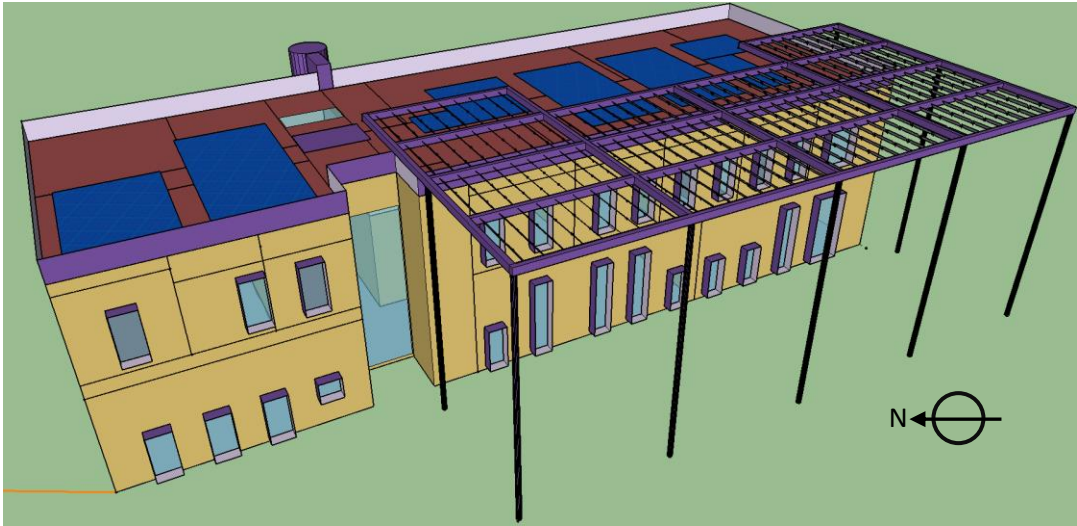


Figure 19: Complete SEB model in Sketchup

3.2.4. Volumetric Analysis and Thermal Zoning

An important part of building modeling is to correctly assign the volume to each part of the building, to estimate the total air volume to be conditioned. Strictly linked to this, there is also the need to properly assign the thermal zones to each geometrical space, to outline the characteristic of the air distribution system. Thermal zone assignment is fundamental to build a solid base upon which develop the rest of the model.

3.2.4.1. Geometrical Volume Analysis and Thermal Zones

This part is devoted to checking if the dimensions of the model match with the real building. Table 9 reports the surface and volume breakdown for all the rooms present in the building.

In the present model, a single thermal zone is assigned for every geometrical space (i.e. rooms) to properly model the control strategy of the HVAC system. It is important to remember that not all the spaces listed in Table 9 are conditioned, some of them (like the elevator pit) are not ventilated or conditioned. This means that the overall conditioned surface and volume are smaller than those reported in Table 9. Moreover, almost all the rooms have a drop ceiling, which creates a space (a plenum) that is not conditioned or ventilated and reduces each room total volume. This has been accounted for and each plenum is defined as a separate thermal zone, not conditioned or ventilated. Considering this aspect, the net total conditioned volume is equal to 4182.5 [m³].

Table 9: Surface and Volume Breakdown for Room Type

| Room type | Area [m ²] | Volume [m ³] |
|------------------------------|------------------------|--------------------------|
| Classroom 1 | 35.2 | 147.2 |
| Classroom 2 | 32.7 | 136.5 |
| Classroom 3 | 40.4 | 169.0 |
| Combustion lab | 140.9 | 993.1 |
| Corridor 1 - Dress Room Side | 8.2 | 34.2 |
| Corridor 2 - Office Side | 22.1 | 92.3 |
| Elevator Pit | 5.3 | 49.0 |
| Gym | 133.2 | 679.5 |
| Hall | 47.5 | 440.5 |
| Men Dress Room | 18.1 | 75.8 |
| Office 1 | 26.4 | 110.5 |
| Office 2 | 24.7 | 103.1 |
| Office 3 | 24.5 | 102.4 |
| Rehe Lab Office | 73.5 | 307.1 |
| Relax Room | 27.1 | 113.2 |
| Restroom 1st floor | 27.9 | 106.1 |
| Restroom Combustion Lab | 12.4 | 63.5 |
| Restroom Solar and Geo lab | 11.5 | 58.5 |
| Solar and Geothermal Lab | 145.2 | 740.3 |
| Technical rooms | 13.9 | 129.1 |
| Woman Dress Room | 16.7 | 69.8 |
| Total | 887.3 | 4720.9 |

3.2.4.2. Thermal Zones Operating Conditions and Internal Gains

It is possible to introduce the operating conditions and internal gains for the thermal zones reported in the previous chapter. The air volumetric flow rates for supply and return air represent also the air changes per hour (the ventilation system is running only with fresh air, there is no recirculation). The internal gains account for the energy contribution given by human occupation of the room, lighting, and plug-loads. Those contributions are important because can modify the energy balance of a thermal zone, reducing the amount of heating energy required and increasing the cooling needs. The evaluation of these parameters is based on measure, experience, common sense and direct observation of the people working and studying inside the SEB.

Table 10, Table 11, Table 12 and Table 13 report details about the air flow rates, the occupancy levels, the lighting and the plug loads, respectively. Moreover, Table 11, Table 12 and Table 13 report the maximum peak value for the considered parameter (i.e. the number of occupants), the related scheduled time interval (i.e. 14-20) and the

percentage of the peak value that is maintained for that specific time schedule. For instance, a peak value of 20 persons from 14 to 20 at 50% means that from 14:00 to 20:00 there are 10 (peak value multiplied for the percentage value) persons inside that thermal zone. For Table 11 the “*Activity Level*” is the amount of thermal power delivered to the zone by each of the occupants. The value is the same for all the thermal zone except for the Gym: the heat delivered in this particular zone will be greater than the heat generated by people at rest in an office.

Table 10: Thermal Zone Volumetric Air Flow Rates and Air Changes per Hour

| Room type | Air Change per hour [-] | Volumetric flow rate [m³/h] | Volumetric flow rate [m³/s] |
|--------------------------|--------------------------------|---|---|
| Classroom 1 | 1.40 | 168.3 | 0.05 |
| Classroom 2 | 1.40 | 208.3 | 0.06 |
| Classroom 3 | 1.40 | 181.5 | 0.05 |
| Combustion Lab | 1.00 | 993.1 | 0.28 |
| Corridor 1 | NA | NA | NA |
| Corridor 2 | NA | NA | NA |
| Elevator Pit | NA | NA | NA |
| Gym | 1.80 | 1079.3 | 0.30 |
| Hall | NA | NA | NA |
| Men Dress Room | 1.70 | 95.5 | 0.03 |
| Office 1 | 1.00 | 97.3 | 0.03 |
| Office 2 | 1.00 | 90.8 | 0.03 |
| Office 3 | 1.00 | 90.1 | 0.03 |
| Rehe Lab Office | 1.00 | 270.4 | 0.08 |
| Relax room | 1.00 | 99.7 | 0.03 |
| Restroom 1st floor | 2.50 | 216.4 | 0.06 |
| Restroom Comb Lab | 2.50 | 96.4 | 0.03 |
| Restroom S&G Lab | 2.50 | 88.9 | 0.02 |
| Solar and Geothermal Lab | 1.00 | 740.3 | 0.21 |
| Technical Rooms | NA | NA | NA |
| Women Dress Room | 1.70 | 88.1 | 0.02 |

Table 11: Thermal Zones Occupancy Breakdown

| GYM | | | | |
|---------------------|----------------|----------|-----|---------------------------|
| | # of Occupants | Schedule | [%] | Activity level [W/person] |
| Gym | 15 | 14-15 | 30 | 432 |
| | | 15-16 | 50 | |
| | | 16-17 | 70 | |
| | | 17-18 | 100 | |
| | | 18-19 | 70 | |
| | | 19-20 | 45 | |
| LABORATORIES | | | | |
| | # of Occupants | Schedule | [%] | Activity level [W/person] |
| Solar and Geo Lab | 1 | 8-13 | 100 | 132 |
| | | 14-17 | 100 | |
| Combustion Lab | 1 | 8-13 | 100 | 132 |
| | | 14-17 | 100 | |
| OFFICES | | | | |
| | # of Occupants | Schedule | [%] | Activity level [W/person] |
| Office 1 | 3 | 8-13 | 100 | 132 |
| | | 14-17 | 100 | |
| Office 2 | 3 | 8-13 | 100 | 132 |
| | | 14-17 | 100 | |
| Office 3 | 3 | 8-13 | 100 | 132 |
| | | 14-17 | 100 | |
| Rehe Lab Office | 3 | 8-13 | 100 | 132 |
| | | 14-17 | 100 | |

CLASSROOMS

| | # of Occupants | Schedule | [%] | Activity level [W/person] |
|-------------|----------------|----------|-----|------------------------------|
| Classroom 1 | 0 | 8-13 | 100 | 132 |
| | | 14-17 | 100 | |
| Classroom 2 | 3 | 8-13 | 100 | 132 |
| | | 14-17 | 100 | |
| Classroom 3 | 3 | 8-13 | 100 | 132 |
| | | 14-17 | 100 | |

RELAX ROOM

| | # of Occupants | Schedule | [%] | Activity level [W/person] |
|------------|----------------|----------|-----|------------------------------|
| Relax Room | 1 | 8-13 | 50 | 132 |
| | | 14-17 | 50 | |

RESTROOMS

| | # of Occupants | Schedule | [%] | Activity level [W/person] |
|--------------------|----------------|----------|-----|------------------------------|
| Restroom S&G Lab | 2 | 9-18 | 10 | 132 |
| Restroom Comb Lab | 2 | 9-18 | 10 | 132 |
| Restroom 1st floor | 2 | 9-18 | 10 | 132 |

DRESS ROOMS

| | # of Occupants | Schedule | [%] | Activity level [W/person] |
|------------------|----------------|----------|-----|------------------------------|
| Women Dress Room | 2 | 9-18 | 10 | 432 |
| Men Dress Room | 2 | 9-18 | 10 | 432 |

CORRIDORS

| | # of Occupants | Schedule | [%] | Activity level [W/person] |
|------------|----------------|----------|-----|------------------------------|
| Corridor 1 | 2 | 9-18 | 10 | 132 |
| Corridor 2 | 2 | 9-18 | 10 | 132 |
| Hall | 2 | 9-18 | 10 | 132 |

| ELEVATOR PIT-TECHNICAL ROOMS | | | | |
|-------------------------------------|----------------|----------|-----|------------------------------|
| | # of Occupants | Schedule | [%] | Activity level [W/person] |
| Technical Rooms | NA | NA | NA | NA |
| Elevator Pit | NA | NA | NA | NA |

Table 12: Thermal Zones Illumination Breakdown

| GYM | | | | |
|---------------------|----------------------------|---------------|-----|--|
| | Lights [W/m ²] | Schedule | [%] | |
| Gym | 6.50 | 9-18 | 100 | |
| LABORATORIES | | | | |
| | Lights [W/m ²] | Schedule | [%] | |
| Solar and Geo Lab | 5.00 | 8-13 14-17 | 100 | |
| Combustion Lab | 5.00 | 8-13 14-17 | 100 | |
| OFFICES | | | | |
| | Lights [W/m ²] | Schedule | [%] | |
| Office 1 | 6.50 | 8-13 14-17 | 100 | |
| Office 2 | 6.50 | 8-13 14-17 | 100 | |
| Office 3 | 6.50 | 8-13 14-17 | 100 | |
| Rehe Lab Office | 6.50 | 8-13 14-17 | 100 | |
| CLASSROOMS | | | | |
| | Lights [W/m ²] | Schedule | [%] | |
| Classroom 1 | 0.00 | 8-13 14-17 | 100 | |
| Classroom 2 | 6.50 | 8-13 14-17 | 100 | |
| Classroom 3 | 6.50 | 8-13 14-17 | 100 | |

Considering the Dress Rooms, the activity level is increased to 432 [W/person] in order to account for the vapour production coming from the showers.

| RELAX ROOM | | | |
|-------------------------------------|----------------------------|---------------|-----|
| | Lights [W/m ²] | Schedule | [%] |
| Relax Room | 6.50 | 8-13 14-17 | 50 |
| RESTROOMS | | | |
| | Lights [W/m ²] | Schedule | [%] |
| Restroom S&G Lab | 1.80 | 9-18 | 10 |
| Restroom Comb Lab | 1.80 | 9-18 | 10 |
| Restroom 1st floor | 1.80 | 9-18 | 10 |
| DRESS ROOMS | | | |
| | Lights [W/m ²] | Schedule | [%] |
| Women Dress Room | 1.80 | 9-18 | 10 |
| Men Dress Room | 1.80 | 9-18 | 10 |
| CORRIDORS | | | |
| | Lights [W/m ²] | Schedule | [%] |
| Corridor 1 | 5.00 | 9-18 | 70 |
| Corridor 2 | 5.00 | 9-18 | 70 |
| Hall | 5.00 | 9-18 | 70 |
| ELEVATOR PIT-TECHNICAL ROOMS | | | |
| | Lights [W/m ²] | Schedule | [%] |
| Technical Rooms | NA | NA | NA |
| Elevator Pit | NA | NA | NA |

Table 13: Thermal Zones Plug Loads Breakdown

| GYM | | | |
|---------------------|--------------------------|----------|-----|
| | Plug [W/m ²] | Schedule | [%] |
| Gym | 3.75 | 14-20 | 100 |
| LABORATORIES | | | |
| | Plug [W/m ²] | Schedule | [%] |
| Solar and Geo Lab | 10.00 | 9-18 | 100 |
| Combustion Lab | 10.00 | 9-18 | 100 |

| OFFICES | | | |
|-----------------|--------------------------|---------------|-----|
| | Plug [W/m ²] | Schedule | [%] |
| Office 1 | 20.00 | 8-13 14-17 | 100 |
| Office 2 | 20.00 | 8-13 14-17 | 100 |
| Office 3 | 20.00 | 8-13 14-17 | 100 |
| Rehe Lab Office | 20.00 | 8-13 14-17 | 100 |

| CLASSROOMS | | | |
|-------------------|--------------------------|---------------|-----|
| | Plug [W/m ²] | Schedule | [%] |
| Classroom 1 | 0.00 | 8-13 14-17 | 100 |
| Classroom 2 | 0.00 | 8-13 14-17 | 100 |
| Classroom 3 | 0.00 | 8-13 14-17 | 100 |

| RELAX ROOM | | | |
|-------------------|--------------------------|----------|-----|
| | Plug [W/m ²] | Schedule | [%] |
| Relax Room | NA | NA | NA |

| RESTROOMS | | | |
|--------------------|--------------------------|----------|-----|
| | Plug [W/m ²] | Schedule | [%] |
| Restroom S&G Lab | NA | NA | NA |
| Restroom Comb Lab | NA | NA | NA |
| Restroom 1st floor | NA | NA | NA |

| DRESS ROOMS | | | |
|--------------------|--------------------------|----------|-----|
| | Plug [W/m ²] | Schedule | [%] |
| Women Dress Room | NA | NA | NA |
| Men Dress Room | NA | NA | NA |

| CORRIDORS | | | |
|------------------|--------------------------|----------|-----|
| | Plug [W/m ²] | Schedule | [%] |
| Corridor 1 | NA | NA | NA |
| Corridor 2 | NA | NA | NA |
| Hall | NA | NA | NA |

| ELEVATOR PIT-TECHNICAL ROOMS | | | |
|-------------------------------------|--------------------------|----------|-----|
| | Plug [W/m ²] | Schedule | [%] |
| Technical Rooms | NA | NA | NA |
| Elevator Pit | NA | NA | NA |

It is important to point out that for some table entries there is the value NA, while others have a peak value of zero. This means that in both cases the value of the specific internal gain is zero, but with a difference. The value is “NA” means that the specific load will probably remain zero even in the future. In the other case, the value is set to zero (based on the actual situation present nowadays) but it might change in the future (i.e. Classroom have no plug loads connected, but this might change if some devices will be installed there). This choice was made to give more flexibility to the model, because it becomes easier to control those gains by simply inputting the peak value, given that the schedules are already present in the model.

3.2.5. Ideal Loads System Simulation Results

In this paragraph, the ideal energy needs for the SEB are presented on a monthly averaged basis, aggregated for all the thermal zones (Table 14). Table 14 reports also the averaged outside air temperature for each month.

Moreover, simulation results are shown for a representative week during winter and one during summer for two selected thermal zones.

Analysing Table 14, one can immediately notice that also for summer months there is a request for heating. This can be ascribed to the reheating process needed after the sensible and latent cooling processes during summer air conditioning: removing excess humidity from air imposes lowering air temperature to condensate the moisture. Thus, it is necessary to heat it again to an acceptable supply temperature (for instance 18 [°C]), to preserve the comfort level inside the rooms. On the other hand, during winter months, there is a need for cooling power. This can be related to the dehumidification of air: during winter the external air has high relative humidity, so part of this moisture needs to be condensed lowering the temperature of inlet air.

Table 14: Monthly Averaged Energy Needs (for all Thermal Zones)

| | Cooling [kWh] | Heating [kWh] | Average Outdoor Air Temperature [°C] |
|-----------|---------------|---------------|--------------------------------------|
| January | 38 | 18606 | 9.5 |
| February | 35 | 16039 | 9.3 |
| March | 32 | 11531 | 12.1 |
| April | 29 | 5492 | 13.2 |
| May | 3216 | 543 | 17.3 |
| June | 8059 | 235 | 20.4 |
| July | 14033 | 244 | 24.2 |
| August | 8990 | 617 | 24.7 |
| September | 7157 | 235 | 21.9 |
| October | 1950 | 599 | 17.8 |
| November | 26 | 11657 | 12.5 |
| December | 38 | 16647 | 10.1 |
| Total | 43606 | 82445 | |

Focusing on August, the cooling request is approximately half of July's one. This is explainable considering the vacation period in the scheduling process: for the weeks going from 7th to 23rd August the building is considered not occupied, thus the HVAC system is effectively shut down.

For clarity purposes, Figure 20 reports the information contained in Table 14 in a bar chart. For better understanding whether the Ideal Loads system is currently controlling the indoor air temperature and relative humidity of the building, it can be useful to plot the hourly trend for different quantities:

- Outdoor Air Temperature [°C];
- Indoor Air Temperature [°C];
- Air Temperature Set Points [°C];
- Indoor Relative Humidity [-].

For the sake of brevity, the results are proposed only for two thermal zones (Office 3 and Gym) and for two weeks (9th to 15th January, and 1st to 7th July). The two thermal zones have been selected to be representative of the different operating conditions. The office is characterized by a low occupancy level (3 persons max) with low activity levels but has high internal gains given by plug loads, lights and sun exposure.

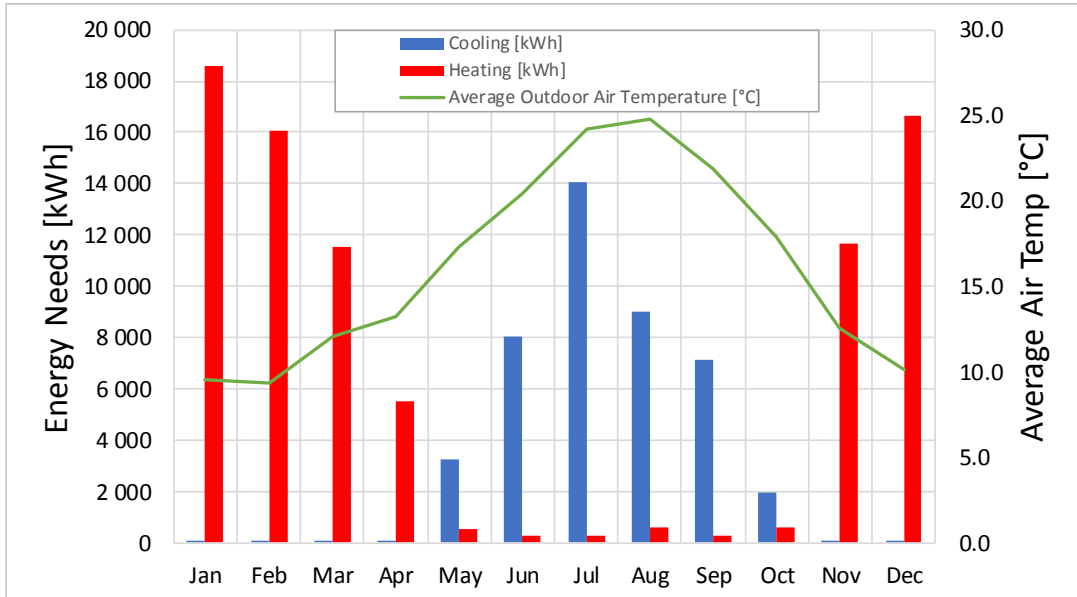


Figure 20: Monthly aggregated energy needs and average outdoor air temperature



Figure 21: Selected Thermal Zone

On the contrary, the gym has much higher occupation levels (20 persons max with intense activity levels) but lower internal gains due to plug loads ($3.75 \text{ [W/m}^2\text{]}$). The sun exposure is similar, but the gym has only one side exposed to the sun, while the other 3 are not receiving direct solar radiation. Figure 21 illustrates where are located the selected thermal zones.

3.2.5.1. Ideal Loads System Simulation Results - Winter Season

Figure 22 shows the hourly trend for the selected winter period (9th to 15th January) for indoor and outdoor air conditions.

To check if the Ideal Loads system is actively controlling the comfort levels inside the thermal zone is necessary to analyze the relative humidity and the indoor air temperature trends. Those quantities have specific upper and lower limits, which should be never

overstepped when the system is working. Figure 22 clearly shows that, for the Office 3, the relative humidity only gets higher than approximately 65% during nighttime periods, while it is stable at some 50% (which represents the desired relative humidity setpoint) when the system is conditioning the space. At the same time, the indoor air temperature is always equal to or greater than the heating temperature setpoint (22 [°C]). When the ventilation is shut down (as it is shown in Figure 24), the relative humidity shows a particular rising trend, as reported by Figure 22. When the room air temperature decreases (i.e. when the building is not occupied and the setpoint is set at 17 [°C]), then the relative humidity inversely rises, and rapidly decreases as soon as the temperature setpoint is incremented to the daytime value, which is 22 [°C]. However, the Ideal Loads is not providing any Cooling Load, because the relative humidity does not overstep the night-time setpoint, fixed at 70 % (ref. Figure 23)

The same results for the Gym thermal zone are presented in Figure 25: the analysis shows that the Ideal Loads model is, once again, able to control the indoor thermal and humidity conditions, when the space is occupied. Considering the temperature, the setpoint temperature is always maintained, with indoor air temperature never falling below the minimum required. In Figure 25, one can notice that, in this case, the humidity is not rising when the ventilation system is shut down (ref. Figure 26), instead it decreases until the night-time setpoint is reached (30 %). This can be explained analysing Figure 26: the Ideal Total Cooling Load is present also whether the ventilation is shut down. If this happens, the air contained in the thermal zone (which starts to be recirculated by the Ideal Load System) still possesses part of the latent heat gained during the occupied time. This latent heat is removed by the Ideal Loads (condensing the air moisture), explaining why the Gym thermal zone requires that amount of cooling power.

The plateau in the data series in both Figure 22 and Figure 25 is due to the weekend days. The system is only conditioning the air temperature with no regard for the humidity. In fact, the temperature is not lower than the setpoint (17 [°C]), while the humidity is fluctuating around lower values (approximately 25 - 30 %) This operating mode is useful to never let the whole building temperature to get too low, avoiding huge thermal transitory period when the system is turned on again (i.e. Monday morning). In this way, the comfort inside the building is reached more easily and it avoids also to stress the conditioning system with OFF-ON transitory phases.

The same analysis is carried out with respect to Heating and Cooling loads as well as ventilation requirements. Figure 22 Figure 26 and Figure 27 shows the trends of these quantities for the same period (9th to 15th January). Overall the situation is very similar for both the spaces, with the main difference being the amount of cooling energy required by the gym. Similarly to what explained above, this is linked to the latent heat produced during the activity of people: for the office, this quantity is very low, while for the gym this contribution becomes important. During the weekends, only a small portion of heating energy is required, for energy saving purposes, like explained when discussing about the

temperature trends. The ventilation requirements are always fulfilled, and during weekends the system is active to maintain the lowered temperature setpoint.

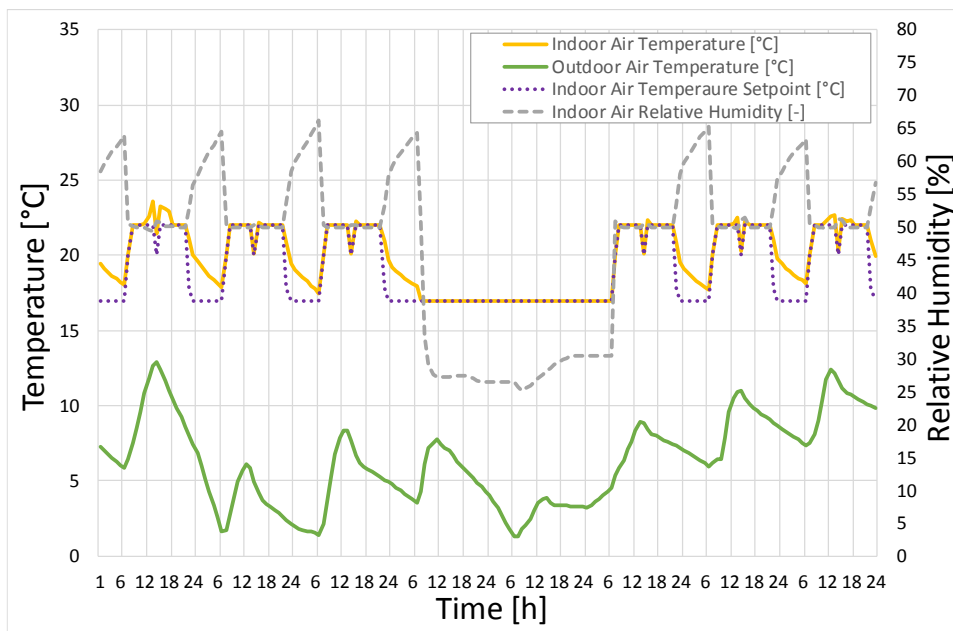


Figure 22: Office 3 Temperatures (Outdoor and Indoor) and Relative Humidity - January weekly trends

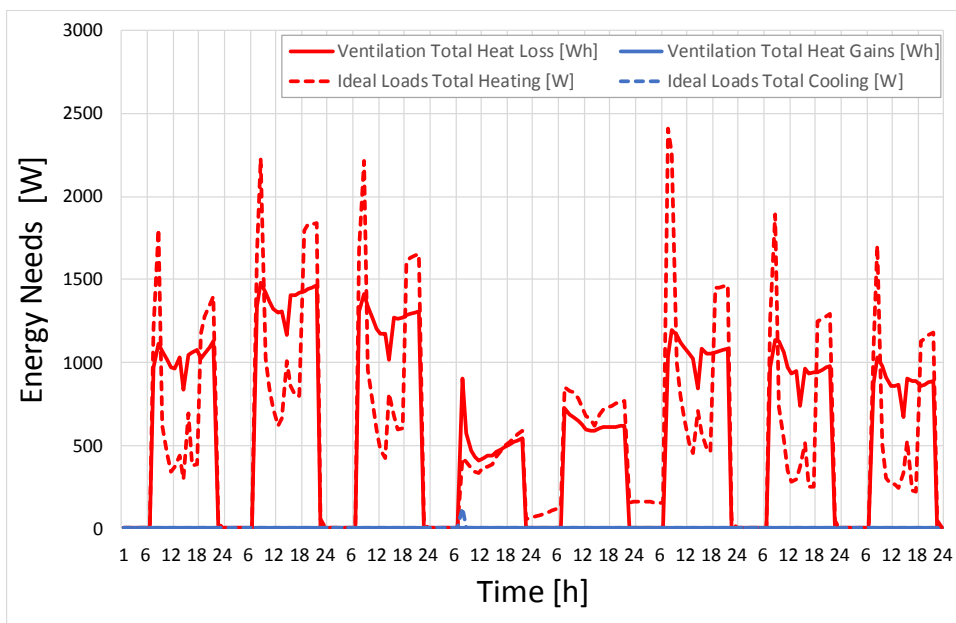


Figure 23: Office 3 Ventilation Heat Loss / Gains and Ideal Loads Heating and Cooling Loads - January weekly trends

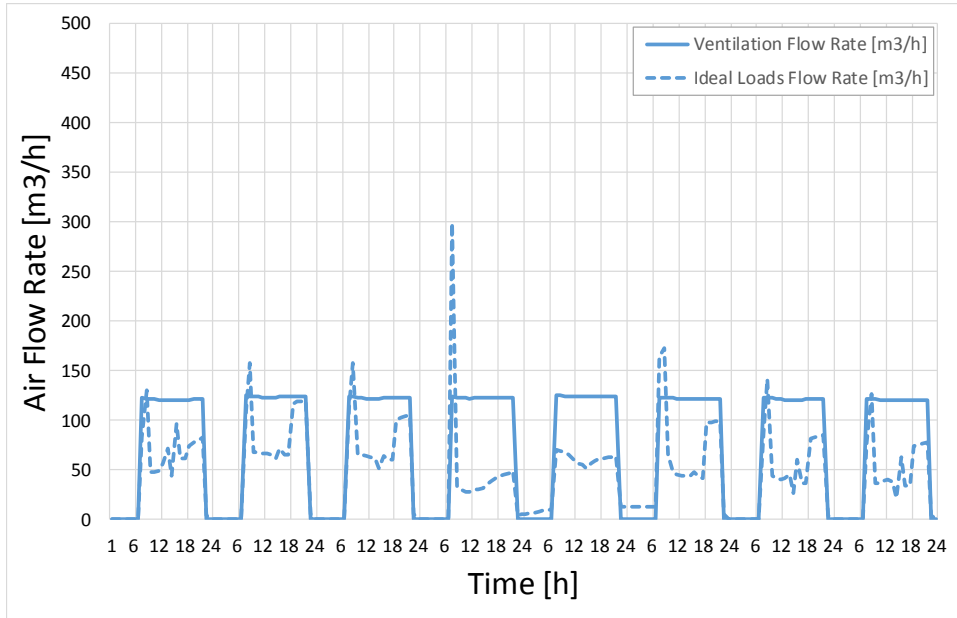


Figure 24: Office 3 Ventilation and Ideal Loads Air Volumetric Flow Rates - January weekly trends

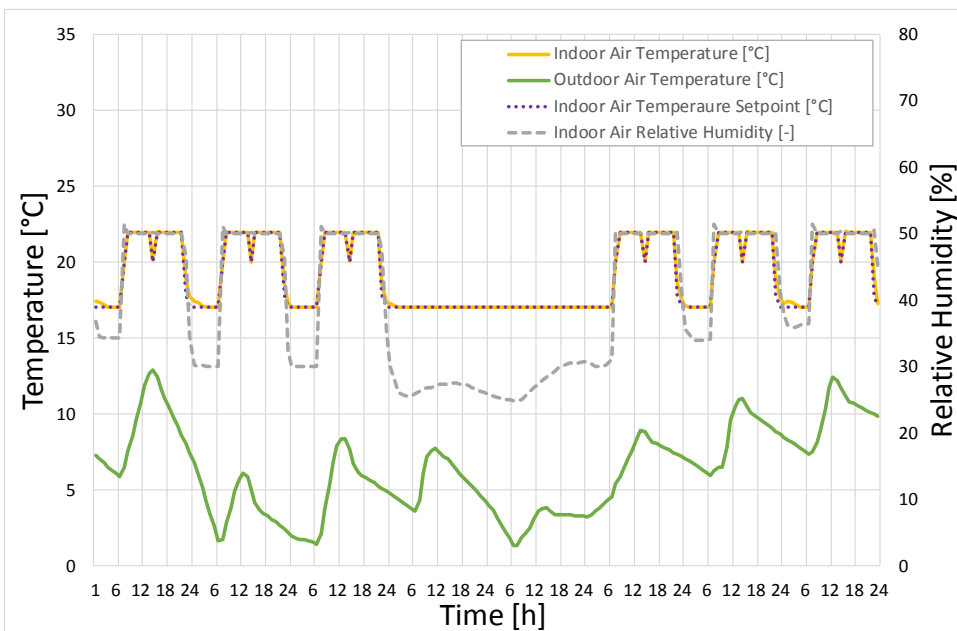


Figure 25: Gym Temperatures (Outdoor and Indoor) and Relative Humidity - January weekly trends

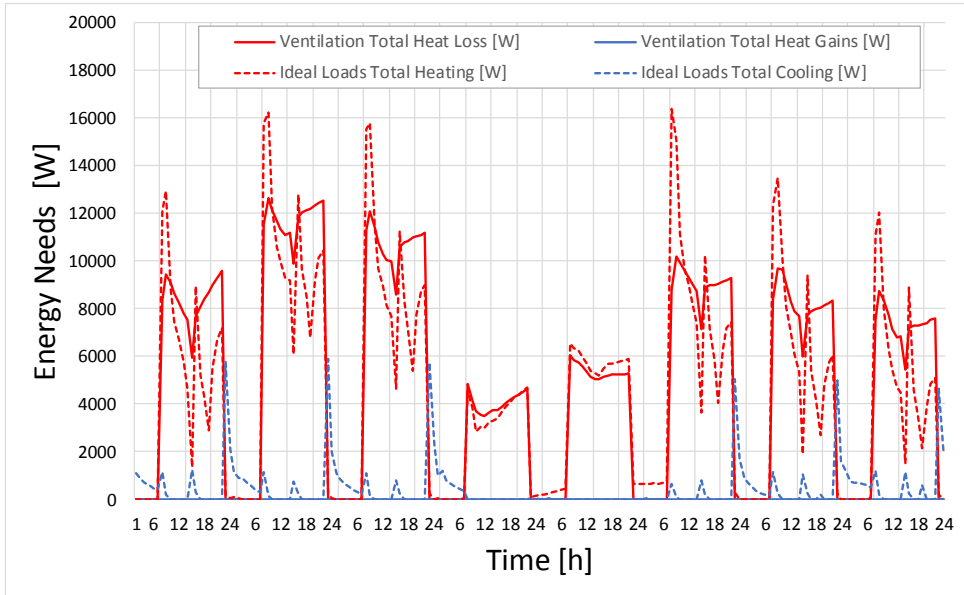


Figure 26: Gym Ventilation Heat Loss / Gains and Ideal Loads Heating and Cooling Loads - January weekly trends

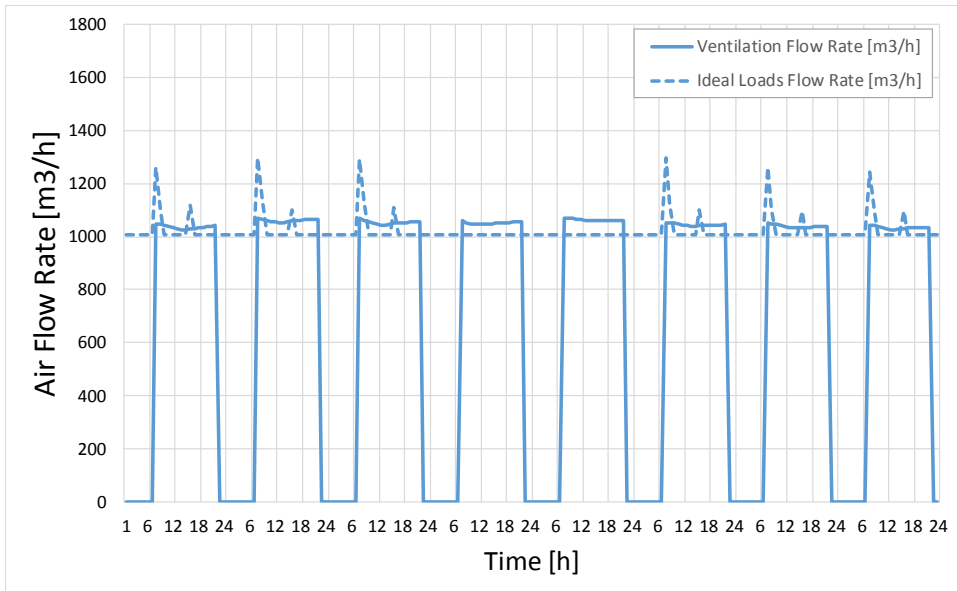


Figure 27: Gym Ventilation and Ideal Loads Air Volumetric Flow Rates - January weekly trends

3.2.5.2. Ideal Loads System Simulation Results - Summer Season

Figure 28 shows the weekly trend for the selected summer period (1st to 7th July) for indoor and outdoor air conditions, when the Office 3 thermal zone is considered.

The situation is very similar to the cases analyzed before; the Ideal Load model can maintain the desired comfort conditions inside the considered room.

The setpoint temperature for cooling changes during the simulation: when there are no occupants inside the room, (i.e. during the lunch break from 13.00 to 14.00) the setpoint is risen by 2°C (from 24 [°C] to 26 [°C]). However, the system is not completely shut down to avoid temperature strong transitory in a short period of time and this is useful to preserve the system from suddenly change its working conditions. Moreover, during the transition phase, the occupants can experience lower comfort levels, due to the temperature and humidity not in the optimal range. On the other hand, during weekends or vacation periods, the system is shut down to save energy and it is switched on again before people occupy the room (usually this is done around 6.00 am). In Figure 28 the first two days of simulation (1st and 2nd July) are weekend days. The temperature set point is changed a few hours before the office worktime.

Figure 31 shows the same analysis for the Gym Thermal Zone, in the same period (1st to 7th July).

Comparing the relative humidity in the two cases, the situation is very similar. When the building is occupied: the relative humidity is maintained equal to the setpoint (50% for both thermal zones). On the other hand, since the first two days of simulation are Saturday and Sunday, the system is off (for the reasons explained above) thus the indoor air temperature is greater than the comfort levels (24 °C). In particular, for the office, it shows a peak around 29°C while for the gym the peak is around 27°C. This behaviour can be explained by the fact that the office is sun-exposed while the gym has the walls that remain shaded for most of the day; therefore, the solar gains from the glazed surfaces are higher in the office.

Analysing the simulation results obtained for the cooling and heating loads, the situation is similar for both the Office 3 and the Gym, and the results are illustrated in Figure 29 and Figure 32, respectively. However, the two thermal zones exhibit different heating loads requests. The office requires heating especially during the weekends, with peaks during the workdays while the gym requires a more constant value. This is related to the humidity control: to condensate moisture the air has to be cooled down to the dew point temperature, which can be significantly lower than the required inlet air temperature. The inlet air must be reheated to acceptable values, to avoid very cold air streams at the air diffusers. that induce a negative effect on the thermal comfort conditions perceived by the occupants. The Cooling Load for the Gym is higher than the Office: this is linked to the considerable difference between the latent heat gains.

The ventilation requirements are fulfilled for all the considered simulation period, for both the thermal zone analysed (see Figure 30 and Figure 33).

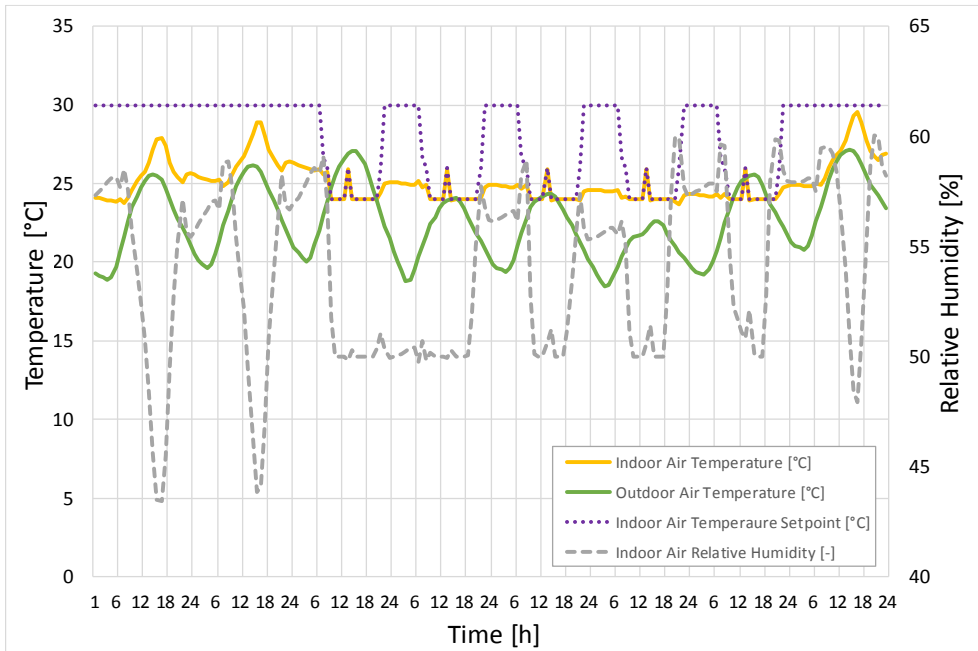


Figure 28: Office 3 Temperatures (Outdoor and Indoor) and Relative Humidity - July weekly trends

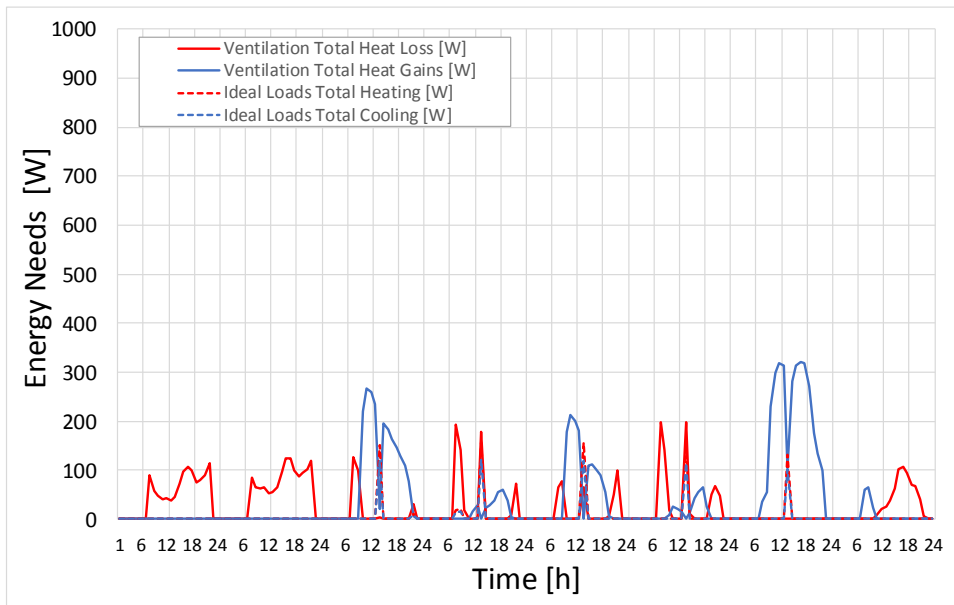


Figure 29: Office 3 Ventilation Heat Loss / Gains and Ideal Loads Heating and Cooling Loads - July weekly trends

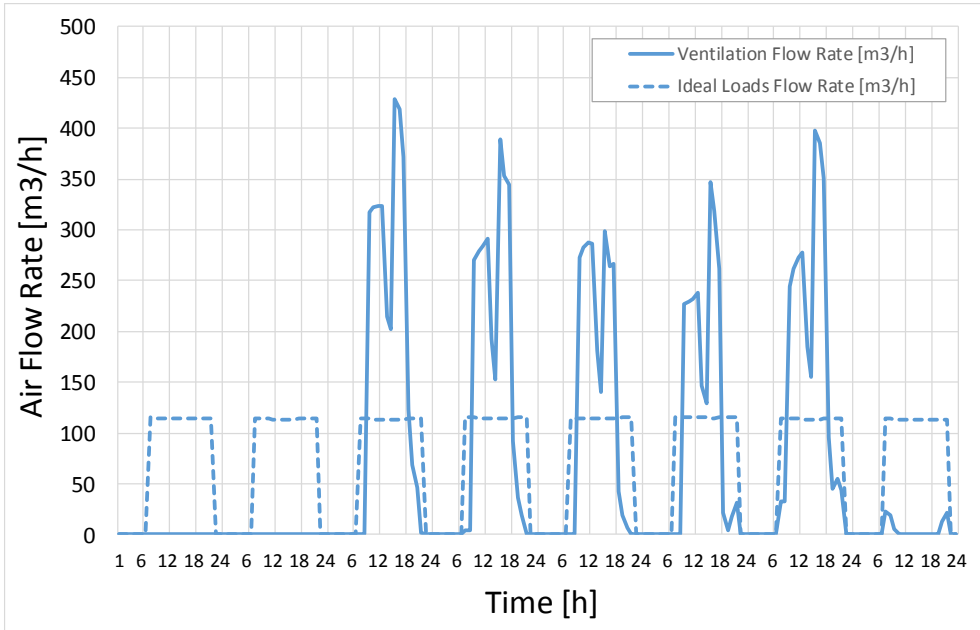


Figure 30: Office 3 Ventilation and Ideal Loads Air Volumetric Flow Rates - July weekly trends

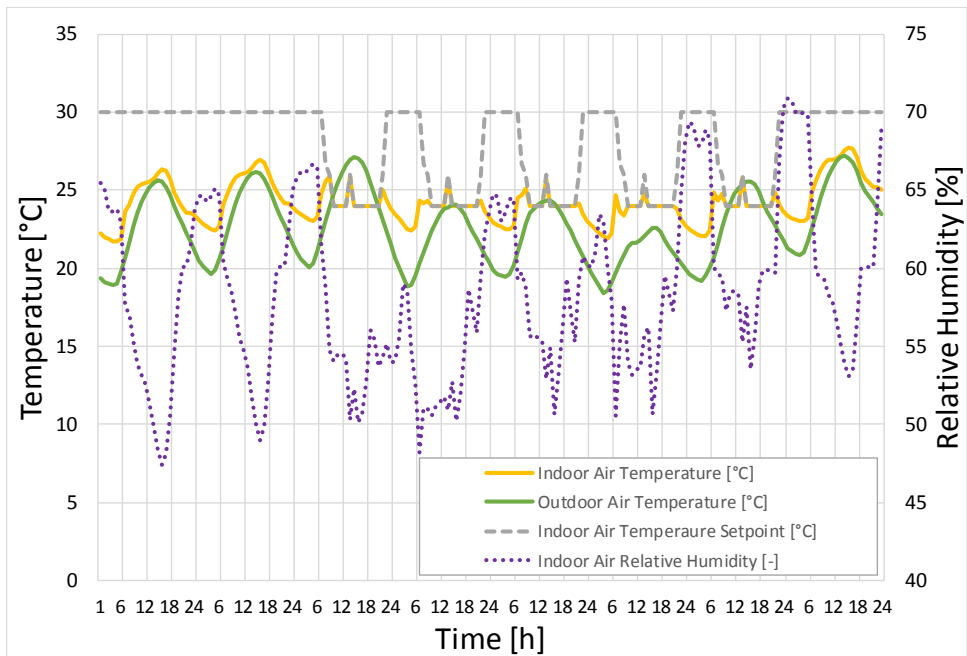


Figure 31: Gym Temperatures (Outdoor and Indoor) and Relative Humidity - July weekly trends

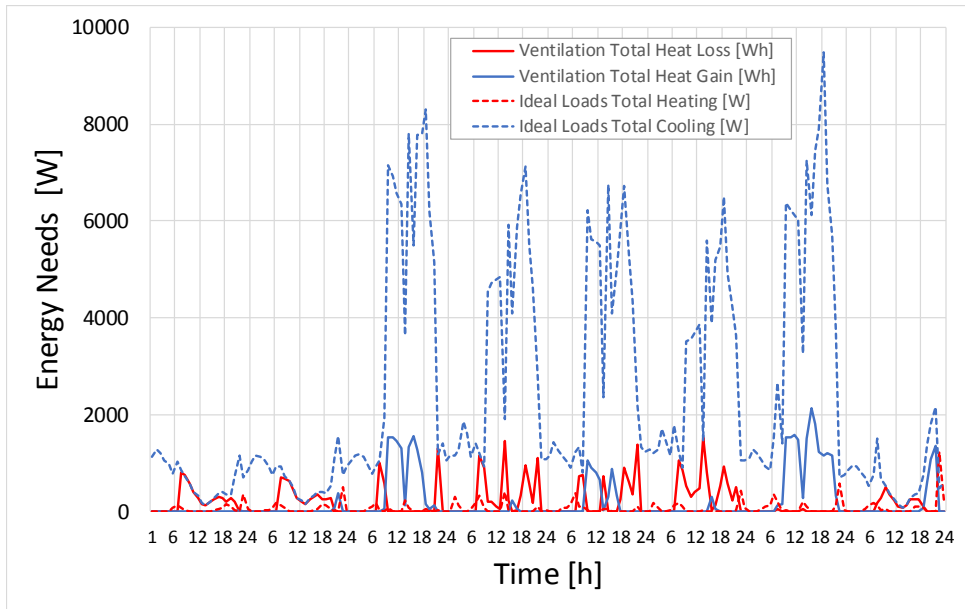


Figure 32: Gym Ventilation Heat Loss / Gains and Ideal Loads Heating and Cooling Loads - July weekly trends

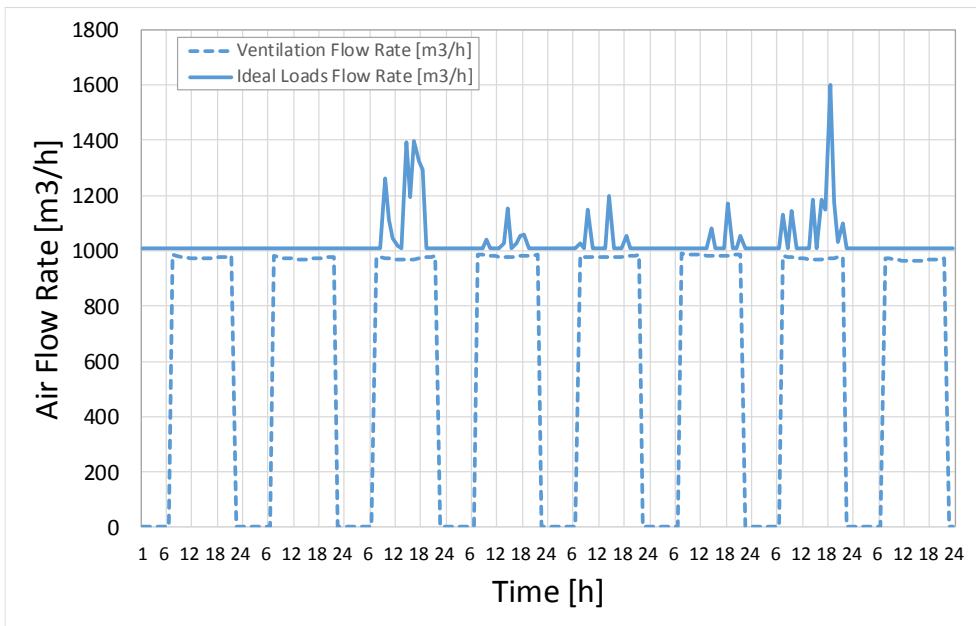


Figure 33: Gym Ventilation and Ideal Loads Air Volumetric Flow Rates - July weekly trends

3.2.6. Smart Energy Building Plants: Description

This paragraph will briefly illustrate the main features of the energy system of the SEB building. Firstly, the ground coupled heat pump is presented together with brief notions about the theoretical background for geothermal borefields. Then it is presented the air-to-air heat pump installed at the SEB. Lastly, the distribution networks for water and air inside the SEB building are described. For the air distribution system, the volumetric flow rates for every zone have been already reported in Table 10, while for the water distribution more information is reported in this paragraph. The water distribution is only referring to the circuit connecting the GHCP to the fancoils and radiators terminals.

3.2.7. Ground Coupled Heat Pump

The water to water heat pump installed at the SEB is a Ground Coupled Heat Pump (GCHP). In general, this kind of heat pump is a system used to heat and/or cool a building transferring heat from/to the ground, respectively during winter or summer months. The ground has a nearly constant temperature during the year, almost equal to the average external air temperature of the site. Thus, the seasonal COP of the system results bigger than for a traditional air-to-air heat pump.

A GCHP is coupled to the ground through a system of heat exchangers, horizontally or vertically buried into the soil. The more common type of heat exchanger is the vertical one, called also Borehole Heat Exchangers (BHEs). The GCHP plant installed in the SEB is characterized by a close-loop vertical configuration. Eight vertical borehole heat exchangers (BHEs) are buried about 120 m deep in the soil.

In modeling GCHP with a dynamic simulation software, the knowledge of the thermal response of the ground to the building loads is requested to predict the fluid temperature from the BHE field, $T_{Fluid,ave}$. In fact, this value represents the source side temperature for the GCHP and influences the COP of the plant.

The ground is considered as a semi-infinite medium, with uniform initial temperature called undisturbed temperature. When the heat extraction/injection begins, the ground temperature is modified around each BHE of the field.

The behavior of the BHEs field into the ground can be modeled with the well-known approach of the two thermal resistances. The first one is time-dependent and represents the response of the ground, linking the average BHE temperature, $T_{ave}(r_b)$ to the undisturbed ground one. The second resistance, constant in time, is the BHE internal resistance R_b , and links the average BHE temperature to the average fluid temperature.

It is possible to forecast the average temperature at the BHEs periphery by applying Eskilson's g -function theory [24]. The g -function (or transfer function) represents the dimensionless temperature response of the ground to the extraction/rejection heat load and depends on the borehole field configuration, the ground properties and the

heating/cooling needs of the buildings. Table 15 summarizes the parameters related to the BHE field in the Savona Campus.

Equation (39) is the general formulation for the ground transfer function.

$$T_{ave}(r_b) - T_{gr,\infty} = \frac{1}{2\pi} \frac{\dot{Q}'_{ave}}{k_{gr}} g \left(\ln(9 \cdot Fo_H), \frac{r_b}{H}, \frac{B}{H, \text{borefieldgeometry}} \right) \quad (39)$$

where:

- $T_{ave}(r_b)$ is the average borehole temperature [K];
- $T_{gr,\infty}$ is the ground undisturbed temperature [K];
- \dot{Q}'_{ave} is the average heat flux per unit length [W/m];
- k_{gr} is the ground thermal conductivity [W/mK];
- Fo_H is the Fourier Number referred to the borehole length [-];
- r_b is the borehole radius [m];
- H is the borehole length [m];
- B is the distance between the boreholes, in case more than one is considered [m].

Successively, knowing the time-dependent BHE average temperature, it is possible to deduce the average fluid temperature (source side) $T_{s,ave}$ by means of the borehole resistance R_b , with Equation (40).

$$T_{s,ave} = T_{ave}(r_b) + R_b \cdot \dot{Q}'_{ave} \quad (40)$$

For the BHE field of the SEB building in the Savona Campus, the proper g -function has been derived from the database of the commercial software EED [25]. The time-dependent g -function is then introduced in the Energy Plus model for selected values of the Fourier number, according to a dimensionless formulation.

The ground thermo-physical properties and the borehole resistance R_b have been experimentally determined with a Thermal Response Test (TRT), carried out in situ with a dedicated TRT machine [11] (Figure 34).

Table 15: Geometrical Parameters for SEB bore field

| BHE field geometrical parameters | | | | | | |
|----------------------------------|-----------|-----------|---------|---------|----------------|------------------|
| Shape | r_b [m] | r_p [m] | H [m] | B [m] | R_b [m K /W] | k_{gr} [W/m K] |
| Single U | 0.45 | 0.02 | 125-150 | 8 | 0.13 | 6.2 |

With r_p being the pipe radius and R_b being the borehole thermal resistance.



(a)

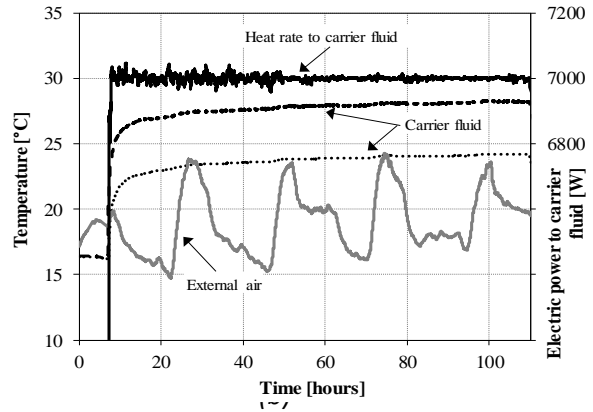


Figure 34: (a) TRT machine developed at the University of Genova, (b) Temperature profiles during the first 100 hours of the pulsated TRT experiment

Tables 16: Manufacturer Data for reversible heat pump (cooling mode).

| Source side outlet water temperature, $T_{S,out}$ [°C] | Load side outlet water temperature, $T_{L,out}$ [°C] | | | | | | | | | | | | | | | | | |
|--|--|-------|------|------|------|------|------|------|------|------|-------|------|------|-------|------|------|------|------|
| | 5 | | | 7 | | | 10 | | | 12 | | | 15 | | | 18 | | |
| | kWt | kWe | COP | kWt | kWe | COP | kWt | kWe | COP | kWt | kWe | COP | kWt | kWe | COP | kWt | kWe | COP |
| 25 | 41.7 | 7.67 | 5.43 | 44.3 | 7.75 | 5.72 | 48.1 | 7.89 | 6.10 | 50.0 | 8.00 | 6.25 | 54.6 | 8.2 | 6.66 | 58.9 | 8.51 | 6.92 |
| 30 | 39.9 | 8.67 | 4.60 | 42.5 | 8.76 | 4.86 | 46.1 | 8.89 | 5.19 | 48.1 | 9.00 | 5.34 | 52.4 | 9.18 | 5.71 | 56.6 | 9.46 | 5.98 |
| 35 | 38.1 | 9.67 | 3.93 | 40.7 | 9.76 | 4.17 | 44.1 | 9.89 | 4.46 | 46.2 | 10.00 | 4.62 | 50.1 | 10.16 | 4.93 | 54.3 | 10.4 | 5.22 |
| 40 | 35.4 | 10.92 | 3.24 | 38.3 | 10.9 | 3.50 | 41.6 | 11.1 | 3.75 | 43.5 | 11.1 | 3.92 | 47.3 | 11.3 | 4.19 | 51.3 | 11.6 | 4.42 |
| 45 | 32.9 | 12.3 | 2.68 | 35.3 | 12.4 | 2.86 | 38.2 | 12.5 | 3.06 | 40.2 | 12.6 | 3.19 | 43.6 | 12.7 | 3.43 | 47.2 | 13 | 3.63 |
| 50 | 29.8 | 13.8 | 2.16 | 32 | 13.9 | 2.30 | 34.8 | 14 | 2.49 | 36.5 | 14.1 | 2.59 | 39.9 | 14.3 | 2.79 | 43.1 | 14.5 | 2.97 |

Table 17: Manufacturer Data for reversible heat pump (heating mode).

| Source side outlet water temperature, $T_{S,out}$ [°C] | Load side outlet water temperature, $T_{L,out}$ [°C] | | | | | | | | | | | |
|--|--|------|------|------|------|------|------|------|------|-------|-------|------|
| | 30 | | | 35 | | | 45 | | | 50 | | |
| | kWt | kWe | COP | kWt | kWe | COP | kWt | kWe | COP | kWt | kWe | COP |
| 0 | 41.8 | 7.37 | 5.67 | 41.3 | 8.35 | 4.95 | 40.5 | 10.7 | 3.79 | 39.4 | 12.2 | 3.23 |
| 1 | 43.1 | 7.39 | 5.83 | 42.4 | 8.37 | 5.07 | 41.6 | 10.7 | 3.89 | 40.4 | 12.2 | 3.32 |
| 3 | 45.5 | 7.44 | 6.12 | 44.9 | 8.43 | 5.33 | 43.8 | 10.7 | 4.10 | 42.6 | 12.2 | 3.50 |
| 5 | 46.5 | 7.47 | 6.22 | 46.3 | 8.48 | 5.45 | 45.4 | 10.7 | 4.24 | 43.8 | 12.2 | 3.59 |
| 7 | 49.4 | 7.53 | 6.55 | 49.0 | 8.54 | 5.73 | 48.0 | 10.7 | 4.48 | 46.25 | 12.2 | 3.79 |
| 10 | 53.7 | 7.62 | 7.04 | 53.2 | 8.65 | 6.15 | 51.8 | 10.8 | 4.79 | 49.85 | 12.25 | 4.07 |
| 12 | 56.7 | 7.70 | 7.36 | 56.2 | 8.73 | 6.44 | 54.7 | 10.9 | 5.02 | 52.55 | 12.35 | 4.26 |
| 15 | 61.7 | 7.83 | 7.88 | 60.9 | 8.86 | 6.87 | 59.2 | 11.0 | 5.38 | 56.75 | 12.4 | 4.58 |
| 17 | 65.2 | 7.92 | 8.24 | 64.4 | 8.96 | 7.19 | 62.5 | 11.0 | 5.68 | 59.85 | 12.45 | 4.81 |

For the Smart Energy Building, the geothermal heat pump in operation is a Clivet brand, model WSHN-XEE2 MF 14.2, working with brine (geothermal side) and water. The manufacturer catalogue provides the heat pump performances as a function of source/load fluid temperatures.

Tables 16 represents the data from the catalogue for the size 14.2, for cooling mode. The performance related to the heating mode as a function of temperatures is

provided by the Manufacturer in two different Tables, depending on the range of the source side water temperature. For this test case, it is interesting to consider a wide range of working conditions for the source side temperature. In fact, for a GCHP with an expected long life of operation time, the temperature of the ground, starting from the undisturbed value, can change considerably in time [26] and consequently also the temperature of the fluid circulating in the BHE field changes.

Unfortunately, the two manufacturer Tables for heating mode differ for the selected values of the load side temperatures and thus it is necessary to apply a proper interpolation. This is a typical problem in manufacturer data, and it cannot be managed in Energy Plus differently. The obtained combined dataset for heating mode is presented in Table 17: the grey cells represent the data achieved by interpolation.

3.2.8. Air-to-air Heat Pump

For the Smart Energy Building, the selected air-to-air heat pump associated with the Air Handler Unit (AHU) is the Clivet model Zephir CPAN-XHE3 Size 3, with a standard air flow of 4600 [m³/h]. This volumetric flow rate fulfills the ventilation requested by the Italian standards for the SEB building in terms of its volume and expected occupancy levels.

This air unit is very peculiar, especially if compared with the options conceived and available in Energy Plus. This system is a primary-air plant with a thermodynamic recovery of the energy contained in the return air. The primary air (*OA*) comes entirely from the outdoor (load side). The Return air (*RA*), coming from the building inner rooms, before being released to the atmosphere, exchange heat with the condenser in cooling mode and with the evaporator in heating mode (source side). Return-air represents a favorable thermal source stable in time, offering lower temperature at the condenser in cooling mode and higher temperature at the evaporator in heating mode. As a consequence, the energy required by the compressors is reduced up to 50% [27].

The manufacturer catalogue provides the reversible heat pump performances as a function of external air temperature T_{OA} (dry bulb/wet bulb) and supply air temperature T_{SA} . The manufacturer catalogue reports two different types of performance coefficients, the thermodynamic efficiencies (EER_{th}/COP_{th}) and the overall efficiencies (EER/COP) that consider also the power of the auxiliary systems.

In cooling mode, the selected supply humidity ratio is equal to 11 [g_{vap}/kg_{air}] and the reference return air temperature T_{RA} is 26 [°C]. In heating mode, the reference return air temperature T_{RA} is 20/12 [°C] (dry bulb/wet bulb).









3.2.9. Air Distribution System

The air distribution system (Air Handling Unit, AHU) is very important because it is responsible for the air quality inside the building. Moreover, it has also the capability of reducing the cooling or heating energy requested from other equipment (i.e. fancoils, radiators, etc.). In fact, if the supply temperature is suitable, the ventilation air maintains the thermal comfort inside the considered rooms. During mild climate seasons (spring or autumn), especially if the building envelope is insulated, the ventilation air fulfills completely the building loads.

The AHU offers the advantage to filter the incoming air, removing dust, bacteria, and pollens, contributing to maintaining the air quality unaltered. This is especially useful in places where the windows cannot be opened, or the outside air has low quality (smog, pollutants, etc.).

In the Smart Energy Building, the AHU is coupled with the innovative air-to-air heat pump working with a constant air flow of approximately 4600 [m³/h]. The ventilation is working all day long when the building is occupied; the ventilation is shut down during nighttime or holidays. The distribution network is split between the two floors, each one has a dedicated ducted system. Figure 35 shows detail for the first-floor air distribution network. The red line represents the supply-air line while the blue is the extraction one. The supply line shows also the positions of the distribution terminals inside each room, with the corresponding volumetric flow rate and the dimensions (diameter or width and height) of the duct.

The scheme also shows the position of the fire and the calibration dampers. The return duct highlights the typology and positioning of the suction nozzles, with the corresponding flow rates. The main difference between air return valves and grills is the amount of air that they can remove. In fact, for smaller air flow rates, valves are preferred, and they are installed in bathrooms, grills are used to extract air from the classrooms and offices.

-  • Aluminum circular air diffuser;
-  • Air return valve;
-  • Air return grill;
-  • Aluminum air transit grill;
-  • Air pressure controller;
-  • Air differential pressure switch;
-  • Fire damper;
-  • Calibration damper;

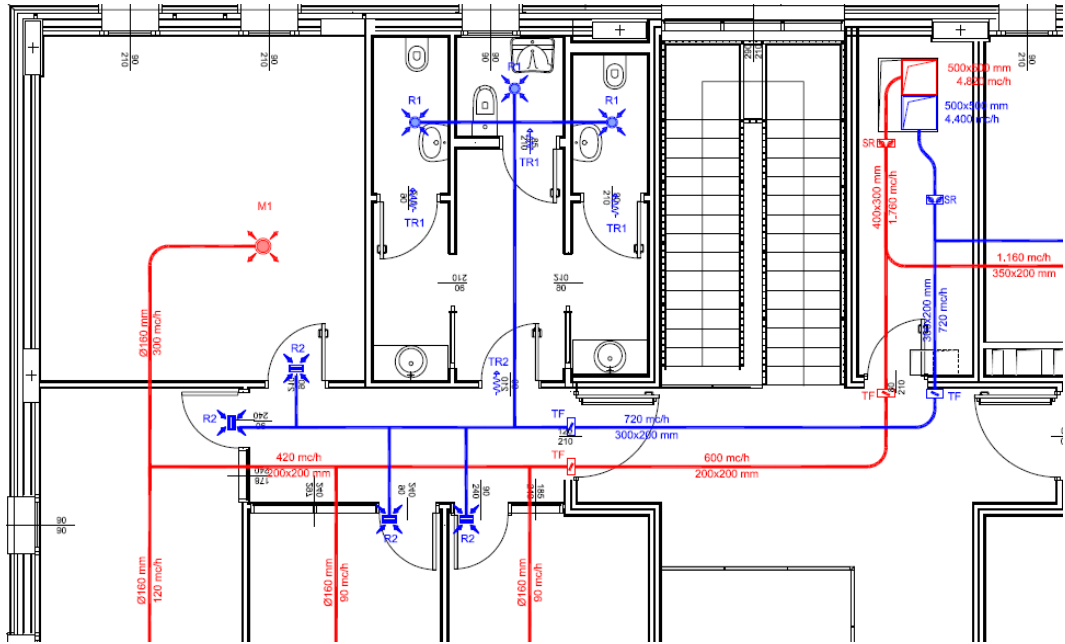


Figure 35: Air Distribution duct lines scheme, detail of the first floor

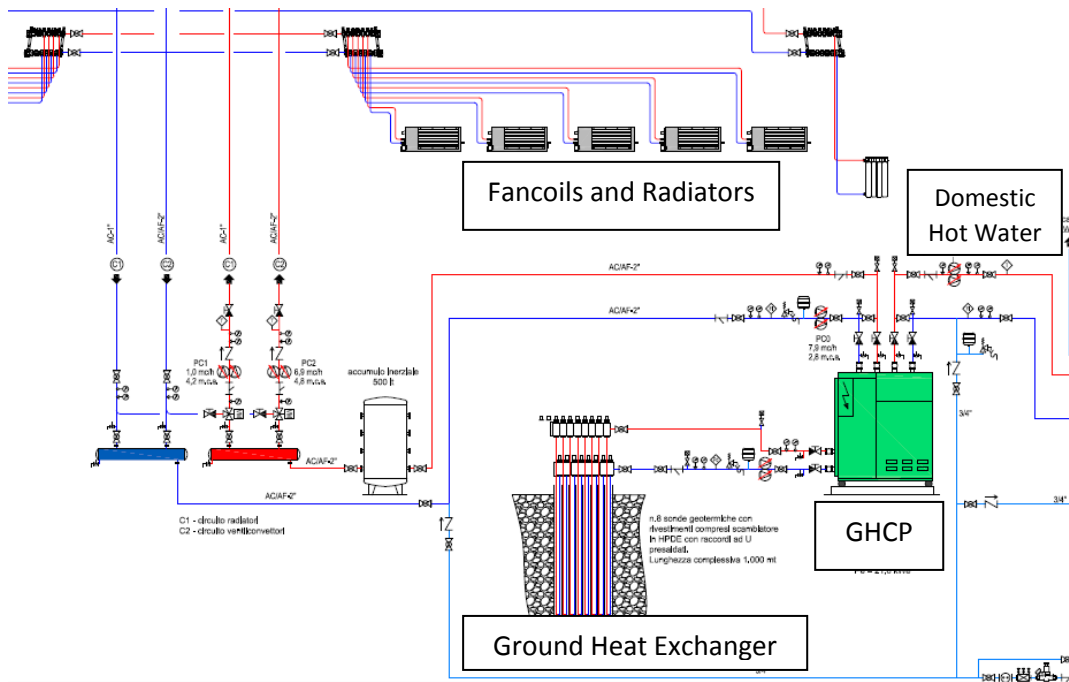


Figure 36: Detail of Water Distribution Scheme

3.2.10. Water Distribution System

The water distribution system is the energy carrier for the thermal and cooling power produced by the Ground Coupled Heat Pump (GHCP). It is delivering the hot and cold water from the heat pump to the fancoils and only hot water to the radiators of the building. The GHCP feeds an insulated water tank (capacity is 500 [l]), placed into the Solar and Geothermal Lab, not far from the heat pump itself, that is maintained at a constant temperature by the control system of the GHCP.

If the temperature varies too much (± 1.5 °C) from the desired set point temperature, the heat pump is turned on to bring it at the desired working condition. The temperature of the inertial tank is maintained at 20 [°C] during summer while it is maintained at 45 [°C] during winter. The water is circulated in the whole building by means of two dedicated pumps (brand Wilo-Stratos model 40/1-4).

Table 18 resumes the main information about fancoils and radiators. For each room, the number and typology of units, their thermal power (in both cooling and heating modes), the water flow rates and air flow rates in nominal conditions are listed.

Some spaces, like corridors or technical rooms, are not conditioned because they are not regularly occupied. Restrooms are equipped with radiators because, given the low amount of internal gains (low occupation, illumination working for a limited amount of time, no electrical plugs), the temperature is frequently below the thermal comfort levels.

Using the local units like the fancoils to regulate the temperature of a room is a common practice. Usually, the centralized system is working continuously, sending a fixed amount of air at a constant supply temperature, to fulfill the ventilation requirements of the conditioned spaces. This can be enough to maintain also the desired setpoint temperature if the heating or cooling loads of the conditioned spaces, served by the central system, are similar. Vice versa, when the central air system is serving rooms that possess different internal gains (i.e. with much different solar exposure, plug loads or occupancy levels) it is difficult that the central system can guarantee the comfort conditions of all the conditioned spaces simultaneously. For this reason, dedicated equipment (like fancoils) locally regulate the comfort levels of each room separately. In this way, the central ventilation system (Air Handling Unit, AHU) is dedicated to supplying enough fresh air to fulfill the ventilation requirements, while the dedicated local equipment is used to cover the cooling and heating peak loads.

The installed hydronic fancoil units are manufactured by Ventilclima, model "Air". The unit size depends on the thermal energy needs of every room. All the devices installed are configured to work with a "2-pipes" arrangement and the heat exchangers are made by 3 ranks. The datasheet provided by the manufacturer refers to some specific conditions at which the devices are tested. The main parameters that characterize the installed devices are listed for cooling and heating respectively.

Cooling:

- Water inlet temperature: 12 [°C];
- Water outlet temperature: 5 [°C];
- Air inlet temperature: 27 [°C] dry bulb conditions;

Heating:

- Water inlet temperature: 50 [°C];
- Water outlet temperature: 45 [°C];
- Air inlet temperature: 20 [°C] dry bulb conditions;

Table 18: Fancoil unit and radiators total thermal power and volumetric flow rates for each room

| Ground Floor | | | | | | | |
|----------------------------|--------------|-------------|--------------------|--------------------|-----------------------------------|-----------------------|---------------------|
| Room | Fancoil type | N° of units | Cooling Power [kW] | Heating Power [kW] | Air Flow Rate [m ³ /h] | Water Flow Rate [l/h] | Radiators Power [W] |
| Gym | C | 2 | 5.7 | 7.88 | 878 | 978 | - |
| Hall | C | 1 | 2.85 | 3.94 | 439 | 489 | - |
| Solar and Geo Lab | D | 3 | 11.13 | 15.54 | 1809 | 1908 | - |
| Restroom Solar and Geo Lab | NA | - | - | - | - | - | 870 |
| Combustion Lab | D | 3 | 11.13 | 15.54 | 1809 | 1908 | - |
| Restroom Combustion Lab | NA | - | - | - | - | - | 850 |
| First Floor | | | | | | | |
| Room | Fancoil type | N° of units | Cooling Power [kW] | Heating Power [kW] | Air Flow Rate [m ³ /h] | Water Flow Rate [l/h] | Radiators Power [W] |
| Office 1 | A | 1 | 1.94 | 2.46 | 292 | 340 | - |
| Office 2 | A | 1 | 1.94 | 2.46 | 292 | 340 | - |
| Office 3 | A | 1 | 1.94 | 2.46 | 292 | 340 | - |
| Rehe Lab Office | B | 2 | 4.94 | 6.98 | 842 | 882 | - |
| Relax Room | A | 1 | 1.94 | 2.46 | 292 | 340 | - |
| Restroom 1st floor | NA | - | - | - | - | - | 850 |
| Classroom 1 | B | 1 | 2.47 | 3.49 | 421 | 441 | - |
| Classroom 2 | B | 1 | 2.47 | 3.49 | 421 | 441 | - |
| Classroom 3 | B | 1 | 2.47 | 3.49 | 421 | 441 | - |
| Woman Dress Room | NA | - | - | - | - | - | 750 |
| Men Dress Room | NA | - | - | - | - | - | 750 |
| Hall | C | 1 | 2.92 | 3.94 | 439 | 489 | 0 |

The electrical motor installed in each unit is innovative and allows energy savings up to 50% [28] thanks to its dedicated control logic and constructive solutions. The innovative electric engine regulation card, with an opportune electronic modulation of voltage signals for each of the different windings, allows to create a precise rotating magnetic field and to precisely modify the rotational speed of the motor, adapting it to the required conditions.

3.3. Smart Energy Building Plants: Modeling in EnergyPlus

This part of the thesis aims to give a deeper insight into how the energy plants described in the previous paragraph are implemented into the model, starting from the reference model present in EnergyPlus.

3.3.1. Heat Pumps Reference Models

This paragraph presents the literature models selected in the present thesis to properly address the input in the Energy Plus program to simulate water-to-water and air-to-air heat pumps with COP as a function of temperature (Figure 37).

In particular, for the water-to-water heat pump, it was investigated also the effect of the volumetric flow rates, for both load and source sides. This was accomplished based on the manufacturer's data, which gives information about the Partial Load Factor (PLF). The detailed description here provided (and the related validations) are original contributions of the present thesis since Energy Plus references do not fully specify how the code can properly manage the running mode when inverse machines' performance has to be customized in terms of manufacturer information.

Models for heat pumps pertain to two main groups, with two different approaches to the problem [29]. On one hand, there are the "equation fit models", which consider the heat pump as a black box, whose behavior is simulated by means of correlations with coefficients derived from manufacturer data. On the other hand, there are "deterministic models", that considers each component of the system applying energy and mass conservation equations.

The main differences between the two approaches are the amount of data requested and the application aim. The equation fit models are easier because they need only the knowledge of the performance at the operating conditions usually given by the manufacturer [30], [31].

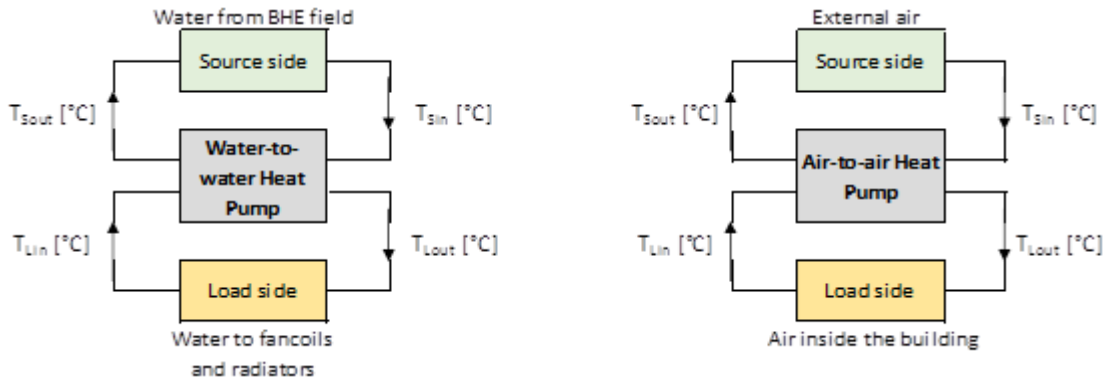


Figure 37: Heat pump operating conditions draft - (a) water-to-water HP - (b) air-to-air HP (without heat recovery).

On the contrary, deterministic models need data also for specific HP components: these parameters often derive from dedicated measurement campaigns and are not provided by the manufacturer. This approach is useful for the study and design of specific components of the heat pump.

In dynamic simulations over long periods (e.g. yearly simulations for building response to environmental conditions and internal energy transfers), the working conditions of a heat pump change continuously, and it is mandatory to include inside the model at least the COP variation with temperature. The starting point is the data provided by the manufacturer in terms of the performance coefficients of the heat pump in heating and cooling at reference working conditions.

This paper deals with HP modeling in EnergyPlus environment. The application of the “equation fit model” is applied for modeling a water-to-water heat hump (Curve Fit Method [32]) and an air-to-air heat pump [33] the latter being applied for heat recovery purposes on air ventilation circuit.

3.3.1.1. Water-to-water HP Reference Model

In EnergyPlus, two different options are available to model the water-to-water heat pumps, i.e. the “Curve Fit Method” and the “Parameter estimation-based model” [30].

For the case study reported in this thesis, the selected model is the “Curve Fit Method”, which allows quicker simulation of the water-to-water heat pump, avoiding the drawbacks associated with the more computationally expensive “Parameter estimation-based model”.

The variables that influence the water-to-water heat pump performance are mainly inlet water temperatures (source and load side) and water volumetric flow rates (source and load side).

The governing equations of the “Curve Fit Method” for the cooling and heating mode are given by (41), (42) and (43), (44) respectively.

Cooling Mode:

$$\frac{\dot{Q}_C}{\dot{Q}_{C,ref}} = A_1 + A_2 \left(\frac{T_{L,in}}{T_{ref}} \right) + A_3 \left(\frac{T_{S,in}}{T_{ref}} \right) + A_4 \left(\frac{\dot{V}_L}{\dot{V}_{L,ref}} \right) + A_5 \left(\frac{\dot{V}_S}{\dot{V}_{S,ref}} \right) \quad (41)$$

$$\frac{P_C}{P_{C,ref}} = B_1 + B_2 \left(\frac{T_{L,in}}{T_{ref}} \right) + B_3 \left(\frac{T_{S,in}}{T_{ref}} \right) + B_4 \left(\frac{\dot{V}_L}{\dot{V}_{L,ref}} \right) + B_5 \left(\frac{\dot{V}_S}{\dot{V}_{S,ref}} \right) \quad (42)$$

Heating Mode:

$$\frac{\dot{Q}_H}{\dot{Q}_{H,ref}} = D_1 + D_2 \left(\frac{T_{L,in}}{T_{ref}} \right) + D_3 \left(\frac{T_{S,in}}{T_{ref}} \right) + D_4 \left(\frac{\dot{V}_L}{\dot{V}_{L,ref}} \right) + D_5 \left(\frac{\dot{V}_S}{\dot{V}_{S,ref}} \right) \quad (43)$$

$$\frac{P_H}{P_{H,ref}} = E_1 + E_2 \left(\frac{T_{L,in}}{T_{ref}} \right) + E_3 \left(\frac{T_{S,in}}{T_{ref}} \right) + E_4 \left(\frac{\dot{V}_L}{\dot{V}_{L,ref}} \right) + E_5 \left(\frac{\dot{V}_S}{\dot{V}_{S,ref}} \right) \quad (44)$$

where the parameters are defined as:

- A_i, B_i, D_i, E_i : Equation fit coefficients for the cooling and heating mode [-]
- T_{ref} : Reference temperature, 283.15 [K]
- $T_{L,in}$: Load side inlet (in the HP) water temperature, [K]
- $T_{S,in}$: Source side inlet (in the HP) water temperature, [K]
- \dot{V}_L : Load side volumetric flow rate [m^3/s]
- \dot{V}_S : Source side volumetric flow rate [m^3/s]
- \dot{Q}_C, \dot{Q}_H : Load side heat transfer rate (cooling/heating mode) [W]
- P_C, P_H : Power consumption (cooling/ heating mode) [W]

The subscript “*ref*” indicates values at reference conditions that must be correctly specified. The reference temperature is always equal to 10°C (283.15 K) and even when available data from the manufacturer are provided at a different value, performance is to be recast to the above temperature.

In cooling mode, the reference conditions are when the heat pump is operating at the highest (nominal) cooling capacity indicated in the manufacturer’s technical references. The above condition does not match the real heat pump/chiller behavior, since its performance can be even better than those at the nominal capacity, provided that the working temperatures are “better” than the performance test ones. Similarly, in heating mode, the reference conditions are realized when the heat pump is operating at the highest (nominal) heating capacity.

In EnergyPlus, when selecting the “Curve Fit Method” to model water-to-water heat pumps, one must specify the parameters at the reference conditions and provide the equation fit coefficients.

Once the type of the water-to-water heat pump is selected, the generalized least square method is used for the evaluation of the coefficients A_i, B_i, D_i, E_i , based on the data available from the manufacturer’s catalogue [27].

The performance coefficients (*EER* in cooling mode and *COP* in heating mode) are evaluated as the ratio between the useful heat transfer rate (load side) from Equations (41)

and (43), while the related power consumption is given by Equation (42) and (44). Their equations as a function of inlet temperatures and volumetric flow rates are respectively:

Cooling Mode:

$$\frac{EER}{EER_{ref}} = \frac{A_1 + A_2 \left(\frac{T_{L,in}}{T_{ref}} \right) + A_3 \left(\frac{T_{S,in}}{T_{ref}} \right) + A_4 \left(\frac{\dot{V}_L}{\dot{V}_{L,ref}} \right) + A_5 \left(\frac{\dot{V}_S}{\dot{V}_{S,ref}} \right)}{B_1 + B_2 \left(\frac{T_{L,in}}{T_{ref}} \right) + B_3 \left(\frac{T_{S,in}}{T_{ref}} \right) + B_4 \left(\frac{\dot{V}_L}{\dot{V}_{L,ref}} \right) + B_5 \left(\frac{\dot{V}_S}{\dot{V}_{S,ref}} \right)} \quad (45)$$

Heating Mode:

$$\frac{COP}{COP_{ref}} = \frac{D_1 + D_2 \left(\frac{T_{L,in}}{T_{ref}} \right) + D_3 \left(\frac{T_{S,in}}{T_{ref}} \right) + D_4 \left(\frac{\dot{V}_L}{\dot{V}_{L,ref}} \right) + D_5 \left(\frac{\dot{V}_S}{\dot{V}_{S,ref}} \right)}{E_1 + E_2 \left(\frac{T_{L,in}}{T_{ref}} \right) + E_3 \left(\frac{T_{S,in}}{T_{ref}} \right) + E_4 \left(\frac{\dot{V}_L}{\dot{V}_{L,ref}} \right) + E_5 \left(\frac{\dot{V}_S}{\dot{V}_{S,ref}} \right)} \quad (46)$$

3.3.1.2. Air-to-air HP Reference Model

The Air-to-air heat pump is modeled, once more, with the “equation fit model” [33]. Assuming constant supply air volumetric flow rate as operating condition, the cooling or heating capacities and the corresponding EER or COP (and EIR = 1/EER) are only depending on temperatures and the selected equations to model the air-to-air heat pump are biquadratic ones. In particular, the performance depends on the “load air wet-bulb temperature” $T_{L,in\ wb}$ and the “source air dry-bulb temperature” $T_{S,in\ db}$ in cooling mode and on the “load air dry-bulb temperature” $T_{L,in\ db}$ and the “source air dry-bulb temperature” $T_{S,in\ db}$ in heating mode.

Cooling Mode

$$\frac{\dot{Q}_c}{\dot{Q}_{c,ref}} = \quad (47)$$

$$= a_0 + a_1 T_{L,in\ wb} + a_2 T_{L,in\ wb}^2 + a_3 T_{S,in\ db} + a_4 T_{S,in\ db}^2 + a_5 T_{L,in\ wb} T_{S,in\ db}$$

$$\frac{EIR}{EIR_{ref}} = \quad (48)$$

$$= b_0 + b_1 T_{L,in\ wb} + b_2 T_{L,in\ wb}^2 + b_3 T_{S,in\ db} + b_4 T_{S,in\ db}^2 + b_5 T_{L,in\ wb} T_{S,in\ db}$$

Heating Mode

$$\frac{\dot{Q}_H}{\dot{Q}_{H,ref}} = \quad (49)$$

$$= c_0 + c_1 T_{L,in\ db} + c_2 T_{L,in\ db}^2 + c_3 T_{S,in\ db} + c_4 T_{S,in\ db}^2 + c_5 T_{L,in\ db} T_{S,in\ db}$$

$$\frac{COP}{COP_{ref}} = \quad (50)$$

$$= d_0 + d_1 T_{L,in\ db} + d_2 T_{L,in\ db}^2 + d_3 T_{S,in\ db} + d_4 T_{S,in\ db}^2 + d_5 T_{L,in\ db} T_{S,in\ db}$$

In the previous Equations the parameters are defined as:

- \dot{Q}_C, \dot{Q}_H : \dot{Q}_C, \dot{Q}_H Load side heat transfer rate (cooling/heating mode) [W]
- EER : Overall efficiency in cooling mode (thermodynamic circuit and fans) [-]
- EIR : Performance coefficient in cooling mode ($=1/EER$) [-]
- COP : Overall efficiency in heating mode (thermodynamic circuit and fans) [-]
- a_i, b_i, c_i, d_i : Equation fit coefficients for the cooling and heating mode [-]
- $T_{L,in\,wb}$: Load side inlet (entering the HP) air wet bulb temperature, [K]
- $T_{L,in\,db}$: Load side inlet (entering the HP) air dry bulb temperature, [K]
- $T_{S,in\,db}$: Source side air inlet (entering the HP) dry bulb temperature, [K].

The subscript “*ref*” indicates values at reference conditions that must be correctly specified. In EnergyPlus the reference conditions are required both in cooling and in heating mode. For standard operating condition, in cooling mode, the reference load side air wet-bulb temperature $T_{L,in\,wb\,ref}$ is equal to 19.4°C (with a corresponding reference load side air dry-bulb temperature $T_{L,in\,db\,ref}$ equal to 26.7°C) whereas the source side air dry-bulb temperature is fixed at 35°C.

In heating mode, the reference load side air dry-bulb temperature $T_{L,in\,db\,ref}$ is equal to 21.1°C whereas the source side air dry-bulb temperature is fixed at 8.3°C.

In fact, for conventional reversible heat pumps, the load side conditions correspond to internal building ones (return air temperature T_{RA} [°C]) whereas source side conditions correspond to external ones (external air temperature T_{OA} [°C]).

The next paragraph describes the selected case study related to the plants of the Smart Energy Building (SEB) in the Unige Savona Campus, Italy. In particular, the water-to-water ground is coupled with the ground whereas the air-to-air heat pump is an innovative one with energy recovery.

3.3.2. Heat Pumps Model Implementation

Starting from the manufacturer's data provided in Paragraph 3.2.7, it is possible to implement the reference model proposed. This part of the work is crucial to correctly account for the real performance of the machine present in the Smart Energy Building.

3.3.2.1. Water-to-water HP Model Implementation

The first heat pump analyzed is the GCHP and the reference model is given by Equations (41-44). The machine is operating with a mixture of water and propylene glycol (30% concentration) for the geothermal heat exchanger hydraulic circuit. The manufacturer catalogue allows to evaluate the effect of temperature on the HP

performance (Tables 16 and Table 17) and it provides information about the effect of volumetric flow rates on the heat pump performance employing the Partial Load Factor. It is important to notice that the performance in

Tables 16 and Table 17 are provided as a function of the outlet temperatures ($T_{S,out}$ and $T_{L,out}$) while Equations (41), (42) and (43), (44) are function of the inlet temperatures, ($T_{S,in}$ and $T_{L,in}$). It is possible to link the inlet and outlet temperatures knowing the temperature difference at which the heat pump is operating. From the manufacturer catalogue, it was possible to obtain this information. In details, data refer to the following imposed temperature difference at the load and source sides for cooling case:

Cooling (ref.

Tables 16):

$$T_{L,in} = T_{L,out} + 5^{\circ}C \quad T_{S,in} = T_{S,out} - 5^{\circ}C \quad (51)$$

For heating case, the temperature difference is varying with the operative conditions. In particular, for lower temperatures ($T_{S,out} = 0, 1, 3 [^{\circ}C]$) the ΔT to be considered is 5 [$^{\circ}C$], while for higher temperatures, the ΔT to be considered is 3 [$^{\circ}C$].

Heating (ref. Table 17):

$$\text{for } T_{S,out} = 0, 1, 3 [^{\circ}C] \quad T_{L,in} = T_{L,out} - 5 [^{\circ}C] \quad T_{S,in} = T_{S,out} + 5 [^{\circ}C] \quad (52)$$

$$\text{for } T_{S,out} = 5, 7, 10, 12, 15, 17 [^{\circ}C]$$

$$T_{L,in} = T_{L,out} - 5 [^{\circ}C] \quad T_{S,in} = T_{S,out} + 3 [^{\circ}C] \quad (53)$$

The effect of the volumetric flow rates on the HP performance is expressed thanks to the PLF effect on the EER and COP. The information is limited only to the performance at PLF equal to 67% and 33%. This effect is beneficial for both the EER and the COP, as it can be observed from the manufacturer's catalogue data reported in Table 19.

Considering that both the source and load sides of the HP work at constant temperature difference according to Equations (51)-(53), the PLF represents not only the ratio between actual cooling or heating capacity and the maximum value but also the corresponding ratio between the water volumetric flow rates at the load side. From the values of EER or COP of Table 19, it is possible to deduce the power consumption (cooling and heating mode) and the source side heat transfer rate and, as a consequence the water volumetric flow rates at the source side.

The coefficients A_i , B_i , D_i and E_i of Equations (41)-(44) are not available from manufacturer references. The only way for assessing them is to iteratively guess their correct value by comparison with the available datasheet values and by minimizing an error. In this thesis, a simple optimum search process has been applied to cooling, heating and power consumption values provided by the manufacturer catalogue. The final calculated coefficients are presented in Table 20.

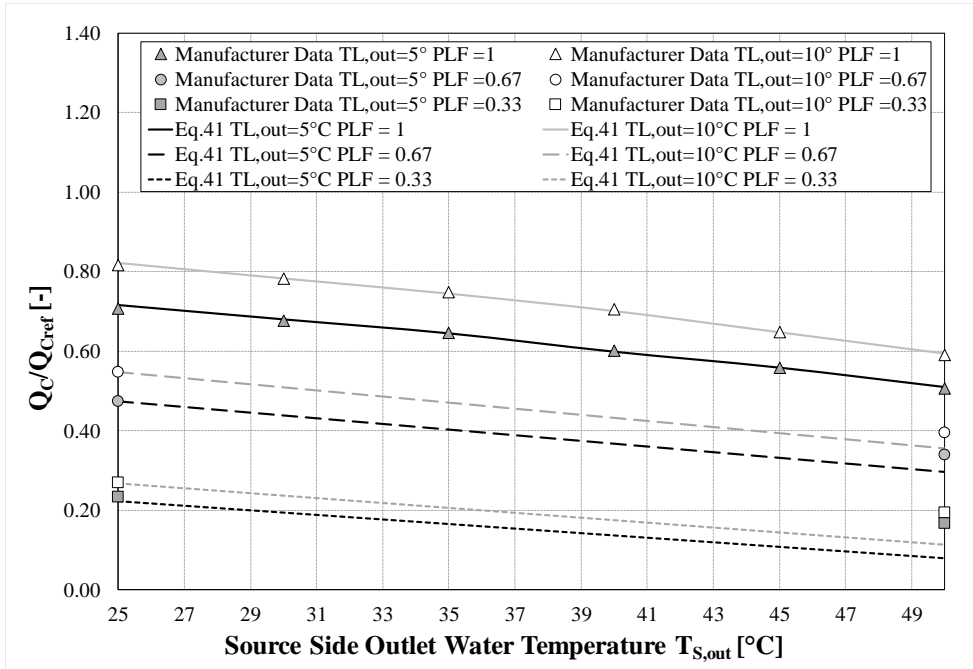
Figure 38 and Figure 39 compare the manufacturer data with the values obtained with the correlations expressed by Equation (41)-(44) using the optimal coefficients of Table 20. In particular, the graphs show the cooling/heating capacities and the electrical power consumption for cooling and heating respectively, as a function of the source side outlet water temperature $T_{S,out}$ with the load side outlet water temperature $T_{L,out}$ as parameter. Moreover, the graphs show the influence of the three different PLF conditions (0, 0.67, 0.33).

Table 19: Manufacturer data for Clivet model WSHN-XEE2. Effect of PLF on the HP performance

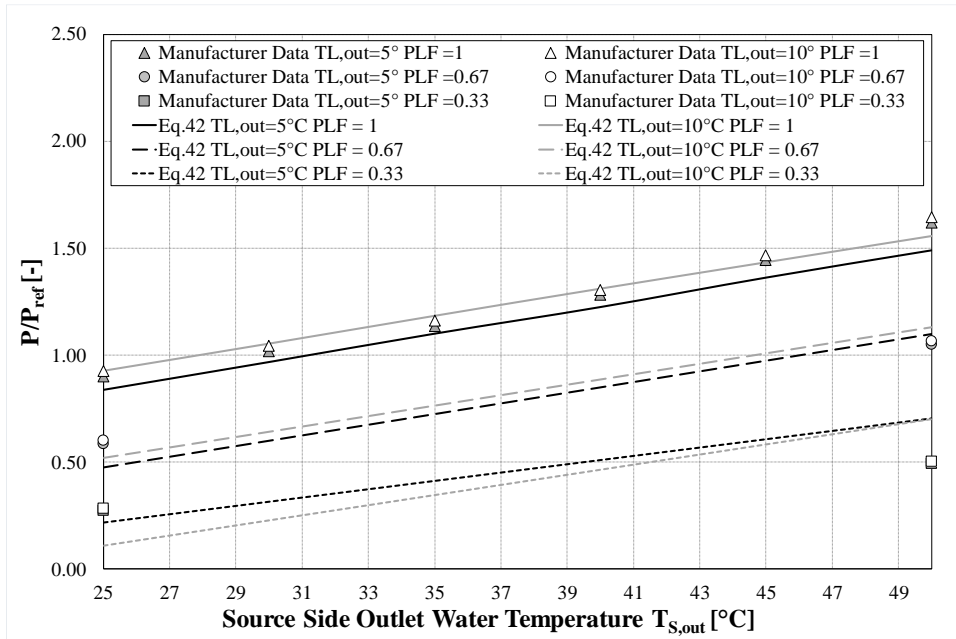
| PLF | EER/EER_{full load} | COP/COP_{full load} |
|------------|------------------------------------|------------------------------------|
| 0.33 | 1.080 | 1.146 |
| 0.67 | 1.032 | 1.103 |
| 1 | 1.000 | 1.000 |

Table 20: Calculated coefficients (optimum search approach) for the "Curve Fit Method" for the water-to-water HP

| | | | |
|----------------------|--------|----------------------|---------|
| A₁ | 0.957 | D₁ | 0.088 |
| A₂ | 0.407 | D₂ | -0.090 |
| A₃ | -1.326 | D₃ | 0.012 |
| A₄ | 0.076 | D₄ | 0.992 |
| A₅ | 0.916 | D₅ | 0.001 |
| B₁ | -5.181 | E₁ | 1.100 |
| B₂ | -1.927 | E₂ | 8.056 |
| B₃ | 6.627 | E₃ | -10.091 |
| B₄ | -1.503 | E₄ | 1.862 |
| B₅ | 2.930 | E₅ | 0.089 |

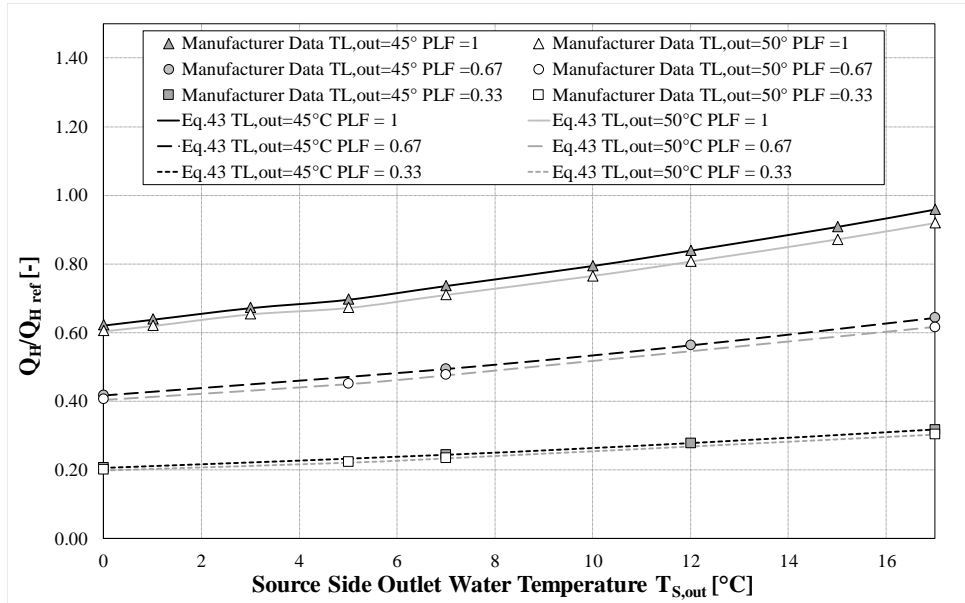


(a)

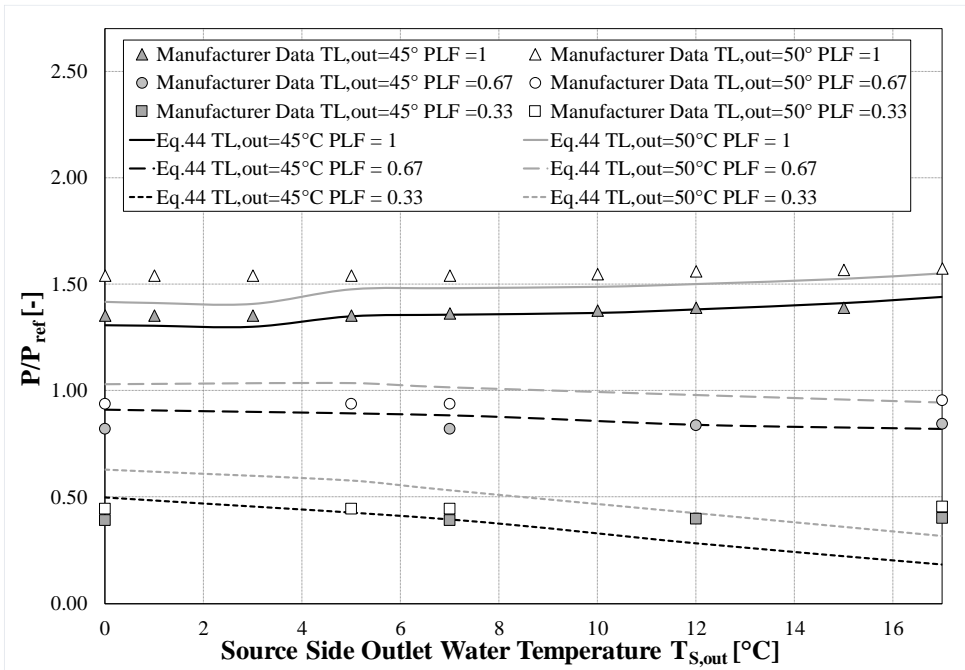


(b)

Figure 38: (a) $Q_c/Q_{c,ref}$ and (b) P/P_{ref} comparison for cooling mode



(a)



(b)

Figure 39: (a) $Q_H/Q_{H,ref}$ and (b) COP comparison for heating mode

During summer season, the cooling capacity \dot{Q}_C decreases for increasing source side outlet water temperature $T_{S,out}$ (fluid temperature entering in the BHE field) and increase for increasing load side outlet water temperature $T_{L,out}$ (fluid temperature to fancoils and radiators). Different behavior is exhibited by the power consumption P , in fact,

it increases if the source side outlet water temperature $T_{S,out}$ rises, while there is a poor effect from the variation of the load side outlet water temperature $T_{L,out}$. In general, both the cooling capacity and the power consumption decrease as the PLF is reduced, as it would be reasonable to expect.

A different situation is shown in Figure 39, which reports the winter operating mode for the considered heat pump. The heating capacity \dot{Q}_H increases for increasing source side outlet water temperature $T_{S,out}$ and it is slightly decreased for increasing load side outlet water temperature $T_{L,out}$. Considering the power consumption P , it is moderately affected by the source side outlet water temperature $T_{S,out}$ while it is increasing as the load side outlet water temperature $T_{L,out}$ rises.

The particular trend of the curve, with two inflection points for $T_{S,out} = 3$ and 5 [°C], is due to the particular operating conditions for the manufacturer's catalogue in heating mode. In fact, manufacture's Tables in heating mode are built for different imposed temperature differences at the load and source sides, according to Equation (53). Thus, at different source side "outlet" water temperatures $T_{S,out}$ correspond the same source side "inlet" water temperatures $T_{S,in} = 8$ [°C] that represents the input of Equations (43) and (44).

The agreement between manufacture dataset and "equation fit models" approach is good, with an average relative error lower than 7%, for both cooling and heating mode, when full load is considered. When partial load working points are considered the average relative error is rising, remaining below 15%.

3.3.2.2. Air-to-air HP Model Implementation

For the Smart Energy Building, the selected air-to-air heat pump associated with the air handling unit (AHU) is the Clivet Zephir CPAN-XHE3 Size 3, with a standard air flow of 4600 [m³/h]. This volumetric flow rate fulfills the ventilation requested by the Italian standards for the SEB building in terms of its volume and expected occupancy levels.

This air unit is very peculiar, especially if compared with the options conceived and available in Energy Plus. This system is a primary-air plant with a thermodynamic recovery of the energy contained in the return air. The primary air comes entirely from outdoor (fresh-air) at temperature T_{OA} whereas the return-air comes from the building inner rooms at temperature T_{RA} . The return air, before being released to the atmosphere, exchanges heat with the condenser in cooling mode and with the evaporator in heating mode. Return-air represents a favorable thermal source stable in time, offering lower temperature on the condenser side in cooling mode and higher temperature on the evaporator side in heating mode. As a consequence, the energy required by the compressors is reduced up to 50% [27]. The manufacturer catalogue provides the reversible heat pump performances as a function of external air temperature T_{OA} (dry bulb/wet bulb) and supply air temperature T_{SA} . Moreover, the manufacturer catalogue reports two different types of performance

coefficients, the thermodynamic efficiencies (EER_{th} and COP_{th}) and the overall efficiencies (EER and COP) that consider also the power of the auxiliary systems.

In cooling mode, the selected supply humidity ratio is equal to 11 [g_{vap}/kg_{air}] and the reference return air temperature T_{RA} is 26 [°C]. In heating mode, the reference return air temperature T_{RA} is 20/12 [°C] (dry bulb/wet bulb). To model the air-to-air HP in EnergyPlus, the operation mode without post-heating in cooling mode has been considered.

The distinctive operating conditions of the present heat pump (with energy recovery) allow it to reach high values of performance coefficients but create some challenges in modeling the system in EnergyPlus. In fact, the “load side” temperature becomes the external air temperature T_{OA} whereas the “source side” temperature is the return air temperature T_{RA} , both in cooling and in heating modes. Consequently, the reference conditions suggested from EnergyPlus (ref. paragraph 3.3.1) are no longer valid and new reference conditions are defined for the analyzed present heat pump.

In particular, in cooling mode, the new reference external air temperature T_{OA} is set to 40/25 [°C] (dry-bulb/wet-bulb) whereas the reference return air temperature T_{RA} is set to 26 [°C] (Table 21). In heating mode, the new reference external air temperature T_{OA} is set to -5 [°C] (dry-bulb) whereas the reference return air temperature T_{RA} is set to 20/12 [°C] (dry bulb/wet bulb) (Table 22).

The model for the air-to-air heat pump used to describe the SEB air-to-air heat pump is the Equation fit model, described by Equations (47)-(50) that express the cooling/heating capacities \dot{Q}_C, \dot{Q}_H and the EIR/COP as a function of both the external air temperature T_{OA} (dry-bulb/wet-bulb) and the return air temperature T_{RA} . Unfortunately (again a typical case when dealing with manufacturers datasheets), the data provided by the manufacturer are function of a unique value of the return temperature T_{RA} , namely 26 [°C] in cooling and 20/12 [°C] (dry bulb/wet bulb) in heating.

Thus, it is necessary to create an extended database to obtain, by optimization, the coefficients a_i, b_i, c_i and d_i of Equations (47)-(50): the selected return temperatures T_{RA} are 20, 22, 26 [°C]. By keeping constant the air volumetric flow rate, for the same external and supply conditions (temperature and humidity), also the cooling/heating capacities remain constant. On the contrary, modifying the return temperature conditions changes the “source temperature” and, therefore, the performance coefficients (EER/COP) and the compressor power are modified.

Table 21: Manufacturer datasheet values in cooling mode for present study analyses. Air handling unit model Zephir CPAN-XHE3 (air flow 4600 [m³/h], supply humidity ratio 11 g_{vap}/kg_{air}).

| Reference Conditions | | | | | |
|---|---|---|---------------------------------------|-------------------------------------|---------------------------|
| Ref. external air temperature (dry-bulb) TOA _{db} [°C] | Ref. external air temperature (wet-bulb) TOA _{wb} [°C] | Ref. return air temperature (dry-bulb) TRA _{db} [°C] | Ref. cooling capacity \dot{Q}_C [W] | Ref. compressor + fan power P [W] | Ref. EER _s [-] |
| 40 | 25 | 26 | 41900 | 16115 | 2.6 |
| Performance Data | | | | | |
| External air temperature (dry-bulb) TOA _{db} [°C] | External air temperature (wet-bulb) TOA _{wb} [°C] | Return air temperature (dry-bulb) RA _{db} [°C] | Cooling capacity \dot{Q}_C [W] | Compressor + fan power P [W] | EER _s [-] |
| 40 | 25 | 26 | 41900 | 16115 | 2.60 |
| 35 | 24 | 26 | 38700 | 13345 | 2.90 |
| 32 | 23 | 26 | 34000 | 10000 | 3.40 |
| 30 | 22 | 26 | 29100 | 6929 | 4.20 |
| 28 | 21 | 26 | 23600 | 4917 | 4.80 |
| 25 | 19 | 26 | 8100 | 2132 | 3.80 |

Table 22: Manufacturer datasheet values in heating mode for present study analyses. Air handling unit model Zephir CPAN-XHE3 (air flow 4600 m³/h).

| Reference Conditions | | | | |
|---|---|---------------------------|-------------------------------------|---------------------------|
| Ref. external air temperature (dry-bulb) TOA _{db} [°C] | Ref. return air temperature (dry-bulb) TRA _{db} [°C] | Ref. heating capacity [W] | Ref. compressor + fan power P [W] | Ref. COP _s [-] |
| -5 | 20 | 49700 | 11044 | 4.50 |
| Performance Data | | | | |
| External air temperature (dry-bulb) TOA _{db} [°C] | Return air temperature (dry-bulb) TRA _{db} [°C] | Heating capacity [W] | Compressor + fan power P [W] | COP _s [-] |
| -5 | 20 | 49700 | 11044 | 4.50 |
| 0 | 20 | 49500 | 12375 | 4.00 |
| 2 | 20 | 46200 | 11268 | 4.10 |
| 7 | 20 | 37100 | 8065 | 4.60 |
| 12 | 20 | 28400 | 5462 | 5.20 |

The values of the thermodynamic performance coefficients (EER_{th}/COP_{th}) for the new values of the return temperatures T_{RA} are obtained starting from the manufacturer's data and using the Carnot Law. Operatively, they are calculated by multiplying the corresponding Carnot performance coefficients ($EER_{Carnot}/COP_{Carnot}$), based on the evaporator and condenser temperatures, by two sets of constants C_{Ci}/C_{Hi} that are assumed dependent on the supply air temperature T_{SA} but independent from the return temperatures T_{RA} .

In cooling mode, the thermodynamic performance coefficients EER_{th} results:

$$EER_{th} = C_{Ci} \cdot EER_{Carnot} = C_{Ci} \cdot \frac{T_{evap}}{T_{cond} - T_{evap}} \quad (54)$$

The evaporator temperature T_{evap} is assumed nearly equal to the supply air temperature T_{SA} whereas the condenser temperature T_{cond} is evaluated by means of energy balances on the components of the HP.

In heating mode, the thermodynamic performance coefficients COP_{th} results:

$$COP_{th} = C_{Hi} \cdot COP_{Carnot} = C_{Hi} \cdot \frac{T_{cond}}{T_{cond} - T_{evap}} \quad (55)$$

The condenser temperature T_{cond} is assumed nearly equal to the supply air temperature T_{SA} whereas the evaporator temperature T_{evap} is evaluated by means of energy balances on the components of the heat pump.

The last step is to deduce the total coefficients of performances (EER and COP) including also the auxiliary systems, by assuming that the fan electrical consumption of the heat pump is constant and equal to 1 [kW] for all the different operating conditions. This is acceptable considering that the real heat pump works at a constant air mass flow rate (equal to 4600 [m³/h]) during its operating conditions.

The results of this analysis are presented in Table 23 and Table 24, in cooling and heating mode respectively (calculated data points are highlighted in grey).

Finally, by means of an optimum search process comparing the performance values of Table 23 and Table 24, the coefficients a_i , b_i , c_i , and d_i of Equations (47)-(50) have been obtained and the results are presented in Table 25.

As an example, Figure 40 and Figure 41 show the cooling/heating capacities and the HP performances (EIR/COP) as a function of external conditions T_{OA} and return temperature T_{RA} as a parameter.

Table 23: Datasheet values in cooling mode for present study analyses (calculated data points in grey). Air handling unit model Zephir CPAN-XHE3 (air flow 4600 [m³/h], supply humidity ratio 11 [g_{vap}/kg_{air}]).

| Reference Conditions | | | | | |
|---|---|---|---------------------------------------|-------------------------------------|---------------------------|
| Ref. external air temperature (dry-bulb) TOA _{db} [°C] | Ref. external air temperature (wet-bulb) TOA _{wb} [°C] | Ref. return air temperature (dry-bulb) TRA _{db} [°C] | Ref. cooling capacity \dot{Q}_C [W] | Ref. compressor + fan power P [W] | Ref. EER _s [-] |
| 40 | 25 | 26 | 41900 | 16115 | 2.6 |
| Performance Data | | | | | |
| External air temperature (dry-bulb) TOA _{db} [°C] | External air temperature (wet-bulb) TOA _{wb} [°C] | Return air temperature (dry-bulb) RA _{db} [°C] | Cooling capacity \dot{Q}_C [W] | Compressor + fan power P [W] | EER _s [-] |
| 40 | 25 | 26 | 41900 | 16115 | 2.60 |
| 35 | 24 | 26 | 38700 | 13345 | 2.90 |
| 32 | 23 | 26 | 34000 | 10000 | 3.40 |
| 30 | 22 | 26 | 29100 | 6929 | 4.20 |

| | | | | | |
|----|----|----|-------|-------|------|
| 28 | 21 | 26 | 23600 | 4917 | 4.80 |
| 25 | 19 | 26 | 8100 | 2132 | 3.80 |
| 40 | 25 | 22 | 41900 | 14249 | 2.94 |
| 35 | 24 | 22 | 38700 | 12009 | 3.22 |
| 32 | 23 | 22 | 34000 | 8794 | 3.87 |
| 30 | 22 | 22 | 29100 | 6095 | 4.77 |
| 28 | 21 | 22 | 23600 | 4292 | 5.50 |
| 25 | 19 | 22 | 8100 | 1735 | 4.67 |
| 40 | 25 | 20 | 41900 | 13383 | 3.13 |
| 35 | 24 | 20 | 38700 | 11273 | 3.43 |
| 32 | 23 | 20 | 34000 | 8224 | 4.13 |
| 30 | 22 | 20 | 29100 | 5675 | 5.13 |
| 28 | 21 | 20 | 23600 | 3971 | 5.94 |
| 25 | 19 | 20 | 8100 | 1515 | 5.35 |

Table 24: Datasheet values in heating mode for present study analyses (calculated data points in grey). Air handling unit model Zephir CPAN-XHE3 (air flow 4600 [m³/h])

| Reference Conditions | | | | |
|---|---|---------------------------|-----------------------------------|---------------------------|
| Ref. external air temperature (dry-bulb) TOA _{db} [°C] | Ref. return air temperature (dry-bulb) TRA _{db} [°C] | Ref. heating capacity [W] | Ref. compressor + fan power P [W] | Ref. COP _s [-] |
| -5 | 20 | 49700 | 11044 | 4.50 |
| Performance Data | | | | |
| External air temperature (dry-bulb) TOA _{db} [°C] | Return air temperature (dry-bulb) TRA _{db} [°C] | Heating capacity [W] | Compressor + fan power P [W] | COP _s [-] |
| -5 | 20 | 49700 | 11044 | 4.50 |
| 0 | 20 | 49500 | 12375 | 4.00 |
| 2 | 20 | 46200 | 11268 | 4.10 |
| 7 | 20 | 37100 | 8065 | 4.60 |
| 12 | 20 | 28400 | 5462 | 5.20 |
| -5 | 22 | 49700 | 10592 | 4.69 |
| 0 | 22 | 49500 | 11717 | 4.22 |
| 2 | 22 | 46200 | 10738 | 4.30 |
| 7 | 22 | 37100 | 7712 | 4.81 |
| 12 | 22 | 28400 | 5254 | 5.41 |
| -5 | 26 | 49700 | 9469 | 5.25 |
| 0 | 26 | 49500 | 10633 | 4.66 |
| 2 | 26 | 46200 | 9703 | 4.76 |
| 7 | 26 | 37100 | 6868 | 5.40 |
| 12 | 26 | 28400 | 4605 | 6.17 |

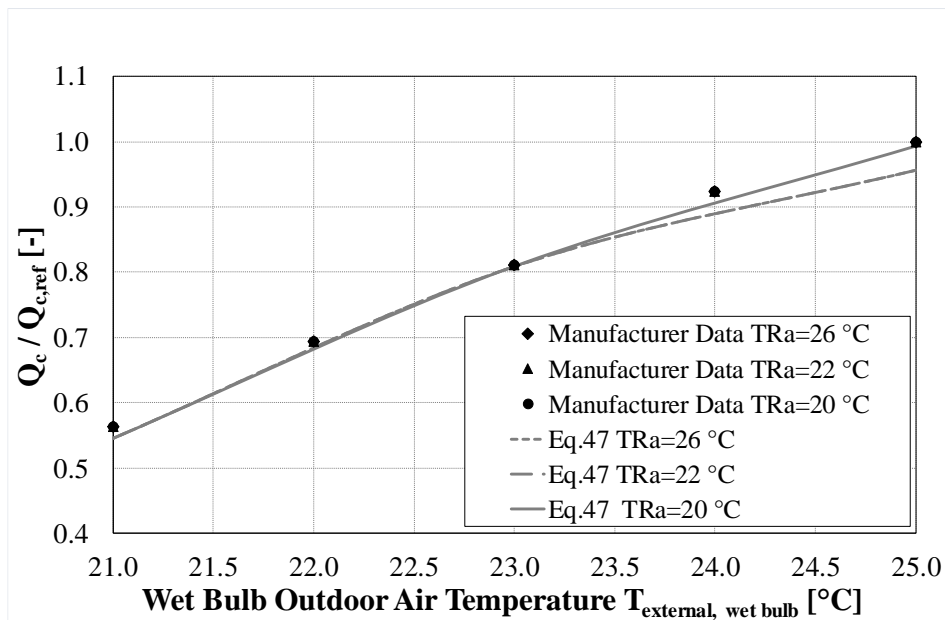
Table 25: Calculated coefficients for the “Equation Fit Approach”, air-to-air heat pump

| | | | | | | | |
|-------|----------|-------|----------|-------|----------|-------|----------|
| a_0 | -6.04980 | b_0 | -2.20000 | c_0 | -0.06076 | d_0 | 0.59269 |
| a_1 | 0.48670 | b_1 | 0.11000 | c_1 | -0.00423 | d_1 | 0.02513 |
| a_2 | -0.00820 | b_2 | 0.00000 | c_2 | -0.00148 | d_2 | -0.00190 |
| a_3 | 0.00000 | b_3 | 0.00300 | c_3 | 0.08791 | d_3 | 0.05807 |
| a_4 | 0.00000 | b_4 | 0.00056 | c_4 | -0.00186 | d_4 | -0.00171 |
| a_5 | 0.00000 | b_5 | 0.00000 | c_5 | -0.00053 | d_5 | -0.00094 |

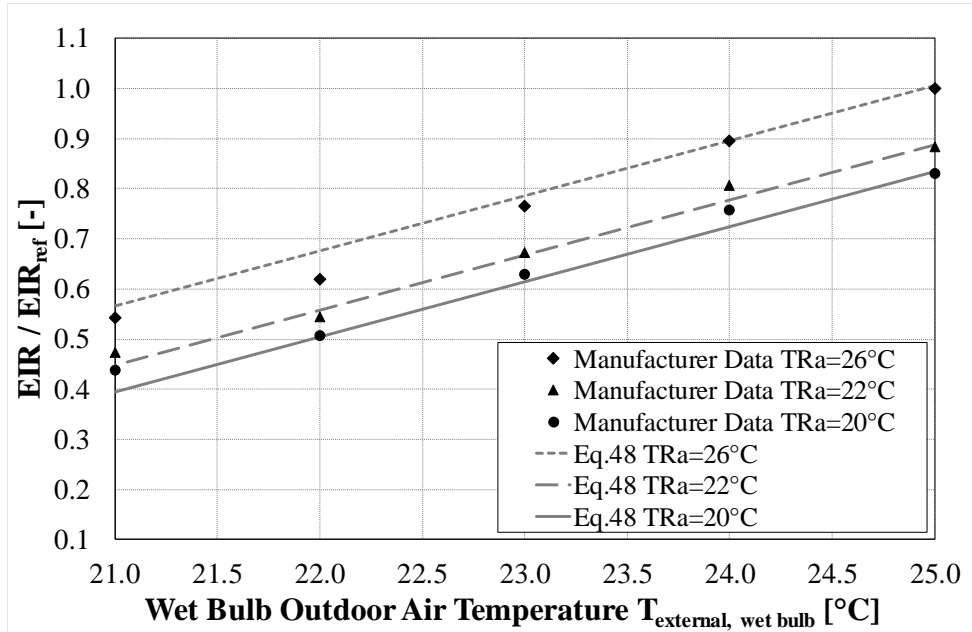
From the analysis of Figure 40 and Figure 41, it is possible to obtain some interesting information. Firstly, keeping constant the volumetric flow rate, the external temperature T_{OA} and the supply conditions (temperature and humidity), the cooling and heating capacities \dot{Q}_C, \dot{Q}_H remain almost constant for the different return air conditions T_{RA} . Secondly, the cooling capacity \dot{Q}_C (requested by the building) increases with the external temperature T_{OA} whereas the heating capacity \dot{Q}_H (requested by the building) decreases increasing the external temperature T_{OA} .

On the contrary, the performance parameters $EIR (=1/EER)$ and COP depend on both the external and return air temperature. In cooling mode, the EIR increases with the external air temperature T_{OA} (load side temperature) and increases with the return air temperature T_{RA} (source side temperature). In heating mode, the COP decreases as the return air temperature T_{RA} is increased (source side temperature) whereas it decreases with the external air temperature (load side temperature) for $T_{OA} > 0^\circ\text{C}$. For $T_{OA} < 0^\circ\text{C}$, the COP increase with the external air temperature because of the energy consumption of the defrost contribution.

The agreement between manufacturer data and best-fit curves is good and the coefficients can be implemented in EnergyPlus to represent the behavior of the present air-to-air heat pump. The average relative error (fit profiles vs manufactured data) in cooling is about 2.3% for the cooling \dot{Q}_C capacity and 3.3% for the EER . In heating mode, the average relative error is 2.4% for the heating capacity \dot{Q}_H and 2.6% for the COP .

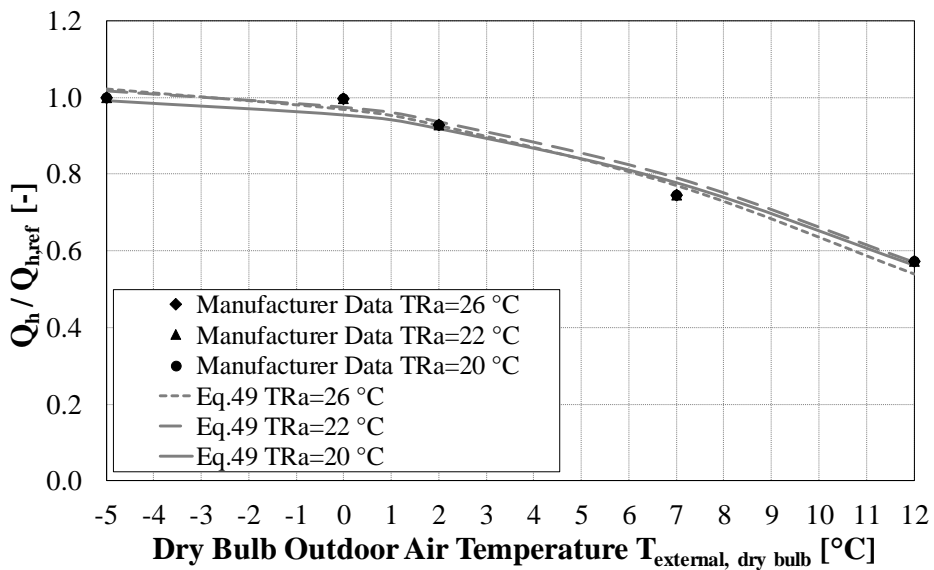


(a)



(b)

Figure 40: HP performances in cooling mode, comparison between manufacturer data and Equations (47) and (48)



(a)

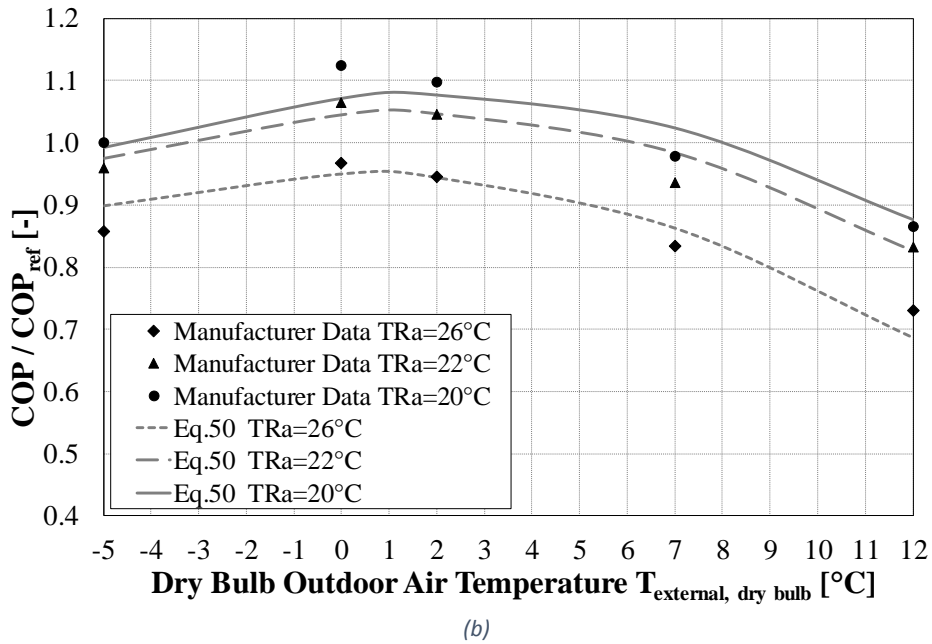


Figure 41: HP performances in heating mode, comparison between manufacturer data and Equations (49) and (50)

3.3.3. Heat Pumps Models Validations

3.3.3.1. Water-to-water HP Model Validation

The proposed simplified version of the “Curve Fit Method” presented in the previous Paragraphs has been validated with reference benchmark simulations in EnergyPlus.

A simplified model has been created for this purpose, with a building able to work at nearly constant operating conditions for the whole simulation period, i.e. 1 month. The modeled building is equipped with the GCHP Clivet WSHN-XEE2 MF 14.2 and both cooling and heating modes are simulated. Different working conditions are analyzed, imposing different load side outlet $T_{L,out}$ and source side inlet $T_{S,in}$ water temperature. The load of the building and the thermal response of the ground are properly calibrated to maintain the desired temperature difference at the source and load sides, as shown by Equations (51)-(53). The results are presented in Table 26 and

Table 27 where the first two columns represent the imposed operating temperatures. The results are presented for the full load operating conditions.

From EnergyPlus simulations is possible to infer the inlet load and outlet source temperatures and verify that the temperature differences at the source and load sides are

comparable to the desired values (Equations (51)-(53)). The performance values (EER/COP) are evaluated from the ratio between the simulated values of cooling or heating capacity \dot{Q}_C, \dot{Q}_H and the electrical consumptions P . These simulated performances are then compared with the values calculated employing the Simplified Curve Fit Method, obtaining a very good agreement.

The average absolute relative error on EER in cooling is nearly 0.15% whereas on COP in heating is nearly 0.6%. The comparison, in terms of EER and COP , is represented graphically in Figure 42 and Figure 43, for cooling and heating mode, respectively.

Table 26: Benchmark simulations for the water-to-water heat pump (cooling case)

| Operating conditions | | Energy Plus simulations | | | | Simplified Curve Fit Method | | | |
|----------------------|-----------------|-------------------------|------------------|--------------------|----------------------|-----------------------------|-------------------------------------|---------------|---------------------------------------|
| $T_{L,out}$ [°C] | $T_{S,in}$ [°C] | $T_{L,in}$ [°C] | $T_{S,out}$ [°C] | Electric Power [W] | Cooling Capacity [W] | EER [-] | EER _{ref} [-] interpolated | T_{ref} [K] | EER [-] Eq. (45) with coeff. Table 20 |
| 5 | 20 | 9.40 | 24.50 | 4500 | 25699 | 5.71 | 5.55 | 283.15 | 5.72 |
| 5 | 25 | 9.18 | 29.43 | 5340 | 24396 | 4.57 | 4.69 | 283.15 | 4.58 |
| 5 | 30 | 9.18 | 34.61 | 6544 | 24396 | 3.73 | 3.98 | 283.15 | 3.73 |
| 5 | 35 | 9.18 | 39.82 | 7942 | 24395 | 3.07 | 3.27 | 283.15 | 3.08 |
| 5 | 40 | 9.18 | 45.06 | 9582 | 24394 | 2.55 | 2.67 | 283.15 | 2.55 |
| 5 | 45 | 9.18 | 50.35 | 11535 | 24392 | 2.11 | 2.13 | 283.15 | 2.12 |
| 7 | 20 | 11.31 | 24.38 | 4240 | 25148 | 5.93 | 5.80 | 283.15 | 5.94 |
| 7 | 25 | 11.31 | 29.53 | 5244 | 25148 | 4.80 | 4.68 | 283.15 | 4.80 |
| 7 | 30 | 11.31 | 34.70 | 6387 | 25148 | 3.94 | 4.21 | 283.15 | 3.94 |
| 7 | 35 | 11.31 | 39.89 | 7701 | 25148 | 3.27 | 3.51 | 283.15 | 3.27 |
| 7 | 40 | 11.31 | 45.12 | 9232 | 25166 | 2.73 | 2.85 | 283.15 | 2.73 |
| 7 | 45 | 11.31 | 50.39 | 11025 | 25162 | 2.28 | 2.26 | 283.15 | 2.29 |
| 12 | 20 | 16.48 | 24.49 | 4016 | 26105 | 6.50 | 6.34 | 283.15 | 6.51 |
| 12 | 25 | 16.48 | 29.62 | 4904 | 26105 | 5.32 | 5.42 | 283.15 | 5.33 |
| 12 | 30 | 16.48 | 34.77 | 5898 | 26105 | 4.43 | 4.65 | 283.15 | 4.43 |
| 12 | 35 | 16.48 | 39.93 | 7019 | 26105 | 3.72 | 3.92 | 283.15 | 3.72 |
| 12 | 40 | 16.48 | 45.12 | 8293 | 26105 | 3.15 | 3.18 | 283.15 | 3.15 |
| 12 | 45 | 16.48 | 50.34 | 9754 | 26105 | 2.68 | 2.53 | 283.15 | 2.68 |
| 15 | 20 | 19.50 | 24.47 | 3845 | 26193 | 6.81 | 6.75 | 283.15 | 6.82 |
| 15 | 25 | 19.50 | 29.60 | 4664 | 26193 | 5.62 | 5.79 | 283.15 | 5.62 |
| 15 | 30 | 19.50 | 34.73 | 5574 | 26193 | 4.70 | 4.98 | 283.15 | 4.71 |
| 15 | 35 | 20.07 | 40.02 | 6713 | 26994 | 4.02 | 4.17 | 283.15 | 4.03 |
| 15 | 40 | 20.07 | 44.95 | 7505 | 25743 | 3.43 | 3.45 | 283.15 | 3.43 |
| 15 | 45 | 20.07 | 50.01 | 8529 | 25085 | 2.94 | 2.78 | 283.15 | 2.95 |
| 18 | 20 | 22.49 | 24.44 | 3674 | 26118 | 7.11 | 7.04 | 283.15 | 7.12 |
| 18 | 25 | 22.49 | 29.55 | 4430 | 26118 | 5.90 | 6.07 | 283.15 | 5.90 |
| 18 | 30 | 22.49 | 34.68 | 5265 | 26118 | 4.96 | 5.27 | 283.15 | 4.97 |
| 18 | 35 | 22.49 | 39.81 | 6191 | 26118 | 4.22 | 4.44 | 283.15 | 4.22 |
| 18 | 40 | 22.50 | 44.98 | 7244 | 26196 | 3.62 | 3.63 | 283.15 | 3.62 |
| 18 | 45 | 22.50 | 50.16 | 8407 | 26196 | 3.12 | 2.95 | 283.15 | 3.12 |

Table 27: Benchmark simulations for the water-to-water heat pump (heating case)

| Operating conditions | | Energy Plus simulations | | | | | Simplified Curve Fit Method | | | |
|----------------------|-----------------|-------------------------|------------------|--------------------|----------------------|---------|-------------------------------------|----------------|----------------------------------|--|
| $T_{L,out}$ [°C] | $T_{S,in}$ [°C] | $T_{L,in}$ [°C] | $T_{S,out}$ [°C] | Electric Power [W] | Heating Capacity [W] | COP [-] | COP _{ref} [-] interpolated | T_{ref} [°C] | COP Eq.(46) with coeff. Table 20 | |
| 30.0 | 6 | 24.6 | 1.8 | 10000 | 59092 | 5.91 | 5.95 | 283.15 | 5.92 | |
| 30.0 | 10 | 24.6 | 7.4 | 9045 | 59092 | 6.53 | 6.62 | 283.15 | 6.64 | |
| 30.0 | 15 | 24.6 | 12.4 | 8006 | 59092 | 7.38 | 7.42 | 283.15 | 7.49 | |
| 30.0 | 18 | 24.6 | 13.6 | 7452 | 59092 | 7.93 | 7.63 | 283.15 | 7.99 | |
| 30.0 | 20 | 24.6 | 17.3 | 7108 | 59092 | 8.31 | 8.28 | 283.15 | 8.31 | |
| 34.6 | 6 | 28.7 | 1.5 | 12260 | 65200 | 5.32 | 5.13 | 283.15 | 5.24 | |
| 34.6 | 8 | 28.7 | 5.2 | 11642 | 65200 | 5.60 | 5.48 | 283.15 | 5.57 | |
| 34.6 | 12 | 28.7 | 9.2 | 10525 | 65200 | 6.19 | 6.04 | 283.15 | 6.20 | |
| 35.0 | 15 | 29.0 | 12.3 | 9453 | 62534 | 6.62 | 6.48 | 283.15 | 6.61 | |
| 35.0 | 20 | 29.0 | 17.2 | 8383 | 62534 | 7.46 | 7.21 | 283.15 | 7.36 | |
| 45.0 | 5 | 38.5 | 0.9 | 16101 | 63962 | 3.97 | 3.88 | 283.15 | 3.92 | |
| 45.0 | 6 | 38.5 | 1.9 | 15649 | 63962 | 4.09 | 3.98 | 283.15 | 4.06 | |
| 45.0 | 10 | 38.5 | 7.4 | 14015 | 63962 | 4.56 | 4.52 | 283.15 | 4.59 | |
| 45.0 | 18 | 38.5 | 15.3 | 11398 | 63962 | 5.61 | 5.42 | 283.15 | 5.61 | |
| 45.0 | 20 | 38.5 | 17.3 | 10848 | 63962 | 5.90 | 5.68 | 283.15 | 5.86 | |
| 50.0 | 8 | 42.8 | 6.1 | 13108 | 50297 | 3.84 | 3.70 | 283.15 | 3.93 | |
| 49.6 | 13 | 46.1 | 8.3 | 11169 | 43586 | 3.90 | 3.91 | 283.15 | 3.90 | |
| 50.0 | 10 | 44.9 | 10.9 | 11911 | 51803 | 4.35 | 4.16 | 283.15 | 4.35 | |
| 50.0 | 15 | 45.1 | 12.8 | 11982 | 54673 | 4.56 | 4.34 | 283.15 | 4.56 | |
| 50.0 | 18 | 45.1 | 15.8 | 11151.4 | 54673.3 | 4.90 | 4.66 | 283.15 | 4.90 | |
| 50.0 | 20 | 45.1 | 17.7 | 10665.7 | 54673.3 | 5.13 | 4.88 | 283.15 | 5.13 | |

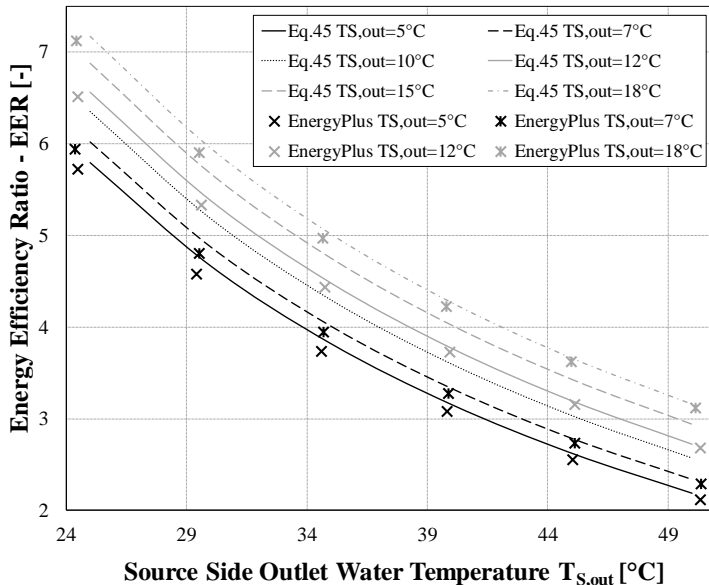


Figure 42: EER in cooling mode: comparison between EnergyPlus simulations and equation fit model approach

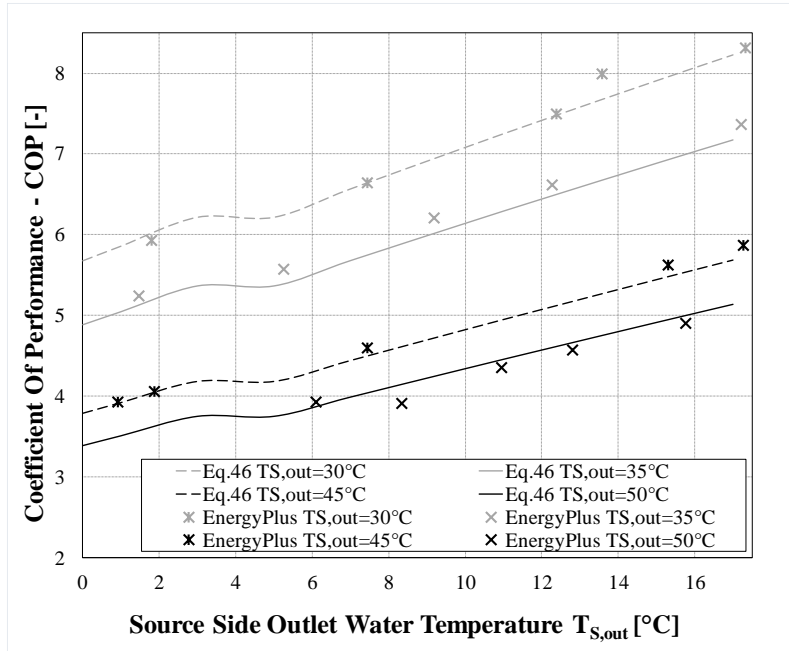


Figure 43: COP in heating mode: comparison between EnergyPlus simulations and equation fit model approach

3.3.3.2. Air-to-air HP Model Validation

The equation fit model approach has been implemented in EnergyPlus also for the air-to-air heat pump, through Equations (47)-(50) with the coefficients listed in Table 25. Similarly to the procedure followed for the water-to-water model validation, a simplified building model has been created. The simplified model allowed to maintain nearly constant operating conditions for the whole simulation duration, i.e. 1 month. The modeled building is equipped with the Clivet Zephir CPAN-XHE3 Size 3 and both cooling and heating are simulated.

Table 28: Benchmark simulations for the air-to-air heat pump (cooling case)

| Cooling Mode | | | | | | | | | | |
|---------------------------|---------------------------|---------------------------|---------------------------|---------------------------|---------------------|---------|----------------------|-----------------------------|---------|----------------------|
| Operating conditions | | | Energy Plus simulations | | | | | Simplified Curve Fit Method | | |
| TOA _{db} [°C] | TOA _{wb} [°C] | TRA _{db} [°C] | TOA _{wb} [°C] | TRA _{db} [°C] | Q̇ _C [W] | P [W] | EER _s [-] | Q̇ _C [W] | P [W] | EER _s [-] |
| 28 | 21 | 20 | 21.04 | 20.1 | 22862.6 | 3538.5 | 6.5 | 23241.9 | 3522.0 | 6.6 |
| 28 | 21 | 22 | 21.04 | 22.2 | 22862.6 | 4062.9 | 5.6 | 23241.9 | 3996.2 | 5.8 |
| 28 | 21 | 26 | 21.04 | 25.9 | 22862.6 | 5024.3 | 4.6 | 23241.9 | 5064.6 | 4.6 |
| 32 | 23 | 20 | 19.84 | 19.8 | 33887.8 | 8078.1 | 4.2 | 33792.4 | 7980.2 | 4.2 |
| 32 | 23 | 22 | 20.39 | 20.4 | 33887.8 | 8264.8 | 4.1 | 33792.4 | 8669.6 | 3.9 |
| 32 | 23 | 26 | 26.14 | 26.1 | 33887.8 | 10314.1 | 3.3 | 33792.4 | 10223.0 | 3.3 |
| 40 | 25 | 20 | 25.07 | 20.1 | 41594.1 | 13449.5 | 3.1 | 41594.1 | 13342.1 | 3.1 |
| 40 | 25 | 22 | 25.07 | 22.2 | 40063.4 | 13835.6 | 2.9 | 41594.1 | 14190.6 | 2.9 |
| 40 | 25 | 26 | 25.07 | 25.9 | 40063.4 | 15510.1 | 2.6 | 41594.1 | 16102.7 | 2.6 |

Table 29: Benchmark simulations for the air-to-air heat pump (heating case)

| Heating Mode | | | | | | | | | | |
|---------------------------|---------------------------|---------------------------|---------------------------|---------------------|-------|----------------------|-----------------------------|--------|----------------------|--|
| Operating conditions | | | Energy Plus simulations | | | | Simplified Curve Fit Method | | | |
| TOA _{db} [°C] | TRA _{db} [°C] | TOA _{db} [°C] | TRA _{db} [°C] | Q̇ _H [W] | P [W] | COP _s [-] | Q̇ _H [W] | P [W] | COP _s [-] | |
| -5 | 20 | -5.0 | 20.01 | 45426 | 10007 | 4.54 | 49292 | 10873 | 4.5 | |
| -5 | 22 | -5.0 | 21.99 | 45426 | 9816 | 4.63 | 50538 | 10949 | 4.6 | |
| -5 | 26 | -5.0 | 26.04 | 45426 | 9071 | 5.01 | 50814 | 10147 | 5.0 | |
| 0 | 20 | 0.0 | 20.03 | 46609 | 11077 | 4.21 | 47425 | 11298 | 4.2 | |
| 0 | 22 | 0.0 | 21.99 | 46603 | 10787 | 4.32 | 48407 | 11241 | 4.3 | |
| 0 | 26 | 0.0 | 25.98 | 46606 | 9838 | 4.74 | 48152 | 10164 | 4.7 | |
| 2 | 20 | 2.0 | 20.01 | 43530 | 10393 | 4.19 | 45651 | 10928 | 4.2 | |
| 2 | 22 | 2.0 | 21.94 | 43547 | 10100 | 4.31 | 46526 | 10819 | 4.3 | |
| 2 | 26 | 2.0 | 26.03 | 43439 | 9111 | 4.77 | 46059 | 9661 | 4.8 | |
| 7 | 20 | 7.0 | 20.10 | 35889 | 8124 | 4.42 | 38645 | 8793 | 4.4 | |
| 7 | 22 | 7.0 | 22.01 | 35885 | 7804 | 4.60 | 39254 | 8582 | 4.6 | |
| 7 | 26 | 7.0 | 26.30 | 35885 | 6878 | 5.22 | 38258 | 7332 | 5.2 | |
| 12 | 20 | 12.0 | 20.08 | 28062 | 5421 | 5.18 | 27966 | 5443 | 5.1 | |
| 12 | 22 | 12.0 | 21.99 | 28206 | 5144 | 5.48 | 28311 | 5199 | 5.4 | |
| 12 | 26 | 12.0 | 25.93 | 26784 | 4085 | 6.56 | 26784.2 | 4084.8 | 6.6 | |

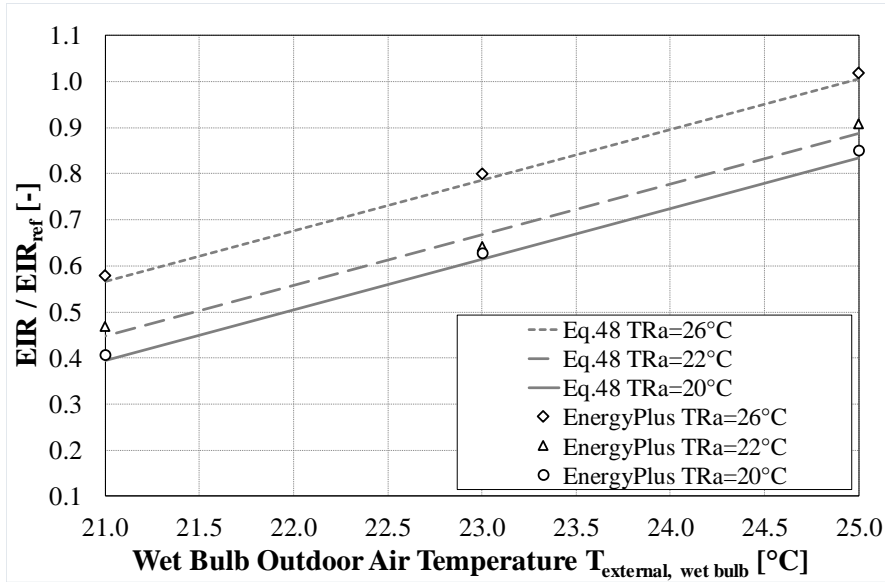


Figure 44: EIR in cooling mode: comparison between EnergyPlus simulations and Equation (48) with Table 25 coefficients

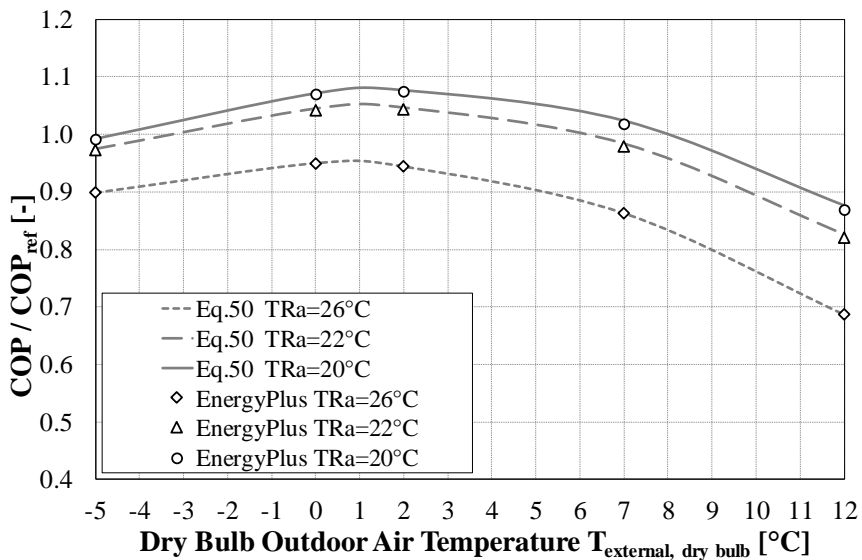


Figure 45: COP in heating mode: comparison between EnergyPlus simulations and Equation (50) with Table 25 coefficients

Different operating conditions have been simulated, namely the ones presented in

Table 28 and Table 29 for cooling and heating mode respectively. The results of EnergyPlus simulations are reported and compared with the data obtained with the implemented equation fit model. The agreement is very good, with an average relative error of almost 1.5% for the cooling capacity \dot{Q}_C , 1.6% for the EER , 5.1% for the heating capacity \dot{Q}_H and 0.26% for the COP . Figure 44 and Figure 45 show graphically the same comparison.

3.3.3.3. Implementation of the Fancoil model in EnergyPlus

The EnergyPlus object used to describe the fancoil unit is called "ZoneHVAC:FourPipeFanCoil". Even if the real units installed in the Smart Energy Building are working with a "2-pipes" configuration, the software model can be controlled to operate only one coil at a time. In this way, it is possible to operate the fancoils with the right coil configuration.

The software model is composed of different objects, namely a fan, a cooling coil (water fed), a heating coil (electricity or water fed). This simple assembly can be controlled differently, keeping constant or modifying the water or the air flow rates to change the heat flux, and consequently control the room air temperature.

In the SEB case, both the cooling and heating coil are operating with water and the control logic adopted is to keep constant the water flow rate and to modify the air flow.

3.3.4. Photovoltaic Field of the Smart Energy Building

This paragraph is devoted to the analysis of the Photovoltaic system placed on the rooftop of the Smart Energy Building. The paragraph is briefly covering the theoretical background of the photovoltaic effect, and some detailed information about the real photovoltaic field are given. Then it is described how it is possible to implement the PV field into the EnergyPlus model, describing it deeply. A dedicated section presents the electrical power model used to calculate the PV production as a function of different parameters (i.e. sun irradiance, cell temperature). The analysis was aimed to obtain a comparison between the real data measured by the sensor network, the simulation results, and theoretical calculations. To operate a homogeneous comparison, the weather file used for simulations has been manipulated using the software Elements, thus real data measured at the Savona Campus were used as inputs. The considered simulation periods for updating the weather file were January and June 2018. The measured quantities contained information about solar irradiance and the external air temperature. The comparison was carried out between values of electrical power produced, measured, calculated and simulated, using the PV cell temperature and the solar irradiance as inputs.

3.3.5. Photovoltaic Effect Theoretical Background

The working principle of a photovoltaic module is called *photovoltaic effect*, and it is both a chemical and a physical principle. It is linked to the photoelectric effect, according to which a metal struck by light can emit electrons. If the incident particle (a photon) carries enough energy to free the electrons from the valence band, then the electron will move to the conduction band. However, this effect alone is not sufficient to generate current, because if the freed electrons remain stationary, they slowly lose the acquired energy, producing electromagnetic radiation. To exploit the photoelectric effect is necessary to consider other aspects.

When manufacturing PV modules, a semiconductor material is used. Semiconductors exhibit an electronic structure with most of the electrons bonded in the valence band, and only a few are present in the conduction band. The two bands are separated by a well-defined threshold of energy, called *forbidden energy gap*, that is different for every material. For silicon, one of the most used materials to assembly PV modules, this gap between valence and conduction band is equal to 1.2 [eV].

The energy carried by a photon, E , is defined as:

$$E = \frac{\lambda}{h \cdot c} \quad (56)$$

where:

- λ is the wavelength of the considered radiation;
- h is the Plank constant, equal to $6.626 \cdot 10^{-34}$ [Js];
- c is the speed of light, equal to $299.792 \cdot 10^6$ [m/s];

For each radiation considered, the energy carried by the photons is defined. Considering sunlight, much of the radiation coming from the Sun to the Earth is constituted by photons carrying an amount of energy greater than the silicon bandgap energy. However, pure silicon is not suitable to produce electricity with this principle, because it possesses no driving force able to set in motion the electrons in the conduction band. Pure silicon is a tetravalent element, this means that every atom is bonded to other four silicon atoms through four valence electrons present in the external orbital. It is possible to alter this structure by inserting different impurities inside pure silicon (doping). Those impurities are atoms of specific materials, that possess a different number of electrons in the valence band. Thus, it is possible to alter the electronic equilibrium of the pure silicon, obtaining different doping effects with different materials. Commonly, one speaks about *n-doping* if fluorine (which is a pentavalent element) is used to add electrons to the valence band The *p-doping* is obtained when trivalent elements are used, like boronThe *p-n junction* is obtained when two volumes of *p-doped* silicon and *n-doped* silicon are joined together. The junction process does not produce an electrically charged material, because, on the average, the number of the excess negative electron (added by fluorine) and positive holes

(created by boron) is the same. However, on the junction interface, the positive charges tend to diffuse in the negatively charged zone, and vice versa. This disequilibrium generates an electrical field that naturally opposes to the movement of the charges, recalling them to the original region. This is called *drifting*, it reaches an equilibrium when the number of moving charges is counterbalanced by the number of recalled ones. The equilibrium state induces, in the proximity of the junction interface, a lack of positive and negative charge, in the so-called *space charge region*. This is, basically, the configuration of a diode, with the cathode constituted by the p-region, and the anode is made by the n-region.

When the junction is exposed to sunlight, the photons striking the doped silicon are producing couples of electrons-holes in the space charge region. The particles are forced to move in the p or n region by the electric field that is present at the interface of the junction, generating an electrical current. Figure 46 is graphically showing the functioning principle of the p-n junction.

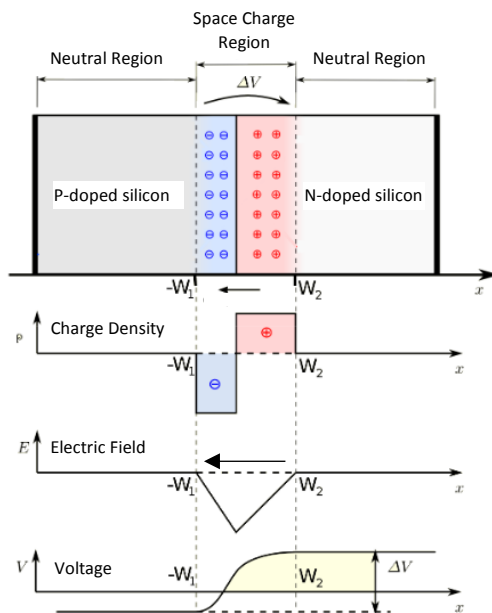


Figure 46: p-n junction and Space Charge Region [34]

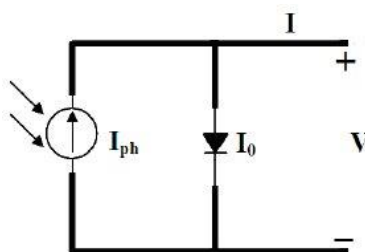


Figure 47: One diode equivalent circuit for an ideal PV cell [35]

The basic elements that can be connected electrically to obtain a PV module are called PV cells. It is possible to represent the equivalent circuit corresponding to an ideal photovoltaic cell, as in Figure 47.

With no load connected to the cell, there is no current flowing and the voltage produced is equal to the Open Circuit Voltage (V_{oc}). Otherwise, when the cell is short-circuited, the current flowing is the Short Circuit Current (I_{sc}) but no voltage is present.

The I-V characteristic of PV cells depends on the incident radiation and the cell temperature. Those quantities are constantly changing during time, therefore studying the I-V characteristic is a complicated task.

For this reason, standard test conditions (STC) are defined, to allow the manufacturers to provide “standard” PV performance. The STC are defined by a cell temperature equal to 25 [°C] and an irradiance value of 1000 [W/m²].

Considering the simple model presented in Figure 47 it is possible to express the Short Circuit Current (I_{sc}) and the Open Circuit Voltage (V_{oc}), using Equations (57) and (58), respectively.

$$I_{sc}(G, T) = \frac{G}{G_{stc}} [I_{sc,stc} + \mu_{I,sc}(T - T_{stc})] \quad (57)$$

$$V_{oc}(T) = V_{oc,stc} + \mu_{V,oc}(T - T_{stc}) \quad (58)$$

Where G [W/m²] and G_{stc} [W/m²] are the measured and the standard test condition irradiance, T [K] and T_{stc} [K] are the measured cell temperature and the cell temperature at standard test conditions, $I_{sc,stc}$ [A] is the short circuit current at the standard test conditions, $V_{oc,stc}$ is the open-circuit voltage at standard test conditions, $\mu_{I,sc}$ [A/°C] and $\mu_{V,oc}$ [V/°C] are the thermal degradation coefficient for the short circuit current and the open-circuit voltage.

These Equations constitute a simplified model, which neglects several important effects induced by power losses and contact characteristics within the cells. However, they can be useful to obtain the trend for current and voltage as a function of temperature. In general, increasing the temperature cell is detrimental for the PV energy conversion.

3.3.6. Smart Energy Building Photovoltaic Field

A photovoltaic field is installed on the roof of the Smart Energy Building, with a total peak power equal to 22 [kW]. The field is constituted by five strings, each composed of 17 modules, for a total of 85 PV modules. The manufacturer is Futura and the commercial name of the single element is FU250 P.

The manufacturer datasheet for the single module is shown in Table 30. The cells are constituted by polycrystalline silicon, and the main feature declared by the manufacturer is the linear degradation of the module efficiency, equal to 0.7 % per year.

The PV field is connected to a single inverter, brand Aros-solar model K33. The inverter is a very important device that allows to couple the PV field to the rest of the electrical grid. Since PV technology is still relatively expensive, it is important to maximize the power produced by the installed modules. The power produced by a PV field depends on the incident irradiation and the electrical characteristics (current and voltage) of the load connected to it. If the solar radiation changes in time, also the load electrical characteristics that allow obtaining the maximum power production have to change. The Maximum Power Point Tracking (MPPT) solves this problem because allows presenting to the PV field the best couple of I_{MPP} - V_{MPP} that maximize power production. Contemporarily, the inverter can reconvert the I-V couple to values that are suitable to power the load connected to the PV field, effectively coupling the PV field to the electrical load. Moreover, since the current produced by the PV field is direct current (DC), the inverter has also the task to convert the DC into alternate current (AC).

Table 30: FU 250 P PV single module datasheet

| | |
|---|-------------------------|
| Maximum Rated Power P_{max} | 250 [W] |
| Efficiency | 15.3 [%] |
| Open Circuit Voltage V_{oc} | 37.55 [V] |
| Short Circuit Current I_{sc} | 8.83 [A] |
| MPP Voltage V_{MPP} | 30.3 [V] |
| MPP Current I_{MPP} | 8.26 [A] |
| Maximum Inverse Current | 15 [A] |
| Temperature V_{oc} Attenuation Coefficient | -0.26 [%/°C] |
| Temperature I_{sc} Attenuation Coefficient | 0.06 [%/°C] |
| Temperature P_{max} Attenuation Coefficient | -0.36 [%/°C] |
| Nominal Operative Cell Temperature (NOCT) | 45 [°C] |
| Irradiance at NOCT | 800 [W/m ²] |

3.3.7. PV Module Models in EnergyPlus

In this paragraph, it will be analyzed how EnergyPlus calculates the incident solar radiation that can be used as input for the PV modules models. Moreover, the different EnergyPlus objects used to describe the PV field will be presented, giving information about the requested inputs and the considered outputs.

3.3.7.1. General EnergyPlus PV Modules Model

EnergyPlus contains three different “Generator:Photovoltaic” objects that can be used to model the performance of a PV module. In general, it is necessary to apply this type of object to an existing shading surface, reproducing the exact position and geometrical configuration of the real PV array installed. Figure 48 shows how the PV field has been drawn and integrated into the complete EnergyPlus model.

The models that can be used to describe the “Generator:Photovoltaic” are “Simple”, “Equivalent One Diode” and “Sandia”. Each one has its mathematical model and can produce different output variables, as well as requiring different input quantities.

For the present work, the “Equivalent One Diode” model has been chosen because it offers the best solution to the problem analyzed. In fact, the “Simple” model operates with fixed PV efficiency, neglecting the effect of the cell temperature and sun irradiance on the electricity production. Moreover, it was not possible to obtain the cell temperature as output of the simulations. The “Sandia” model was discarded because it is more focused on the electrical analysis of the PV array, which was not the main focus of this thesis. EnergyPlus is considering an irradiance threshold of $0.3 \text{ [W/m}^2\text{]}$ below which the PV panels are not operated, thus not producing any electrical power. Moreover, the electrical load connected to the PV field is assumed to operate always at the maximum power point (MPP).

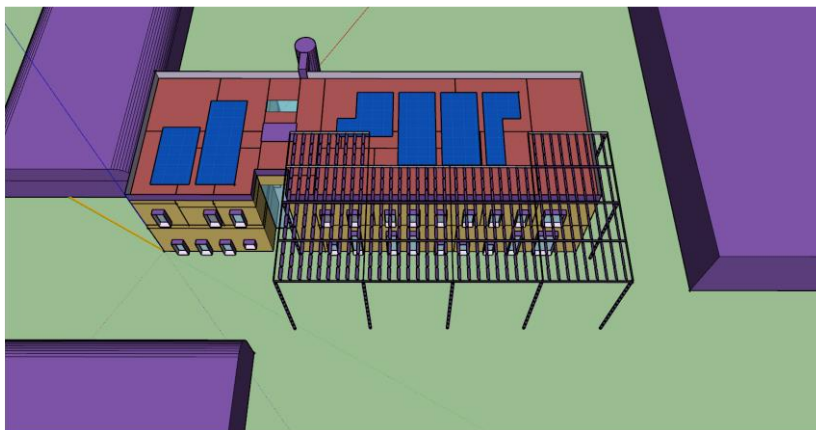


Figure 48: SketchUp model of the PV field installed on SEB rooftop

3.3.7.2. Equivalent One Diode Model

The “Equivalent One-Diode” model uses equations that are derived from an empirical equivalent circuit, which is described by Figure 49 where a series-connected resistance (R_s) is used to account for the voltage drop at the contact and through the layers of materials. Even if this equivalent circuit is equal to a single module, the software can model also the array of modules that constitutes the PV field. The intensity of the current produced is dependent on solar radiation while the I-V characteristics of the diode are both irradiance and temperature-dependent. The model can estimate different parameters using the manufacturers' data that have to be provided as inputs. Moreover, the model includes also an optional incidence angle modifier correlation to calculate the effects that are induced by the reflectance of the PV module, considering that it continuously changes with the solar incident angle.

The “One Diode Model” is based on the work by Eckstein [36] and it requires the estimation of four parameters that describe the equivalent circuit for the PV module.

The four parameters that are estimated by EnergyPlus are:

- $I_{L,STC}$ = photocurrent at standard test condition;
- $I_{0,STC}$ = diode reverse saturation current at standard test condition;
- R_s = series resistance;
- γ = empirical PV curve-fitting parameter.

Those parameters cannot be obtained by physical measurements, but they are calculated by EnergyPlus, based on the manufacturer’s datasheet.

When using the “One Diode” model, the IV curve is generated by EnergyPlus using as inputs the temperature, the solar irradiance and the four parameters listed above.

The expression describing the current-voltage curve for the equivalent circuit shown in Figure 49 is given by the Equation (59):

$$I = I_L - I_0 \left\{ \exp \left[\frac{e}{\gamma K T_c} (V + I \cdot R_s) \right] - 1 \right\} \quad (59)$$

where:

- e is the electron charge [C];
- K is the Boltzmann constant [J/K];
- T_c is the cell temperature [K];

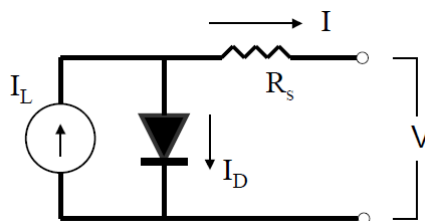


Figure 49: Equivalent One Diode model equivalent circuit for one PV module

I_L is the current generated by the incident radiation on the cell [A], while I_0 is the diode reverse saturation current [A]. They are given by Equation (60) and (61), where G and G_{stc} are, respectively, the global incident radiation on the cell [W/m^2] and the incident radiation at standard test condition ($1000 [W/m^2]$), $I_{L,stc}$ is the current generated by the cell at the standard test condition [A], $I_{0,stc}$ is the diode reverse saturation current at standard test condition [A] and $T_{c,stc}$ is the cell temperature at standard test condition ($25 [^{\circ}C]$).

$$I_L = I_{L,stc} \frac{G}{G_{stc}} \quad (60)$$

$$\frac{I_0}{I_{0,stc}} = \left(\frac{T_c}{T_{c,ref}} \right)^3 \quad (61)$$

In Equation (59) the PV current I appears on both sides, and the equation becomes implicit. For this reason, the equation roots can be found applying Newton's method. Moreover, since the maximum point tracking is required to correctly select the most suitable working conditions, an iterative search is applied to the IV curve, to find the maximum power current (I_{mpp}) and voltage (V_{mpp}) point.

The temperature at which the cell operates influences the cell performance because the electricity production lowers as the cell temperature rises.

EnergyPlus possesses different models dedicated to calculating the cell operating temperature:

- Decoupled NOCT Conditions;
- Decoupled Ulleberg Dynamic;
- Integrated Surface Outside Face;
- Integrated Transpired Collector;
- Integrated Exterior Vented Cavity;

For the present thesis, the Decoupled NOCT Conditions model has been chosen and applied. This model is based on the method proposed by Duffie and Beckman [37], which accounts for the Normal Operating Cell Temperature.

With this method, the cell temperature (T_c) is evaluated under the following assumptions:

- Wind speed of $1 [m/s]$;
- No electrical load;
- Specified values for reference irradiance $G_{T,NOCT}$ ($800 [W/m^2]$) and ambient temperature T_a ($25 [^{\circ}C]$).

Thus, the Equation that is used by EnergyPlus to compute the cell temperature is:

$$T_c = T_a + \frac{1 - \eta_c / \tau \alpha}{G_{T,NOCT} \cdot \tau \alpha / U_L} \quad (62)$$

- T_c is the cell temperature [$^{\circ}C$];
- T_a is the ambient temperature [$^{\circ}C$];
- η_c is the conversion efficiency of the module, depending on T_a [-];

- $G_{T,NOCT}$ is the total radiation incident on the module at Normal Operating Conditions [W/m^2];
- $\tau\alpha$ is the module transmittance-absorptance product [-];
- U_L is the array thermal loss coefficient [W/m^2K];

Figure 50 shows the EnergyPlus parameters input window with the corresponding value assigned for the “Equivalent One Diode” model.

| Field | Units | Obj1 |
|---|---------------|--------------------|
| Name | | PV_SEB |
| Cell type | | CrystallineSilicon |
| Number of Cells in Series | dimensionless | 55 |
| Active Area | m2 | 1.46 |
| Transmittance Absorptance Product | dimensionless | 0.95 |
| Semiconductor Bandgap | eV | 1.2 |
| Shunt Resistance | ohms | 1000000 |
| Short Circuit Current | A | 8.83 |
| Open Circuit Voltage | V | 37.55 |
| Reference Temperature | C | 25 |
| Reference Insolation | W/m2 | 1000 |
| Module Current at Maximum Power | A | 8.26 |
| Module Voltage at Maximum Power | V | 30.3 |
| Temperature Coefficient of Short Circuit Current | A/K | 0.005298 |
| Temperature Coefficient of Open Circuit Voltage | V/K | -0.09763 |
| Nominal Operating Cell Temperature Test Ambient Tem | C | 25 |
| Nominal Operating Cell Temperature Test Cell Temperat | C | 45 |
| Nominal Operating Cell Temperature Test Insolation | W/m2 | 800 |
| Module Heat Loss Coefficient | W/m2-K | 40 |
| Total Heat Capacity | J/m2-K | 50000 |

Figure 50: EnergyPlus input window for "Equivalent OneDiode" PV model

3.3.7.3. Power Production Models

For this work, the field power production is calculated starting from irradiance and cell temperature values, and the obtained results are compared with the output value from EnergyPlus. For the calculation, two different models are used.

The first (referred to as the MPP method) is based on the assumption that the module is always working at the Maximum Power Point (MPP), and the electrical power is calculated using Equation (63):

$$P_{MPP} = V_{MPP} \cdot I_{MPP} \quad (63)$$

Being V_{MPP} and I_{MPP} the MPP voltage and current, given by applying Equation (57) and (58) when MPP conditions are considered. V_{MPP} and I_{MPP} are expressed by Equation (64) and (65) respectively:

$$I_{MPP} = \frac{G_T}{G_{stc}} \cdot [I_{MPP,stc} + \mu_{I,sc}(T_c - T_{stc})] \quad (64)$$

$$V_{MPP} = V_{MPP,stc} + \mu_{V,oc}(T_c - T_{stc}) \quad (65)$$

where:

- G_T is the total solar irradiance [W/m^2];
- G_{stc} is the total solar irradiance at standard test conditions ($1000 [\text{W}/\text{m}^2]$);
- $I_{MPP,stc}$ is the MPP current at standard test conditions [A];
- $V_{MPP,stc}$ is the MPP voltage at standard test conditions [V];
- $\mu_{I,sc}$ is the short circuit current temperature-attenuation factor [$\text{A}/^\circ\text{C}$];
- $\mu_{V,oc}$ is the open-circuit voltage temperature-attenuation factor [$\text{V}/^\circ\text{C}$];
- T_c is the cell temperature [$^\circ\text{C}$];
- T_{stc} is the cell temperature at standard test conditions ($25 [^\circ\text{C}]$);

The second method, referred to as the “Efficiency Method”, is given by Equation (66):

$$P_\eta = A_a \cdot G_T \cdot \eta_{module}(T) \quad (66)$$

where

- A_a is the net active module area [m^2],
- G_T is the total irradiance incident on the module [W/m^2]
- $\eta_{module}(T)$ is the module efficiency is given as a function of temperature [-];

The module efficiency $\eta_{module}(T)$ can be calculated using the expression given by Equation (67):

$$\eta_{module}(T) = \eta_{module}(T_{stc}) \cdot [100 - \mu_p(T_c - T_{stc})] \quad (67)$$

where:

- $\eta_{module}(T_{stc})$ is the module efficiency at standard test conditions [-];
- μ_p is the electrical power temperature-attenuation coefficient [W/°C];
- T_c is the cell temperature [°C];
- T_{stc} is the cell temperature at standard test conditions [°C];

3.4. Model Validation

This paragraph is dedicated to present the validation procedure using the measured values acquired by the SEB sensor network. Unfortunately, given the lack of recorded data for part of the ventilation system, and the aggregation of the electrical consumption data at floor level, the validation procedure focused mainly on the PV field. Then, it is shown also how, starting from the electrical power measured after the conversion operated by the inverter, it was possible to calculate the effective electrical power produced by the PV field, accounting for the calculated inverter efficiency.

The wide sensor network installed at the Smart Energy Building is controlled by a dedicated software (DESIGO) which is able not only to record in real-time all the variables measured by the sensors (both thermal quantities and electrical ones) but it can store them in a large database that contains historical data series. In particular, the SEB acquisition system contains information about mass flow rates for the geothermal pump, temperatures of water and air (system plants and building), sun irradiance, human presence inside rooms, electrical power, current and voltage produced by PV field, electrical power requested by the building (aggregated at floor level), and many others. Moreover, through the DESIGO interface, it is possible to set the operative conditions of certain plant components (i.e. temperature setpoints) or to check the presence of failures.



Figure 51: DESIGO page for the AHU monitoring

Unfortunately, the main parameters for the air handling unit (air mass flow rates, temperature and humidity ratio) are only available in real-time, with no record and storage of data. This means that no long-time data series are available. Although the lack of data recording, it was possible to verify that the air handling unit works at constant temperature and humidity ratio, providing the ventilation required to fulfill the Italian Normative standards. That information has been used to properly model the AHU operation and performance as shown in Paragraph 3.3.2.2. Figure 51 shows an example of the DESIGO interface for the AHU system.

In a future work perspective, some sets of measures have been acquired and processed, to already verify consistency among the stored datasets. As an example, Figure 52 shows the electrical power data, measured at the 1st-floor electrical panel. The measures contain information about the requested power for lighting and plug loads during the period from 8th January to 8th February 2019.

Figure 52 and Figure 53 show an example of the available acquired data series by the sensor network present at the Smart Energy Building. Figure 52 shows the example data acquired to monitor the Electrical Power measured at the electrical cabinet connected to the 1st floor, while Figure 53 reports the GHE temperatures for inlet and outlet. The sensors are different, the average value refers to the main inlet and outlet pipes, while the HC sensors monitor the temperature of a single bore-hole.

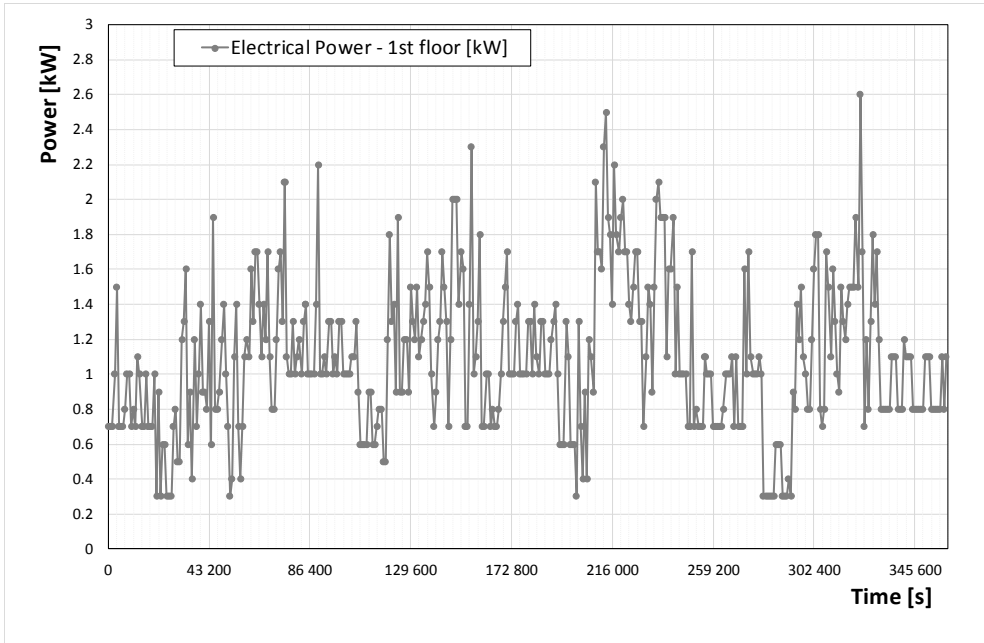


Figure 52: Electrical Power aggregated at floor level, for the 1st floor (8th January - 8th February 2019)

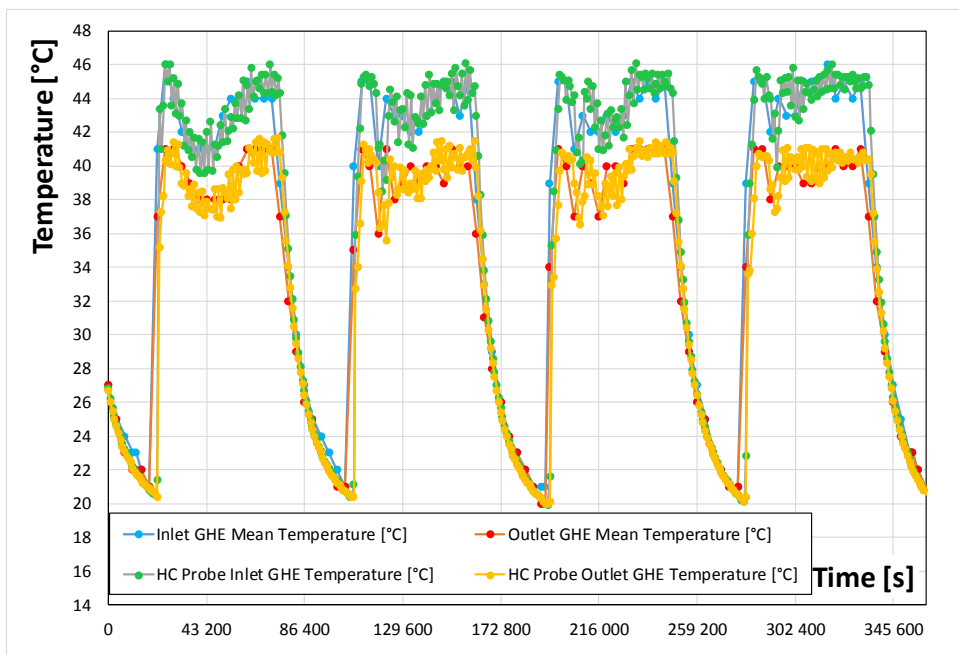


Figure 53: Inlet and Outlet Temperatures [°C] for the GHE

3.4.1.1. Inverter Efficiency Calculation

The power produced by the PV field is not constant in time and, consequently, the inverter efficiency is not constant too. Moreover, the measured values of the electrical power (P_{meas}) are acquired downstream. Thus, it is necessary to account for the inverter efficiency to obtain the power produced by the PV field ($P_{field,meas}$).

Equation (68) shows the relation that links P_{meas} and $P_{field,meas}$.

$$P_{field,meas} = P_{meas} / \eta_{inverter} \quad (68)$$

The inverter efficiency ($\eta_{inverter}$) is a function of the electrical load, so it is necessary to calculate it for every measured value P_{meas} .

Unfortunately, the datasheet available for the inverter (brand Aros-solar model K33) only gives the maximum efficiency (equal to 0.95).

Starting from data of a typical inverter efficiency-partial load (P/P_{max}) behavior, it was possible to interpolate them to obtain the curve expression (Figure 54). In the analyzed case, the best fit can be given by Equation (69) (obtained employing Curve Expert software.)

$$\eta_{inverter} = a \cdot b \left(\frac{P}{P_{max}} \right) \cdot \left(\frac{P}{P_{max}} \right)^c \quad (69)$$

The next step is to calculate the actual partial load using the measured value (P_{meas}/P_{max}) and to use this value to calculate the actual inverter efficiency applying Equation (69). In this way, it is possible to obtain the inverter efficiency for every measured value of the data series for the PV electrical power production.

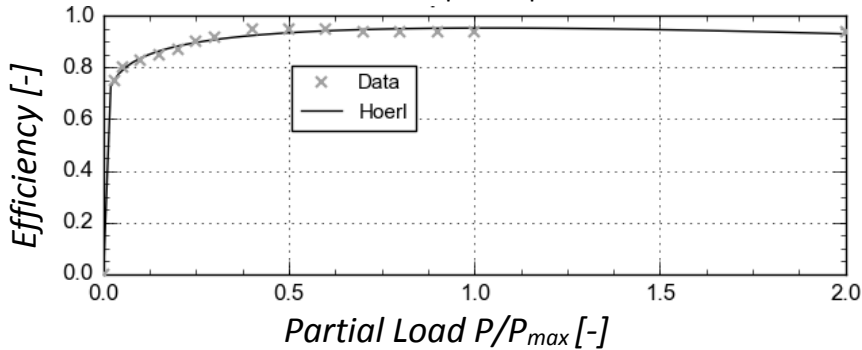


Figure 54: Efficiency vs partial load curve for typical inverter

3.4.1.2. Weather File Enhancing with Measured Climatic Parameters

For this thesis, for the comparison among real measured data, simulation results and theoretical calculations, it was necessary to modify the EPW file. In particular, the “standard” weather file has been converted into the “actual” weather file, related to the climate conditions corresponding to the period during which the SEB measurements have been realized. An additional software, called Elements, has been used. Elements is a very powerful software that allows manipulating the input weather file, adding or removing information or simply modifying the existent quantities. The most important feature is that it can ensure certain correlations between quantities (like dew-point temperature and air humidity, or diffuse and direct solar radiation with respect to the total irradiance).

For the analyzed case, Elements has been used to insert in the Savona weather file the irradiance and the outdoor air temperature values registered by the sensor network present at the Savona Campus, during the same period as for the PV power production measurements.

Considering the solar irradiance, the weather file has been modified to have the global horizontal irradiance value equal to the measured quantity. The horizontal global solar radiation is composed of different contribution like shown in Equation (70):

$$G_{(tot,hor)} = G_{direct,normal} \cdot \cos(z) + G_{diffuse,horizontal} \quad (70)$$

with z being the zenith angle for the selected location.

As a consequence, the measured values of global radiation on horizontal surface have to be decomposed in the two components $G_{direct,normal}$ and $G_{diffuse,horizontal}$ to correctly input all the values needed by the weather file.

The first step is to calculate the ratio between diffused and direct radiation with respect to the global one. The Standard UNI10349 provides the global, direct and diffuse irradiance (daily value, obtained as a monthly average) on a horizontal surface for Savona (Table 31).

The average ratio between diffused and global irradiance has been calculated as:

$$\left(\frac{E_{dif}}{E_{tot}}\right)_{avg} = \frac{\sum_{n=1}^{12} E_{dif,n}}{\sum_{n=1}^{12} E_{tot,n}} \quad (71)$$

This average ratio results equal to 0.39, thus, the horizontal direct solar radiation is 61% of the horizontal total value.

In this way, it is possible to calculate the share of diffused and direct horizontal radiation using Equation (72) and (73) respectively.

$$G_{diffuse,horizontal} = \left(\frac{E_{dif}}{E_{tot}}\right)_{avg} \cdot G_{total,horizontal} \quad (72)$$

$$G_{direct,horizontal} = \left[1 - \left(\frac{E_{dif}}{E_{tot}}\right)_{avg}\right] \cdot G_{total,horizontal} \quad (73)$$

To apply Equation (70) it is still necessary to calculate $G_{direct,normal}$. This quantity can be correctly computed considering Equation (74):

$$G_{direct,normal} = G_{direct,horizontal} / \cos(z) \quad (74)$$

It is still necessary to consider that, since the measured values already account for the possible cloud coverage, the cloud cover index in the modified weather file must be set equal to zero.

3.5. PV field Model Validation

The validation of the model was possible thanks to the measured values acquired by the sensor network installed at the SEB building, and it focuses more on the Photovoltaic field performances and power production. The SEB is equipped with two different software dedicated to the monitoring: DESIGO and SCADA. DESIGO is mainly used for acquiring, processing and storing data from thermal measures (for instance temperatures, heat fluxes, mass flow rates, power) while SCADA is extensively used to collect and analyze electrical quantities (i.e. voltage, current, electrical power, frequency). For the validation process, the data used come from both systems, considering:

- PV module temperature;
- Global horizontal irradiance;
- The electrical power produced by the PV field;

The considered periods for the analysis are January 2018 and June 2018

| | E_{tot} | E_{dif} | E_{dif}/E_{tot} |
|--------------|-------------------------|-------------------------|-------------------|
| Month | [kJ/m ² day] | [kJ/m ² day] | [-] |
| Jan | 5500 | 2 600 | 0.47 |
| Feb | 8300 | 3 600 | 0.43 |
| Mar | 12500 | 5 100 | 0.41 |
| Apr | 16600 | 6 700 | 0.40 |
| May | 19600 | 7 900 | 0.40 |
| June | 21200 | 8 400 | 0.40 |
| July | 23700 | 7 600 | 0.32 |
| Aug | 19400 | 6 900 | 0.36 |
| Sept | 15100 | 5 500 | 0.36 |
| Oct | 10300 | 4 000 | 0.39 |
| Nov | 6200 | 2 800 | 0.45 |
| Dec | 5000 | 2 300 | 0.46 |
| Total | 163400 | 63 400 | 0.39 |

Table 31: UNI 10349 monthly averaged daily value for direct and diffused irradiance (on horizontal surface) in Savona City

3.5.1.1. Solar Irradiance Analysis

The first comparison between measurements and simulations is related to solar irradiance. More specifically, the measured global solar irradiance on horizontal surface is compared with the global solar irradiance calculated by EnergyPlus on a horizontal surface of the roof (Figure 55 and Figure 56). The irradiance values come from a weather station installed in Savona, and they have been shared by courtesy of the CIMA foundation.

The horizontal surface selected is subjected to a shading effect similar to the neighbouring PV modules.

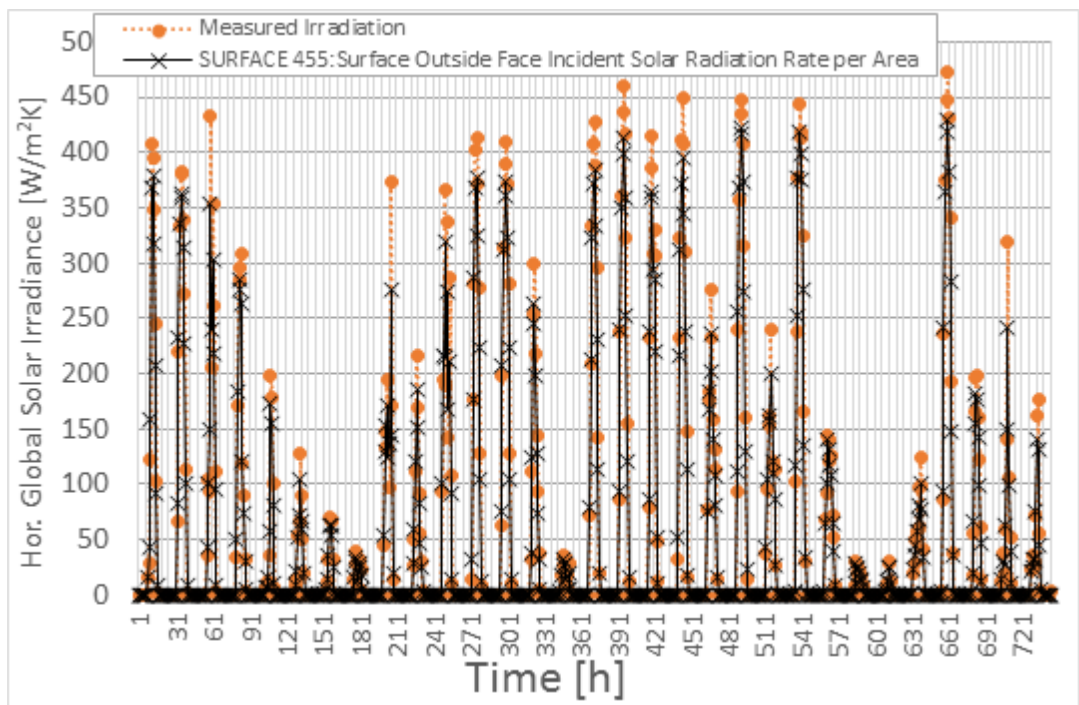


Figure 55: Measured Irradiance vs Simulated Irradiance (on horizontal surface) for January

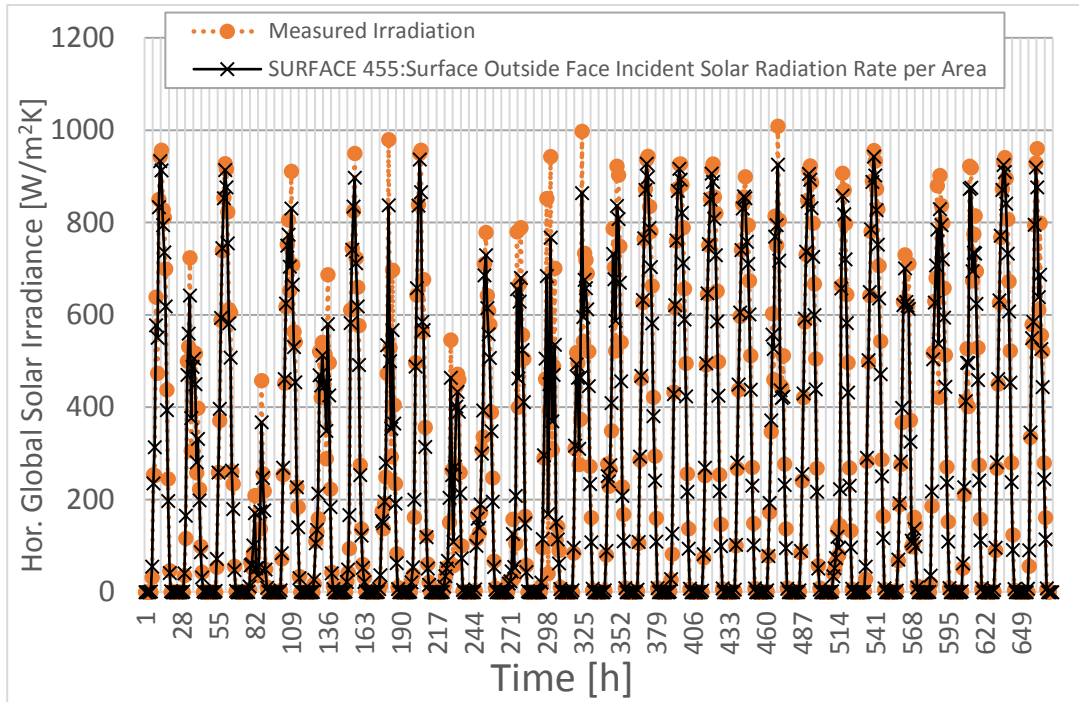


Figure 56: Measured Irradiance vs Simulated Irradiance (on horizontal surface) for June

Overall, for both January and June, the irradiance obtained as output from the simulation is always below or equal to the measured value. This can be explained by the presence of the shades cast by the surrounding building structures (like the steel sunblind or the railings surrounding the roof). Moreover, in June, the difference is minor, and this is linked to the sun position in the sky. During summer, the solar zenith angle is higher, thus the surrounding objects are casting shorter shadows. The shading phenomenon can be visually checked also using Sketchup to inspect the three-dimensional model as shown in Figure 57.

3.5.1.2. Module Temperature Validation

The next comparison is related to the cell temperature that is extremely important since it influences the PV module efficiency. Figure 58 and Figure 59 show the results of the comparison. The selected model in EnergyPlus is the “DECOUPLED: Generator PV” which produces as output the PV cell temperature.

For January, the simulation results are in quite good agreement with the measured values with the major discrepancies around peak values. For June, the agreement between the simulation results and the measurements is unsatisfactory. The simulated module temperature is higher than the measured one, with particular discrepancy for peak values.

It is not clear if this disagreement is due to an unsuitable choice of simulation parameters or measurement uncertainties. The latter appears as the most probable reason because, looking at maximum values reached by the measured module temperature, it appears as unconvincing to reach only 44 [°C] with global incident radiation around 1000 [W/m²].

Further investigations are necessary to clarify this point. In the next future, a measurement campaign for temperature and irradiance will be realized directly on the SEB roof, with an InfraRed (IR) gun and a pyranometer, respectively. The measured data will be compared against the DESIGO data, to identify the cause of the problem.

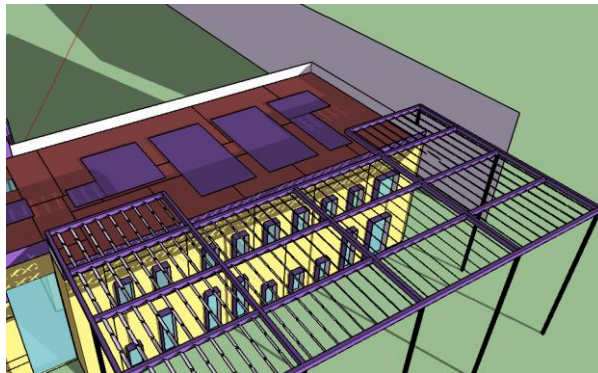


Figure 57: Example of Shading Effect on PV Modules for January

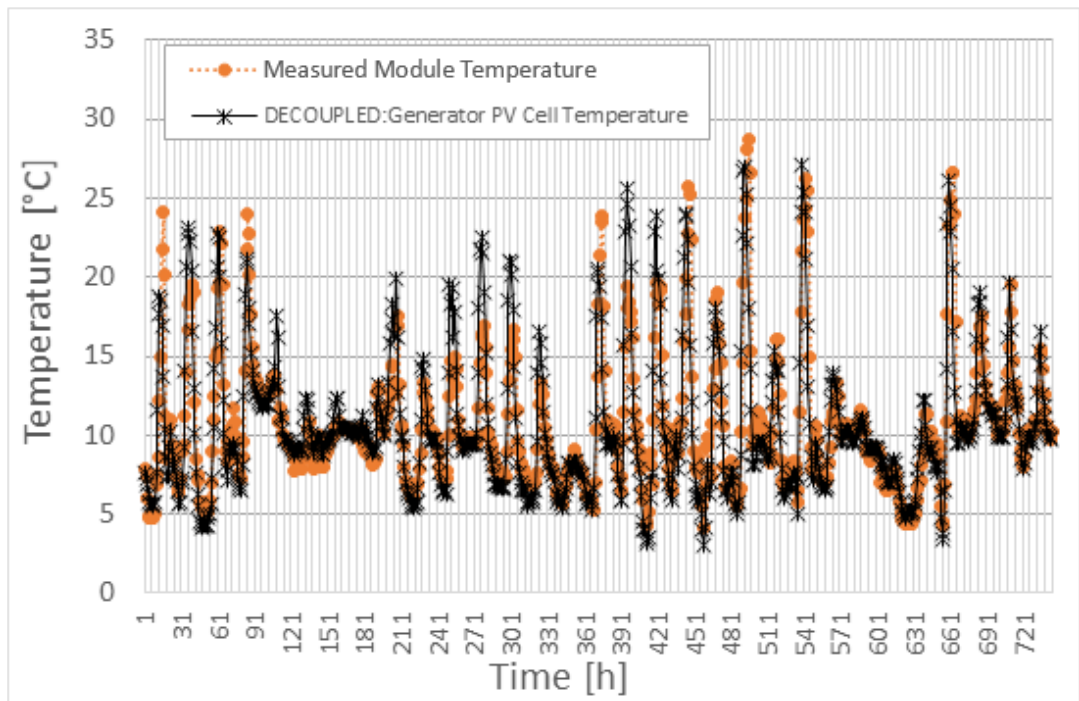


Figure 58: Measured Module Temperature vs Simulated Module Temperature for January

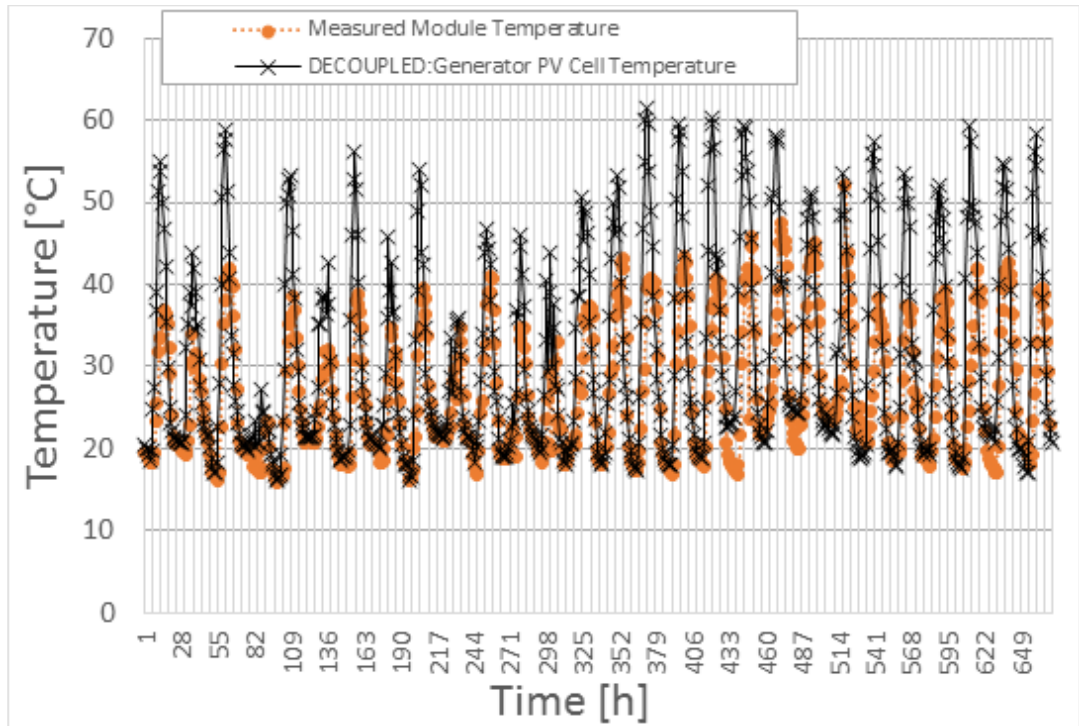


Figure 59: Measured Module Temperature vs Simulated Module Temperature for June

3.5.1.3. Electrical Power Production Validation

The last comparison is on the electrical power produced by the PV field. The available measures, modified with Equation (68), to eliminate the influence of the inverter efficiency, are compared with the electrical power calculated with Equation (63) and Equation (66) using the simulated cell temperature and the simulated total incident irradiance on the module.

Figure 60 reports the comparison results for January. Unfortunately, the acquisition system does not record any value for the first two weeks of the month. Moreover, the power values calculated (applying Equation (63) and Equation (66)) are always higher than the acquired data, especially considering the peak values. Furthermore, considering only the simulation results, the “MPP” method is producing results always greater than the “module efficiency” method, probably because the MPP assumes that the module always works at the Maximum Power Conditions.

The same comparison is carried out for June and the results are shown in Figure 61. The analysis of Figure 61 shows that, in general, there is a better agreement between measured and simulation results, with respect to the comparison proposed for January (Figure 60). The calculated electrical power using the “MPP” method is higher than the measured data and, again, the major discrepancies are at the peaks. This could be

explained by thinking that the Maximum Power Point operating conditions represent for definition the limiting upper condition. Analysing the results obtained applying the “Efficiency” method, the agreement with measured values is quite good, with the measured values being always equal to or smaller than the calculated ones.

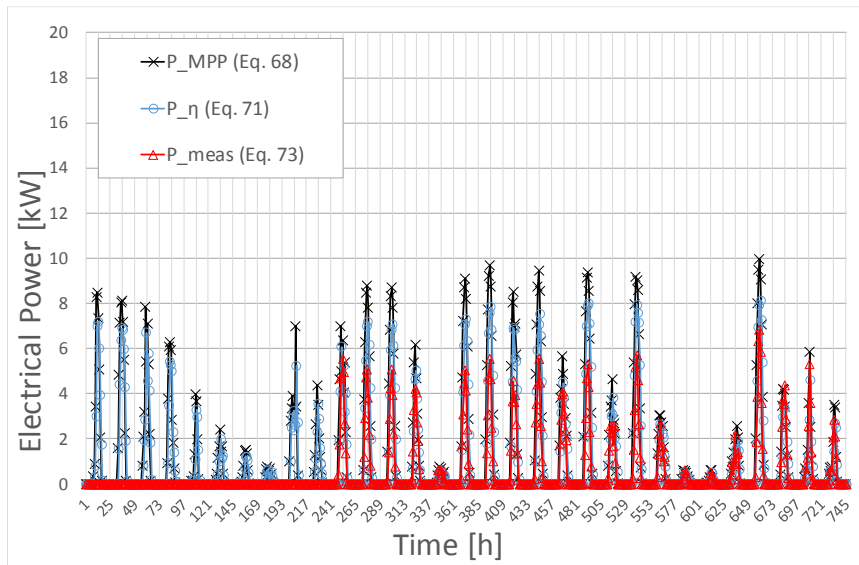


Figure 60: Electrical power comparison between measured data (modified with inverter efficiency) and electrical power calculated with module temperature and total irradiation simulated, for January

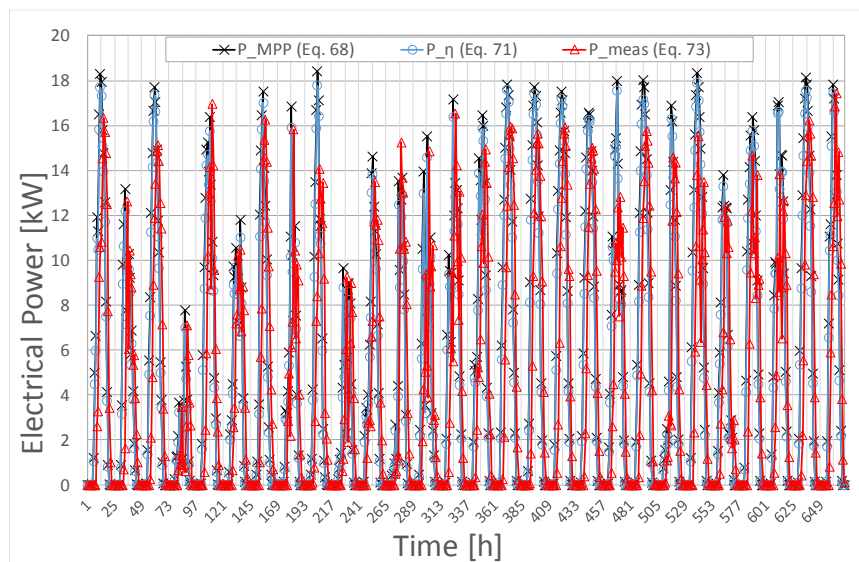


Figure 61: Electrical power comparison between measured data (modified with inverter efficiency) and electrical power calculated with the MPP method-Equation (70), for June

A further comparison can be carried out considering the module efficiency, calculated using Equation (65) applied to both the simulated data and the measured ones. Figure 62 and Figure 63 show graphically the results of this comparison. The module efficiency calculated shows very good agreement in both the analyzed cases (January and July) with the two curves exhibiting the same trend and almost identical values.

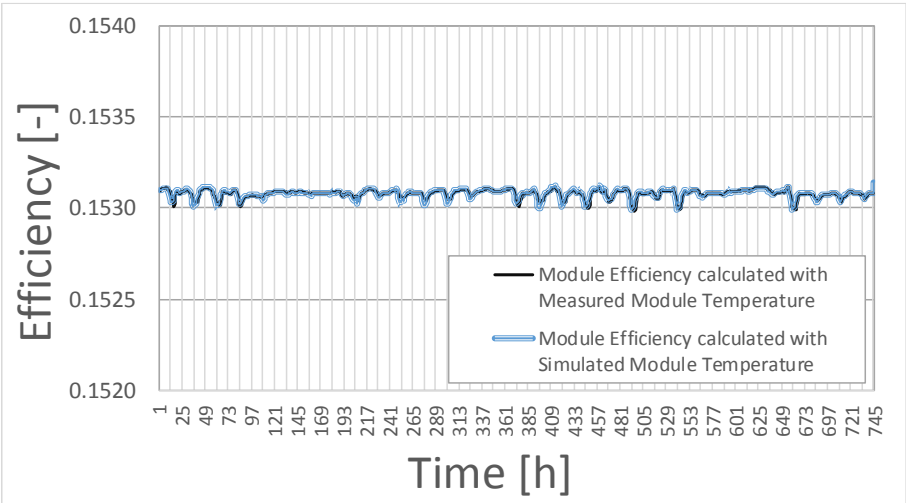


Figure 62: Module efficiency calculated applying Equation (72) to measured and simulated Module Temperature (January)

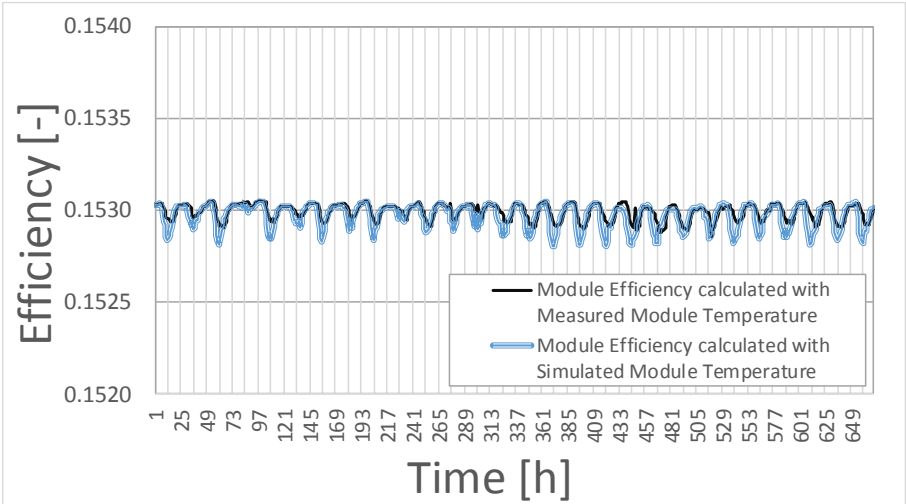


Figure 63: Module efficiency calculated applying Equation (72) to measured and simulated Module Temperature (June)

4. Conclusions and Final Remarks

The aim of the present thesis is to present the research activity developed during Ph.D. studies. The main issues are related to the analysis of new technologies associated with renewable energy sources (as geothermal energy) and devoted to reducing the energy consumption in buildings (Nearly Zero Emission Buildings).

The first activity deals with the modeling of heat exchangers into the ground to be coupled with heat pumps (Ground Coupled Heat Pumps, GCHP). In particular, a new semi-analytical method called Multiple Point Source - MPS - method has been proposed. The method, based on the superposition in space of the Single Point Source solution, is useful to generate the Ground Thermal Response Factor especially for innovative ground heat exchangers shape, like geopiles or helix ground heat exchangers.

The second topic is the development of a model in EnergyPlus environment for the dynamic energy simulation of a real Zero Emission Building (the Smart Energy Building - SEB - at the Savona Campus). Particular attention has been devoted to the analysis of the technological solutions of the SEB, specifically the two heat pumps (a water-to-water geothermal heat pump and an air-to-air heat pump with energy recovery) and the photovoltaic field on the SEB rooftop.

4.1. MPS Method Conclusions

Ground heat exchangers can be profitably coupled with heat pumps, for either heating or cooling buildings. Recently, to overcome the high cost related to the bore drilling, the heat exchangers start to be integrated into building foundation piles. This new arrangement, commonly called energy piles, reduces the drilling costs but on the other hand, given the particular shape of the pipe arrangement (helix or vertical U-pipes), needs the development of new methods to obtain the ground heat transfer function. Recently, different analytical solutions have been proposed to deal with some particular layout of the ground heat exchangers. While holding very precise results, the application of these solutions is difficult due to the strict mathematical formulation of the solutions themselves. Moreover, the specific solution is true only for the heat exchanger shape from which was derived. This means that changing the heat exchanger layout implies the need for applying a different solution, an operation that can be time-consuming.

The innovative MPS superposition method, proposed in this part of the thesis, is based on the superposition in space of the Single Point Source analytical solution. The model can be used to simulate any pipe arrangement, thus offering great flexibility able to deal with most energy pile heat exchanger configuration. In the thesis, great care was used to analyze in detail the discretization effect on the results of the model application. The influence of the discretization parameter $\Delta s/r_b$ has been discussed: considering different mesh discretization (for both a finite line source and finite stacked ring source models), the average error between different solutions have been calculated. For the finite ring source,

a discretization parameter $\Delta s/r_b = 2$ is the best compromise, allowing to balance the accuracy of the solutions and the computational time.

After the mesh discretization analysis, the method has been extensively validated against different analytical solutions proposed in literature: Finite Solid Cylindrical source and Finite Ring source. Calculating the average error between the different results shown that the solutions are in very good agreement (the error is 2.8% and 1.8% respectively). The validation process also involved the comparison of the ground thermal response factor calculated using the MPS method, with the results of a FEM simulation of a finite rings heat exchanger, using Comsol. In this case, the average error calculated was 2.5%, which is comparable to the previous validations.

Finally, in order to show the flexibility of the MPS method, the ground heat transfer function is calculated for a heat exchanger modeled as a series of vertically stacked rings or as a series of vertical pipes connected at the end by U-bends, maintaining constant the total length of the different heat exchanger configuration.

In future work, it could be possible to investigate the effect of another important parameter, i.e. the helix pitch effect, through a sensitivity analysis of the model with respect to this geometrical parameter.

4.2. Smart Energy Building Ideal Loads Calculation Conclusions

This part of the work was devoted to the calculation of the energy needs for the Smart Energy Building, using EnergyPlus and its Ideal Loads option. The calculated energy needs are the cooling and heating loads required by the building during the year, to maintain the comfort conditions (internal air temperature and humidity).

Analyzing the results obtained, the first consideration concerns the aggregated monthly loads for the whole building. During summer months, there is also a small request for heating, and this can be ascribed to the reheating process needed after the cooling one that decreases the air temperature below the dew point to remove the excess humidity from the supply air. The same process explains the need for cooling power, during winter months. Given that, during winter, the external air has high relative humidity, part of this moisture needs to be removed, lowering the temperature of inlet air.

Also the thermal comfort conditions inside each room have been analyzed and in particular: the outdoor and indoor air temperature, the indoor air temperature set point and indoor relative humidity. This analysis was carried out for two selected thermal zones, namely the Gym and the Office 3. The choice of these thermal zones was mainly driven by the difference in terms of internal gains between them. Moreover, for the sake of brevity, the analysis was focused on two weeks (9th to 15th January, and 1st to 7th July).

Overall, the thermal conditions for the considered zones are maintained within the desired range of values, both during summer and winter months. For a deeper analysis, also the cooling and heating loads have been investigated, both for the Gym and the Office

3 thermal zones. This analysis confirmed that the difference in internal gains (Office has high plug loads and solar gains with low occupancy level, while the Gym has high occupancy as well as high activity level, but low plug loads) induces meaningful differences for the heating and cooling loads. In particular, the Gym requires cooling energy also during winter, to effectively remove the high latent heat produced by the occupants' activity. This is reflected also during summer, when the Gym requests heating power to raise the supply air temperature after the moisture removal. On the other hand, the Office shows a more standard energy request, with almost no need for cooling during winter and very small amounts of heating during summer. Considering the ventilation, the minimum values requested by the law in force are always maintained.

4.3. Smart Energy Building Heat Pumps Analysis Conclusions

This work aimed to provide a series of insights to EnergyPlus users when simulations are carried out considering the operating temperature effects on the performance of heat pumps, chillers and even heat recovery heat pumps in ventilation circuits. The starting point was to refer to the equipment related to a recent near-zero energy building at the Author's University (the SEB at the Savona Campus). In particular, the final goal was to properly model the dependence of heat pumps performance on the temperature, both load and source side and eventually on the partial load operating conditions. The installed water-to-water and air-to-air heat pumps have been considered and the equation fit model has been implemented with a series of modifications for adapting it to the typical data available from the manufacturer.

Coefficients needed in the equation fit models have been determined utilizing an optimum search and, to validate the approach, a simplified building model equipped with the selected heat pumps and chiller has been created. The simplified model was created to operate the heat pumps at given nearly constant working temperatures.

For the air-to-air heat pump, the results from the simulations confirmed the expected results in terms of heating and cooling equipment performance, even if small differences (within 7%) resulted from the comparison between simulation trends and equation fit model input data.

For the water-to-water heat pump, also the influence of the water flow rates has been considered, deriving it from the manufacturer data related to the Partial Load Factor (PLF). The same analysis approach used for the air source HP has been used, comparing the simulation results with manufacturer data. The relative error slightly increases (within 15%) if the partial load operating conditions are considered (PLF = 0.67, 0.33) when comparing the manufacturer's data with the model equations.

4.4. Smart Energy Building Photovoltaic Field Analysis Conclusions

Photovoltaic energy conversion is a great resource that can be applied widely to reduce dependence from non-renewable sources of energy. Unfortunately, this technology is still quite expensive, thus it is very important to maximize energy production during the plant lifetime. One of the main factors that lower the performance of a PV module is the temperature of the module itself: the higher the temperature the lower the efficiency. For this reason, when developing building models used for dynamic energy simulation, it is of paramount importance to account for the variable efficiency of the modules.

In the thesis, the PV analysis was focused on studying the effect of the module temperature on electrical energy production, with a comparison with real measurements taken in January and June 2018 at the SEB PV field. The measures acquired by the sensor network installed at the Smart Energy Building are related to outdoor air temperature, horizontal solar irradiance, PV module surface temperature, and electrical power production.

The model selected and implemented in the building model for the PV module is the “Equivalent One Diode” model. The input weather file has been modified, to replicate the measured conditions, for both the outdoor air temperature and solar irradiance. Once the parameters of the real modules have been included in the model, the variable efficiency of the inverter has been assessed. This was necessary because the electrical power measurements are taken after the inverter, while the model does not account for it. The measurements and the simulation results have been compared also with values of the electrical power production calculated applying two different methods, namely the “MPP” method and the “Efficiency” method.

The comparison between the simulated and measured values of the electrical power production (modified to eliminate the influence of the inverter) and the cell temperature showed that, especially during January, the overall trend match is very good, while there are some major discrepancies at the peak values. The reason is still unclear a measurement campaign will be organized, to acquire in real-time sun irradiance, air temperature, and PV module temperature at SEB location. The measured values will be compared with the same quantities acquired by the sensor network, to correctly assess the reliability of the acquired measures.

Bibliography

- [1] European Commission, *Eu Energy in figures*, Bruxelles, 2019.
- [2] M. Ringel, R. Laidi and D. Djenouri, "Multiple Benefits through Smart Home Energy Management Solutions - A Simulation-Based Case Study of a Single-Family-House in Algeria and Germany," vol. 12, 2019.
- [3] *Directive 2010/31/EU of the European Parliament and of the Council on the energy performance of buildings*, 18/06/2010.
- [4] Adeguamento linee guida nazionali per la certificazione energetica degli edifici, Decreto interministeriale 26 giugno 2015, 2015.
- [5] T. P, P. S, D. M and C. D, *Zero Energy Buildings: A Critical Look at the Definition*, vol. 3, US: National Renewable Energy Laboratory and Department of Energy, 2006, pp. 417-428.
- [6] Z. Zheng, W. Lixiong and H. Nyuk, *Intelligent Control System Integration and Optimization for Zero Energy Buildings to Mitigate Urban Heat Island*, 2016.
- [7] P. D, *Geothermal energy and heat storage*, Canobbio: SUPSI – DCT – LEEE Scuola Universitaria Professionale della Svizzera Italiana Dipartimento Costruzioni e Territorio Laboratorio di Energia, Ecologia ed Economia, 2002.
- [8] B. Sanner, "Summary of EGC 2019 Country Update Reports on Geothermal Energy in Europe," in *European Geothermal Congress*, The Netherlands, 2019.
- [9] L. X, P. Y, Q. D and M. J, "An Analysis on Cost Reduction Potential of Vertical Bore Ground Heat Exchangers Used for Ground Source Heat Pump Systems," in *44th Workshop on Geothermal Reservoir Engineering*, Stanford, 2019.
- [10] M. Alam, M. Zain, A. B. M. Kaish and M. Jamil, "Underground Soil and Thermal Conductivity Materials Based Heat Reduction for Energy Efficient Building in Tropical Environment," *Indoor and Built Environment*, vol. 24, pp. 185-200, 2015.
- [11] M. Fossa, D. Rolando and P. Pasquier, "Pulsated Thermal Response Test experiments and modelling for ground thermal property estimation," in *IGSHPA Research Track*, Stockholm, September 18-20, 2018.
- [12] G. G and P. C, "Elementi di trasmissione del calore," Editoriale Veschi, 1990.
- [13] S. W. T. Kelvin, "Mathematical and Physical Papers II," 1882.
- [14] L. Ingersoll, O. Zobel and A. Ingersoll, "Heat conduction with engineering, geological, and other applications," 1954.
- [15] C. H.S. and J. J.C., *Conduction of heat in solids*, Oxford, U.K.,: Clarendon Press, 1947.
- [16] M. Abramovitz and I. Stegun, *Handbook of mathematical functions with formulas, graphs, and mathematical tables*, National Bureau of Standards, 1964.

- [17] Z. H.Y., D. N.R and F. Z.H., "A finite line-source model for boreholes in geothermal heat exchangers," *Heat Transfer-Asian Research*, no. 31, pp. 558-567, 2002.
- [18] L. L. and B. B., "A new contribution to the finite line-source model for geothermal boreholes," *Energy and Buildings*, no. 39, p. 188–198, 2007.
- [19] C. J. and J. S., "An analytical method to calculate borehole fluid temperatures for time-scales from minutes to decades," *ASHRAE Trans.*, vol. 2, no. 117, p. 279–288, 2011.
- [20] M. Fossa, "Correct design of vertical borehole heat exchanger systems through the improvement of the ASHRAE method," *Science and Technology for the Built Environment*, vol. 7, no. 23, pp. 1080-1089, 2017.
- [21] C. P., L. X., M. Y. and F. Z., "Heat transfer analysis of pile geothermal heat exchangers with spiral coils," *Applied Energy*, vol. 88, pp. 4113-4119, 2011.
- [22] M. Y., Y. H., D. N., L. J. and F. Z., "A new model and analytical solutions for borehole and pile ground heat exchangers," *Int. J. Heat Mass Transfer*, no. 53, pp. 2593-2601, 2010.
- [23] M. Y., Y. H., D. N., C. P., L. L. and F. Z., "Development of spiral heat source model for novel pile ground heat exchangers," *HVAC&R Research*, no. 17, pp. 1075-1088, 2011.
- [24] E. P., Thermal Analysis of Heat Extraction Boreholes. Ph.D. Thesis, Lund, Sweden: Lund University of Technology, 1987.
- [25] H. G. G. and S. B., Earth energy designer: software for dimensioning of deep boreholes for heat extraction, Lund, Sweden: Department of Mathematical Physics, Lund University, 1994.
- [26] F. M. and M. F., "The effect of borefield geometry and ground thermal load profile on hourly thermal response of geothermal heat pump systems," *Energy*, no. 51, pp. 323-329, 2013.
- [27] Clivet, "Zephir CPAN-XHE3: Technical Bulletin," Belluno, 2016.
- [28] Venticlima, "'Air" Fancoils Technical Bulletin," Treviso, 2017.
- [29] F. D.E., R. S.J., P. S.K. and M. A., "Implementation and validation of ground-source heat pump system models in an integrated building and system simulation environment," *HVAC&R Research*, vol. sup1, no. 12, pp. 693-710, 2006.
- [30] J. H., Parameter estimation-based models of water source heat pumps, PhD Thesis, Stillwater, Oklahoma: Oklahoma State University, 2002.
- [31] C. Tang, "Modeling packaged heat pumps in a quasi-steady state energy simulation program," *MS Thesis*, 2005.
- [32] A. Murugappan, "Implementing ground source heat pump and ground loop heat exchanger models in the Energyplus simulation environment.," *MS Thesis*, 2002.

- [33] E. D. Team, EnergyPlus Version 9.1 engineering reference: The reference to EnergyPlus calculations, US Department of Energy, 2019.
- [34] G. Venchi, "Università degli Studi di Pavia," 2014. [Online]. Available: <http://www-3.unipv.it/electric/elpot/Dispense-2013-2014.pdf>. [Accessed December 2019].
- [35] M. S. W. Z. Y. S. E. H. J. C. M. X. Y. Z. Y. L. D. L. a. L. C. Y. Zhao, "A solar photovoltaic system with ideal efficiency close to the theoretical limit," vol. 20, no. A28-A38, 2012.
- [36] E. J.E., Detailed Modeling of Photovoltaic Components. M. S. Thesis, Madison: Solar Energy Laboratory, University of Wisconsin, 1990.
- [37] D. J. A. and B. W. A., Solar Engineering of Thermal Processes., New York: John Wiley & Sons, Inc, 1991.